Building a platform for magnetic imaging of spin waves

Simon, B.G.

DOI
10.4233/uuid:ff3fb812-182e-4d09-803a-fe4ed30ce603

Important note
To cite this publication, please use the final published version (if applicable).
Please check the document version above.

BUILDING A PLATFORM FOR MAGNETIC IMAGING OF SPIN WAVES

BUILDING A PLATFORM FOR MAGNETIC IMAGING OF SPIN WAVES

Proefschrift

ter verkrijging van de graad van doctor
aan de Technische Universiteit Delft,
op gezag van de Rector Magnificus Prof. dr. ir. T.H.J.J. van der Hagen,
voorzitter van het College voor Promoties,
in het openbaar te verdedigen op vrijdag 7 juli 2023 om 12:30 uur

door

Brecht Gwendolyn SIMON

Master of Science in Physics,
Universiteit Leiden, Nederland,
geboren te Enschede, Nederland.

Dit proefschrift is goedgekeurd door de promotoren.

Samenstelling promotiecommissie:

Rector Magnificus	voorzitter
Prof. dr. L. Kuipers	Technische Universiteit Delft, promotor
Dr. ir. T. van der Sar	Technische Universiteit Delft, promotor

Onafhankelijke leden:

Prof. dr. Y. M. Blanter	Technische Universiteit Delft
Prof. dr. A. F. Otte	Technische Universiteit Delft
Prof. dr. ir. T. H. Oosterkamp	Universiteit Leiden
Prof. dr. E. Neu-Ruffing	Rheinland-Pfälzische Technische Universität Kaiserslautern-Landau, Duitsland
Prof. dr. S. Gröblacher	Technische Universiteit Delft, reservelid

Overig lid:

| Dr. ir. A. J. Katan | Technische Universiteit Delft |

CONTENTS

SUMMARY

Building a platform for magnetic imaging of spin waves

S PIN waves, with magnons their associated quasi-particles, are the elementary excitations of magnets. They represent the collective, wave-like motion of coupled electron spins that can transfer spin information across millimetre distances without the electrons moving themselves. As such, spin waves may provide a path towards low-dissipation information technology that does not suffer from the Joule heating currently limiting the performance of small-scale electronic devices. Furthermore, spin waves are fascinating because of their many-body physics, displaying rich phenomena like magnon condensation and non-linear interactions.

To obtain a better understanding of spin-wave transport and to explore new ways to control it, this thesis focuses on developing magnetic imaging techniques based on the single spin of the nitrogen-vacancy (NV) defect in diamond that detects spin waves via their magnetic stray fields. The NV centre's convenient properties, having spin-dependent photoluminescence (PL) and a long lifetime, make it a versatile and sensitive atomic-sized magnetic field sensor that has emerged in the last two decades as a powerful tool for visualizing magnetization and current distributions on the nanoscale.

Chapter 1 of this thesis starts with briefly outlining the research field dedicated to spin waves and describes the benefits of NV magnetometry for spin-wave detection. In addition, we introduce the basics of the spin-wave detection scheme used in this thesis. A more detailed explanation of the spin-wave theory relevant to this work follows in **chapter 2**. The properties of NV centres are explained in more detail in **chapter 3**, where we focus on the NV centre as a magnetic field sensor and the measurement modalities and experimental setup enabling the detection of nanoscale spin waves. **Chapters 4-6** describe the results of this PhD thesis.

At the heart of our NV magnetometry platform is a diamond scanning probe hosting the NV just below its apex. This scanning probe geometry allows for nanometre NV-sample proximity and sensitivity to nanoscale spin waves whose stray fields decay evanescently on the scale of their wavelength. **Chapter 4** describes the methods to fabricate such NV probes from single-crystal diamond. Its first part describes the implementation of existing protocols into our cleanroom facilities that resulted in our first generation of NV probes and formed the foundation of several projects in our group. In the second part of **chapter 4**, we present a new fabrication protocol that reliably produces NV probes with semi-conical shaped pillars that are predicted to guide the NV PL toward our collection optics twice as efficiently as standard cylindrical pillars. A preliminary optical characterization confirms the high PL rate of some of our second-generation NV probes, enabling

higher sensitivity or faster measurements.

Having realized our first generation of scanning NV probes with an ensemble of NV centres below their apex, **chapter 5** presents our lab's first spin-wave scanning NV measurements. Here, we image the directional excitation of ~500 nm coherent spin waves in yttrium iron garnet (YIG), a model magnet. Using distance-dependent measurements, we show that the magnetic spectral density associated with thermal spin-wave noise decays on a sub-micron length scale, supporting the need for a proximal magnetic field sensor. Additionally, when driving low-wavenumber coherent spin waves, we find a surprising increase in the magnon density extending hundreds of micrometres from only one side of the excitation stripline. This generation of a non-equilibrium magnon gas in target directions presents a new method for local control of spin waves that could be useful in devices.

Because the magnetic noise from incoherent spin waves increases dramatically as the NV probe approaches the sample, thereby quenching the NV photoluminescence and inducing a fast decay of the NV Rabi oscillations, scanning-NV imaging of nanoscale spin waves is challenging. In **chapter 6**, we show that by lifting the NV probe from the sample surface, we reduce the magnetic noise and recover our imaging capability. This enables high-contrast imaging of a primary-driven spin-wave mode that is optimal when the NV-sample distance is tuned to the expected spin wavelength. To achieve sensitivity to the higher-wavenumber frequency-degenerate modes, we minimize the NV-sample distance and reduce the drive power by two orders of magnitude. We hereby overcome the in-contact NV saturation and reveal the presence of a wide range of spin wavevectors along the two-dimensional spin-wave dispersion, including those of only ~360 nm. Because of our one-dimensional excitation geometry, the occupation of these two-dimensional wavevectors is surprising, which we attribute to defect-enhanced scattering. The demonstrated wavenumber-selective imaging of nanoscale magnetic oscillations is useful to understand spin-wave transport better and paves the way for imaging other coherent spin-wave modes or probing microwave electric current distributions.

The results obtained in this thesis demonstrate the exciting nanoscale physics that can be exposed by scanning NV magnetometry. Furthermore, with our new generation of NV probes, we expect an improvement in measurement sensitivity and speed. We summarize these findings in **chapter 7**, where we also identify ways to improve our sensor and avenues for future research.

SAMENVATTING

De bouw van een platform voor het magnetisch afbeelden van spingolven

Spingolven, met magnonen hun bijbehorende quasideeltjes, zijn de elementaire excitaties van magneten. Ze vertegenwoordigen de collectieve, golfachtige beweging van gekoppelde elektronenspins die spininformatie over millimeterafstanden kunnen overbrengen zonder dat de elektronen zelf bewegen. Spingolven bieden daarom een weg naar lage dissipatie informatietechnologie dat geen last heeft van de Joulewarmte die de prestaties van onze huidige elektronica beperkt. Daarnaast zijn spingolven ook fascinerend vanwege hun veeldeeltjesfysica, met rijke verschijnselen zoals magnonencondensatie en niet-lineaire interacties.

Om een begrip beter van spingolftransport te krijgen en om nieuwe manieren te verkennen om die te beheersen, richt dit proefschrift zich op het ontwikkelen van magnetische beeldvormingstechnieken gebaseerd op de enkele spin van het stikstof-gat (NV) roosterdefect in diamant dat spingolven detecteert via de door hun opgewekte magneetvelden. De handige eigenschappen van het NV centrum: zijn spinafhankelijke fotoluminescentie en lange levensduur, maken het tot een veelzijdige en gevoelige magneetveldsensor van atomaire grootte dat de laatste twee decennia is opgekomen als een krachtig instrument voor het visualiseren van nanoschaal magnetisatie- en stroomverdelingen.

Hoofdstuk 1 van dit proefschrift begint met een korte schets van het spingolfonderzoeksveld en benoemt de voordelen van NV magnetometrie voor spingolfdetectie. Daarnaast introduceren we de basisprincipes van het door ons gebruikte spingolfdetectiemechanisme. Een meer gedetailleerde uitleg van de relevante spingolftheorie volgt in **hoofdstuk 2**. De werking van het NV-centrum als een magneetveldsensor wordt in meer detail uitgelegd in **hoofdstuk 3**, waar we ook de meetmodaliteiten en de experimentele opstelling die de detectie van nanoschaal spingolven mogelijk maken beschrijven. **Hoofdstukken 4-6** beschrijven de in dit proefschrift behaalde resultaten.

Het hart van ons NV-magnetometrie platform bestaat uit een diamanten scansonde die het NV centrum in het uiteinde van zijn naald huist. Deze scansonde geometrie verschaft nanometer nabijheid tussen de NV en de magneet en daarmee gevoeligheid voor nanoscopische spingolven waarvan de magneetvelden evanescent vervallen op de schaal van hun golflengte. **Hoofdstuk 4** beschrijft de methoden om dergelijke NV-sondes uit enkel-kristal diamant te fabriceren. Het eerste deel beschrijft de implementatie van bestaande protocollen waarmee we onze eerste generatie NV-sondes realiseren en een basis leggen voor verschillende fabricageprojecten in ons lab. In het tweede deel presenteren we een nieuw protocol waarmee we NV-sondes met semi conische diamanten naalden creëren waarvan voorspeld wordt dat ze de fotoluminescentie tweemaal efficiënter

dan de standaard cilindrische naalden naar onze collectie-optiek leiden. Een eerste opti-sche karakterisering bevestigt de hoge fotoluminescentie van sommige van onze tweede generatie NV-sondes, die daardoor hogere gevoeligheid- of snellere metingen mogelijk maken.

Nadat we onze eerste generatie NV-sondes met een ensemble van NV-centra hebben gerealiseerd, presenteren we in **hoofdstuk 5** onze eerste spingolfmetingen in een scan-sonde geometrie. Hier brengen we de eenrichtingsexcitatie van ~500 nm coherente spingol-ven in beeld in yttrium ijzer granaat (YIG), een modelmagneet voor het bestuderen van spingolven. Met afstandsafhankelijke metingen laten we daarnaast zien dat de mag-netische spectrale dichtheid afkomstig van thermische spingolfruis op een sub-micron lengteschaal afneemt. Ook vinden we bij het exciteren van coherente spingolven met een laag golfgetal een verrassende toename van de magnonendichtheid dat zich vanaf slechts één kant van de excitatiestriplijn uitstrekt over meer dan honderden microme-ters. Deze eenrichtingsexcitatie van een niet-evenwichtig magnonengas presenteert een nieuwe methode voor het lokaal controleren van spingolven dat gebruikt zou kunnen worden in apparaten.

De magnetische ruis afkomstig van incoherente spingolven neemt dramatisch toe als de NV-sonde het magnetisch oppervlak nadert, met als gevolg een verlaagde NV foto-luminescentie en een snel verval van de NV Rabi oscillaties. Dit maakt het afbeelden van nanoscopische spingolven uitdagend. In **hoofdstuk 6** laten we zien dat, door de NV-sonde op te tillen van het magneetoppervlak, we de magnetische ruis verminde-ren en onze beeldvormingsmogelijkheden herstellen. We realiseren bovendien maxi-maal contrasterende afbeeldingen van een primair aangedreven spingolf wanneer de NV-magneetafstand is afgestemd op de verwachte spingolflengte. Om gevoeligheid voor gelijkfrequente spingolven met een hoger golfgetal te behalen, minimaliseren we daarna de NV-magneet-afstand terwijl we het excitatievermogen met twee orden van grootte verlagen om saturatie van het NV centrum te voorkomen. Deze metingen onthullen de aanwezigheid van een breed scala aan spingolfvectoren langs de tweedimensionale spingolfdispersie, waaronder die met golflengtes van slechts ~360 nm. De in eerste in-stantie verassende tweedimensionale bezetting van golfvectoren, gezien onze eendimen-sionale excitatiegeometrie, schrijven we toe aan een grotere mate van spingolfbotsingen als gevolg van defecten in het magneetoppervlak. Deze selectieve afbeelding van nano-scopische magnetische oscillaties op basis van het spingolfgetal is nuttig om een beter begrip te krijgen van spingolftransport en baant een weg voor de beeldvorming van an-dere coherente spingolfmodi of het visualiseren van elektrische stroomverdelingen.

De in dit proefschrift behaalde resultaten zijn tonend voor de spannende nanoschaal-fysica die kan worden blootgelegd met NV magnetometrie in een scansonde geometrie. Met onze nieuwe generatie NV-sondes verwachten we daarnaast een verbetering van onze meetgevoeligheid en -snelheid. We vatten deze bevindingen samen in **hoofdstuk 7**, waar we ook manieren noemen om onze sensor te verbeteren en richtingen voor toe-komstig onderzoek duiden.

1

INTRODUCTION

D UE to their useful properties, *magnets* play an indispensable role in modern-day technology. A role that is a result of extensive curiosity-driven research whose origin dates back to ~600 BC when Thales philosophized that the magnet must have a soul because it moves the iron[1]. Eventually, the realization that lodestones, magnetic magnetite crystals, always point in the same direction, towards the earth's magnetic pole, gave rise to a new tool that became widely used from the ~11th century [2, 3]: the magnetic compass. The compass is one of the first forms of technology employing magnets, and it enabled reliable navigation for generations of explorers.

Due to the rich physics displayed by magnets, the study of magnetism remains a driving force in technological progress and continues to inspire researchers up until today. Examples of recent technological advancements are the creation of large and homogeneous magnetic fields to enhance the resolution in magnetic resonance imaging (MRI)[4] and to accurately bend the trajectory of elementary particles in CERN's large hadron collider[5, 6].

On a much smaller scale, the ability to control a material's magnetization on the nanoscale using tiny electronic circuits has provided increased data storage capacity for memory devices such as magnetic hard drives[7, 8]. Furthermore, to produce increasingly smaller devices, a broad community seeks solutions to one major factor limiting the performance of micron-scale electronics: the heat-generating dissipative motion of electron charges. One solution that holds particular promise to realize fast data processing on nanometre-length scales is to utilize the motion of coupled electron spins and their associated magnetic moments in magnets. Such a collective motion of precessing spins is called a *spin wave*.

1

1.1. SPIN WAVES

In this thesis, we study spin waves, the collective, wave-like excitations of magnetically ordered materials, first predicted by F. Bloch ~100 years ago[9]. Astonishingly, micrometre wavelength spin waves can propagate over millimetre-long distances upon excitation while preserving spin information due to the low damping observed in some materials[10].

Their low damping is one of the key reasons why spin waves have attracted the interest of a growing research field that wants to utilize spin waves for computing and information storage [11, 12]. Additionally, spin-wave-based logic devices have a potential functionality that goes beyond traditional Boolean logistics [13], as information can be encoded in both the spin-wave's amplitude and phase. Nevertheless, despite recent technological advancements, such as the realization of a spin-wave transistor [14] and a directional coupler[15], the generation, control, and readout of spin waves remain challenging and require a better understanding.

In addition, their many-body physics is interesting by itself and gives rise to exciting phenomena, such as magnon condensation and spin superfluidity[16–18], magnon-phonon coupling[19–22], and quantum magnonics[23], where magnons are a spin-wave mode's elementary quasi-particles. Finally, the recent observation of magnetism in 2D materials has triggered the prospect of utilizing and studying spin waves in the ultimate 2D limit[24–27].

To explore these exciting research opportunities, we require a sensor that provides nanoscale resolution to the magnetic signals produced by spin waves. In this thesis, we, therefore, use a magnetometry technique based on an atomic-sized magnetic field sensor: The *nitrogen-vacancy (NV) centre in diamond*. The NV centre provides a local measure of the magnetic field and detects spin waves via the stray fields they generate. In particular, by bringing our sensor in *nanometre proximity* to the magnetic surface, we realize nanoscale spin-wave sensitivity (Fig. 1.1).
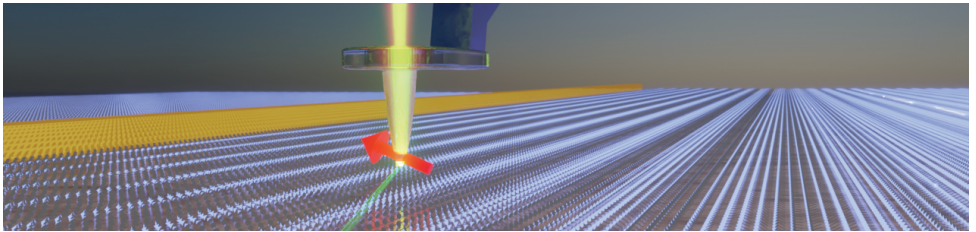
Figure 1.1: Thesis cover showing an artist's impression of a scanning NV probe with an NV centre (red arrow) just below the tip apex to image the evanescent stray magnetic fields of nanoscale spin waves (small blue arrows) in a thin magnetic film. Green and red light rays indicate the NV excitation and the photoluminescence paths. The yellow bar represents the microwave stripline used for spin-wave excitation.

1

1.2. THE NITROGEN-VACANCY CENTRE

The nitrogen-vacancy (NV) centre is a spin-triplet system that arises from an atomic defect in the diamond carbon lattice. The NV centre's photoluminescence (PL) depends on its spin state, enabling its spin optical readout and initialization[28–30]. The NV spin is also known for its long coherence time of a few ms even at room temperature[31–33]. These convenient properties combined have made the NV centre a pivotal actor in developing quantum technologies such as quantum computing[34, 35], quantum networks[36, 37], and sensing [38–40] over the last two decades.

One of the NV's key properties is its susceptibility to magnetic fields, which is the core of a new magnetic sensing technique utilizing the NV's atomic size and single-spin sensitivity: NV magnetometry[29].

NV magnetometry combines several appealing features for studying magnetism: It provides a quantitative measure of the magnetic field[29]. Due to its atomic size, it can generate nanoscale-resolution magnetic field images[41]. It operates in ambient conditions and harsh environments like ultra-low temperatures[42] or high pressures[43]. Spin manipulation schemes that have undergone extensive development from NMR and quantum computing communities can be extended to NV sensing, thereby significantly expanding the sensor's sensitivity and bandwidth[33, 44–46]. Its host material, diamond, is chemically inert and is therefore compatible with many sensitive samples such as biological tissues[30, 47] or geological samples[48, 49]. Finally, setups to perform high-sensitivity NV magnetometry are only table-sized, with special NV-based sensors miniaturized to hand-held devices[50, 51], making it a low-cost and small-footprint alternative to, e.g., synchrotron techniques.

For probing fields that spatially vary on the nanoscale or decay evanescently, it is necessary to obtain nanometer proximity between the NV and a sample. One way to realize a minimized NV-sample distance is by combining NV magnetometry with scanning probe microscopy and using a sharp scanning all-diamond tip with an NV just below its apex[52]. In the last decade, scanning NV magnetometry has proven to be a powerful tool for studying condensed matter systems on the nanoscale by imaging the stray fields from ultra-thin van der Waals magnets [41, 53], or antiferromagnetic domains [54, 55] and current flow in graphene[56, 57]. Excitingly, the first commercial scanning NV magnetometers have recently become available, broadening the technique's accessibility and applications. And in this work, we present the useful capabilities of our (home-built) scanning NV magnetometer for studying spin waves and their nanoscale stray fields.

1.3. SPIN-WAVE DETECTION VIA NV MAGNETOMETRY

In this thesis, we study spin waves in a thin film of the ferrimagnet *yttrium iron garnet (YIG)*, which is famous for its ultra-low damping providing an excellent platform to study spin-wave physics[10]. We now briefly introduce how we use NV centres to probe spin waves in YIG, setting the stage for the more detailed analysis that will follow in this thesis:

1

Like many other ferromagnetic materials, the spin-wave excitations of YIG lie in the gigahertz regime. Our spin-wave detection scheme relies on the fact that the electron spin resonance (ESR) frequencies of our spin sensor ($f_\pm$), the NV centre, lie in that same regime (Fig. 1.2a). Specifically, by applying an external field, which causes the NV spin sublevels to split, we can vary the NV ESR frequencies relative to the spin-wave band to tune in resonance with different frequency and wavelength spin waves (Fig. 1.2b).

Another key point is that the NV centre detects spin waves via their *microwave magnetic stray fields*. Specifically, we can detect spin waves resonant with the NV ESR transition by monitoring the NV's spin-dependent photoluminescence (PL) while sweeping the frequency of an external microwave field used to excite spin waves (Fig. 1.2c). At $f = f_\pm$, the NV PL dips when an NV-resonant spin wave is excited, and its stray field drives the NV ESR transition between the optically bright and dark NV spin states. Finally, we can obtain the amplitude of the spin-wave field via the ESR contrast, C, describing the ESR transition rate [58].
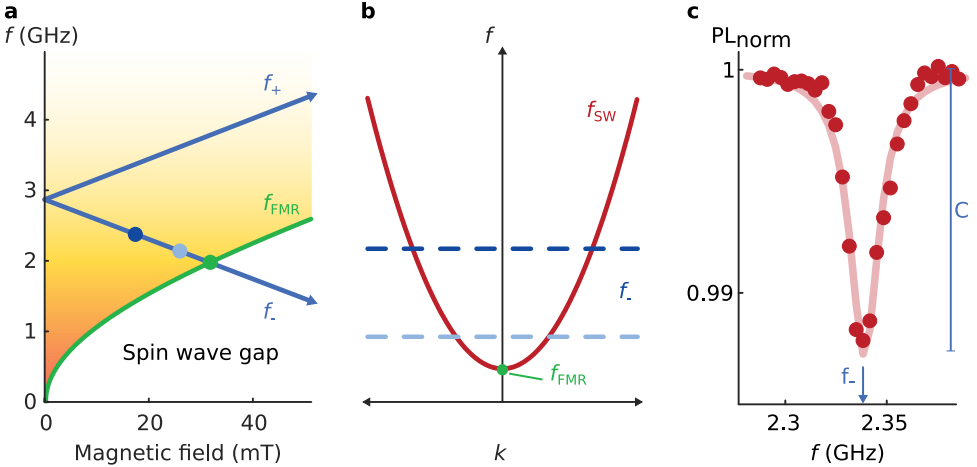
Figure 1.2: Using the NV centre for spin-wave detection (a) The NV spin ground state is a spin triplet, having two electron spin resonance (ESR) frequencies ($f_\pm$), that lie in the GHz range (blue arrows) and depend on the magnetic field along the NV axis. To detect spin waves in yttrium iron garnet (YIG), we use that YIG's spin-wave excitations lie in the same frequency range, indicated by the orange gradient representing a thermal occupation of spin-wave modes. The ferromagnetic resonance (f_{FMR}, green) indicates the frequency associated with the uniform spin-wave mode ($k = 0$). (b) A simple parabolic dispersion explaining the NV centre's sensitivity to different wavelength spin waves at different external fields: When $f_- = f_{FMR}$ (green dot in a&b), the NV is resonant with YIG's uniform mode that does not generate a field above the magnet. Light blue line, the NV is resonant with finite wavenumber spin waves, corresponding to a lower magnetic field (light blue dot in a). When detuning further from the FMR (dark blue line and dot in a), the NV becomes sensitive to higher wavenumber and shorter wavelength spin waves. (c) Electron spin resonance (ESR) measurement monitoring the NV's spin-dependent photoluminescence (PL) while sweeping the frequency of an external microwave drive. The PL is normalized by the PL without microwave driving. The microwave drive excites spin waves in a magnet. The spin waves generate stray fields that, if resonant ($f = f_\pm$), can drive the NV's ESR transition, causing a dip in the NV PL. For decreasing NV-sample distance, the ESR contrast C increases due to the increased amplitude of the evanescent spin-wave stray fields.

1.4. THESIS OUTLINE

In this thesis, we use NV centres for the magnetic imaging of nanoscale spin waves. We continue in **chapter 2** by covering the spin wave theory relevant to understanding the results described in this thesis. Next, in **chapter 3**, we discuss how we use the NV centre as a magnetic field sensor and the required measurement modalities and experimental setup to detect nanoscale spin waves.

In **chapter 4**, we discuss our work on the nanofabrication of diamond for NV magnetometry, focusing on the fabrication of scanning NV probes. We start by describing the fabrication of our first generation of scanning NV probes, which required implementing existing fabrication protocols in our cleanroom facilities. Then, the second part of chapter 4 describes the optimization of our fabrication protocol in terms of its reproducibility. At the same time, our new protocol allows us to fabricate NV probes with a conical shape instead of the standard cylindrical pillars. Using simulations, we show that such highly tapered pillars guide the NV PL to our collection optics more efficiently. As such, our second generation of NV probes provides a higher PL collection efficiency and, ergo, a higher magnetic field sensitivity enabling the detection of weaker fields or reducing measurement times for future experiments.

In **chapter 5**, we use our first generation of NV probes to image the coherent transport of ~500 nm spin waves in a thin film of the magnetic insulator yttrium iron garnet. In addition, we show that the excitation of coherent spin waves enables the generation of a high-density magnon gas in preferential directions. The observed sub-micron spatial decay lengths of the stray fields generated by the out-of-equilibrium magnon gas indicate the presence of small-wavenumber magnons, highlighting the need for proximal sensors such as our scanning-probe NV magnetometer.

In **chapter 6**, we fully exploit the nanoscale control of the NV-sample distance to filter the stray fields of spin waves depending on their wavenumber. Due to the wavelength filtering action of our sensor, we reveal that stripline excitation occupies a range of spin wavevectors along the two-dimensional dispersion despite having a one-dimensional excitation geometry. In addition, our nanoscale spin wave images, including spin-wave modes down to ~360 nm wavelength, pave the way to high-resolution spin wave sensing.

2

SPIN-WAVE THEORY

Spin waves are the elementary excitations of magnetically ordered materials with magnons their associated quasi-particles. In this thesis, we use nitrogen-vacancy (NV) magnetometry to study spin waves by their evanescent magnetic fields. This chapter discusses the spin-wave theory relevant to chapters 5 and 6. We describe the dispersion of spin waves in thin magnetic films and the stray fields the spin waves generate. We then highlight two situations: one in which the NV spin is used to detect coherent spin waves excited via a microwave stripline, and another in which we characterize the NV relaxation dynamics to probe the thermal incoherent spin-wave bath.

2.1. Elementary excitations in magnets

T HE magnetization of a material determines its ability to produce magnetic fields and thereby attract or repel other (magnetic) materials. Magnetization is a macroscopic quantity that emerges from the interaction between the material's individual electrons.

For example, the exchange coupling between two neighbouring electrons in ferromagnetic materials tries to align their spins. Considering the magnetic moments of all the electrons in the material, this can give rise to a macroscopic magnetization with an associated magnetic field that gives the magnet its ability to stick to your refrigerator's door.

Upon excitation of a magnet's magnetization, the coupling between the individual spins gives rise to a wave-like mode of collectively precessing spins (Fig. 2.1). Such a mode of precessing spins, also known as a *spin wave*, is described by an eigenfrequency. A spin-wave mode's elementary (quasi-)particle is called a magnon, a bosonic particle, obeying Bose-Einstein statistics[59]. The non-linear interactions between spin waves give rise to interesting phenomena, such as the unique ability to manipulate a spin wave using other spin waves, and provide a promising platform for new spin-wave-based information technology[60].
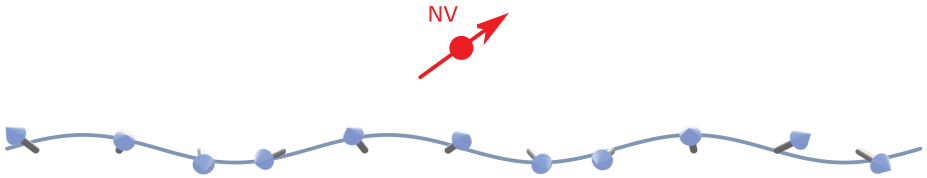
Figure 2.1: Illustration of a spin wave and our probe. Spins precessing slightly out-of-phase with their neighbouring spins around their equilibrium magnetization, giving rise to a collective motion that we describe as a spin wave. Spin waves generate microwave magnetic fields that evanescently decay from the surface on the scale of their wavelength, which can be detected using a nearby NV centre. Here we drew the NV and the spin-wave in a random orientation for visibility.

In our work, we study spin waves in the ferrimagnet yttrium iron garnet (YIG), which, when epitaxially grown with high quality, has the lowest spin damping observed in ferromagnets so far [10]. Like other ferromagnetic systems, its spin-wave excitations lie in the GHz range enabling the inductive excitation and detection via standard microwave electronics with spin-wavelengths varying from millimetres down to the nanoscale[10]. Due to the low damping, coherent spin waves can travel over mm distances, making YIG a model magnet to study spin-wave physics and magnon interactions since the discovery of YIG in the 1960's[10, 61]. The promise to control its magnetization on the nanoscale and its extremely low damping within an electronically insulating environment has recently revived the field of magnonics for the potential of spin-wave-based information technology[60].

Several established techniques exist for studying spin waves: Transport measurements that exploit the spin-Hall effect induced by nearby spin waves in heavy metal electrodes[62,

63] or the inductive coupling of spin wave stray fields to microwave striplines[64–66]. As well as advanced imaging techniques where the most prominent rely on the interaction of light with magnetization such as Brillouin Light spectroscopy[67, 68], X-ray scattering[69, 70] and magneto-optical Kerr effect based spectroscopy[71, 72].

In this thesis, we employ scanning nitrogen-vacancy (NV) magnetometry to study spin waves via their stray magnetic fields. This technique combines several benefits useful for spin-wave detection: We can obtain magnetic images with nanoscale spatial resolution while using a table-top setup. Our sensor has a narrow frequency bandwidth (~MHz) that we use to characterize the power spectral density of the spin-wave generated magnetic fields. In particular, we get access to the magnetic susceptibility and corresponding spin-spin fluctuations of a nearby magnetic material by probing the NV relaxation rates without having to perturb the magnetic system [73]. Additionally, nanoscale control over the sensor-sample distance provides a wavelength filter for probing frequency-degenerate spin waves. The preferential driving of the NV ESR transitions by magnetic fields of a specific handedness gives access to the chirality of the spin-wave precession[58]. Finally, detection based on stray magnetic fields enables imaging of spin-wave transport below optically opaque materials such as metals and superconductors [74, 75].

This chapter discusses the theory for calculating the spin-wave generated stray-magnetic fields above a thin ferromagnetic film. To do so, we start by describing the spatial and temporal dynamics of the film's magnetization using the free energy and the Landau-Liftshiftz-Gilbert (LLG) formalism (§2.2). From the LLG equation, we derive the spin-wave dispersion (§2.3). Then, in §2.4, we analyze the stray fields generated by both coherent and thermal spin waves and how they couple to our NV sensor. Here, we also describe how varying the NV-sample distance can be used to wavelength-filter frequency-degenerate spin waves (§2.4.4).

2.2. MAGNETIZATION DYNAMICS

To derive the spin-wave dispersion, we start by describing the dynamics of spins inside a magnet using the phenomenological Landau-Liftshitz-Gilbert (LLG) equation[76]:

$$\frac{d}{dt}\vec{m}' = -\gamma\,\vec{m}' \times \vec{B}_{\text{eff}} + \alpha\,\vec{m}' \times \frac{d}{dt}\vec{m}', \quad \text{with} \quad \vec{B}_{\text{eff}} = \frac{1}{M_s}\frac{\partial F}{\partial\vec{m}} \tag{2.1}$$

Here the first term describes the torque generated by an effective field, B_{eff}, causing the film's magnetization to tilt away from its equilibrium direction and to precess around it (Fig. 2.2). The effective field is calculated from the free energy F, which we describe below for a thin magnetic film. The second term describes the dissipation as parameterized by the Gilbert damping parameter, α, which causes the magnetization to relax back to its equilibrium direction.
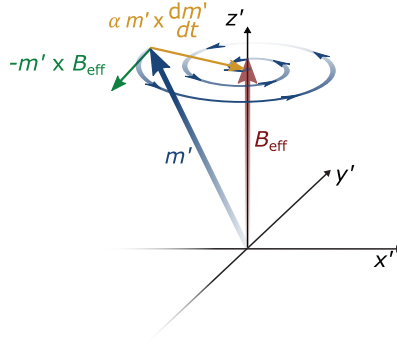
Figure 2.2: A precessing magnetic moment in the effective magnetic field of a magnetic material in the magnet frame $\vec{m}'$. The precession is counter-clockwise around the direction of the effective magnetic field. The magnet frame is defined such that the equilibrium magnetization is along z'.

2.2.1. LINEARIZING THE LLG EQUATION

Following the derivations provided by Refs. [73, 77], linearization of the LLG equation allows us to obtain the spin-wave dispersion. To do so, we first define the *magnet frame*, which is a coordinate system in which the equilibrium magnetization is pointing along z'. Additionally, we assume that the deviations from the equilibrium magnetization ($\delta\vec{m}$) are small everywhere in space and time. The linearized LLG equation then reads:

$$-i\omega\delta m_{x'} = -\gamma(\delta m_{y'} B_{\text{eff},z'} - B_{\text{eff},y'}) + i\alpha\omega\delta m_{y'} \tag{2.2a}$$

$$-i\omega\delta m_{y'} = -\gamma(B_{\text{eff},x'} - \delta m_{x'} B_{\text{eff},z'}) - i\alpha\omega\delta m_{x'} \tag{2.2b}$$

which is defined in wavevector and frequency space to describe the spatial and temporal dynamics of the magnetization in terms of the in-plane wavevector: $\vec{k} = (k_z, k_y)$, with associated wavenumber $k = \sqrt{k_z^2 + k_y^2}$ and the spin-precession frequency ω. Here, $B_{\text{eff},z'}$ is the *static* component of the effective field along z' and $B_{\text{eff},x'}$ and $B_{\text{eff},y'}$ are the components of the effective field along x' and y' that *oscillate* at a frequency ω.

2.2.2. FREE ENERGY OF A MAGNET

We now evaluate the magnetic interactions dominant in a thin film of YIG to obtain its free energy and the associated effective magnetic field, B_{eff}. The *free energy density* of a thin magnetic film of YIG, described by a spin density $M_s\vec{m}$ and with M_s YIG's saturation magnetization, is governed by the following magnetic contributions, where we neglected magnetic anisotropies[73]:

$$f = -M_s\vec{m}\left(\vec{B}_{\text{Zeeman}} + \frac{1}{2}\vec{B}_{\text{dem}}\right) + A_{\text{ex}}\sum_{\alpha,\beta=x',y',z'}\left(\frac{\partial m_\alpha}{\partial\beta}\right)^2 \tag{2.3}$$

Here the first term describes the *Zeeman energy* associated with an external magnetic field. The second term describes energy associated with the *demagnetizing field* generated by the dipole moments in the system. The final term describes the *exchange energy*,

describing the interaction between neighbouring spins. Here, A_{ex} is the exchange constant (assuming isotropic exchange interaction), which is also often expressed in terms of the spin stiffness: $D = 2\gamma A_{ex}/M_s$, with γ the electron gyromagnetic ratio.

Below, we evaluate the contributions of each of these terms to the effective magnetic field. For the small externally applied fields used in this thesis ($B_0 \ll \mu_0 M_s$), the YIG equilibrium magnetization lies predominantly in the sample plane (Fig. 2.3a). Therefore, we can take the magnet and lab frames to overlap, which simplifies the following derivations.
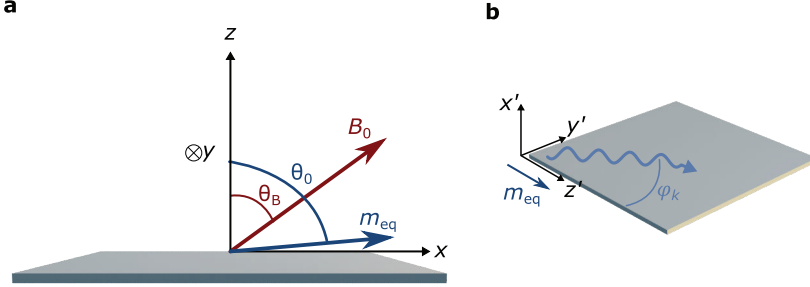
Figure 2.3: Experiment geometry and definition of lab and magnet frame (a) The magnetic film with the definition of the coordinate systems. Here, a bias field B_0 is applied to tune the NV electron spin resonance (ESR) frequencies relative to the spin-wave dispersion, which is at an angle θ_B with respect to the sample surface. For the external fields used in our measurements, the out-of-plane components of the external fields used in this thesis $B_{OOP} < 30\,\text{mT}$ are much smaller than the field required to tilt the magnetization out of the plane $\mu_0 M_s = 175\,\text{mT}$, such that the equilibrium magnetization lies in the sample plane with $z = z'$ and $\theta_0 \approx \pi/2$. (b) Definition of the magnet-frame coordinate system where the equilibrium magnetization aligns with z' for a magnetization that lies in the sample plane ($z = z'$ and $\theta_0 = \pi/2$). The out-of-plane transverse magnetization deviations are described by $\delta m'_y$ and $\delta m'_x$. The wiggly arrow represents a spin wave traveling at an angle $\phi_k = \tan^{-1}\frac{k_y}{k_z}$ with respect to the equilibrium magnetization.

ZEEMAN FIELD

The Zeeman field determines the energy associated with a magnetization in a static external magnetic field. Its component along the equilibrium direction is:

$$\vec{B}_{\text{Zeeman}} = \frac{\omega_B}{\gamma}\hat{z}, \quad \text{with} \quad \omega_B = \gamma B_0 \sin\theta_B \tag{2.4}$$

where θ_B describes the angle of the external field with the surface normal, assuming the magnetization is in-plane.

EXCHANGE FIELD

To obtain the contribution of the exchange field to the effective field, we take the functional derivative of the exchange part of the free energy (Eq. 2.3) in wavevector space, obtaining[58, 73]:

$$\vec{B}_{\text{ex}} = -\frac{\omega_{\text{ex}}}{\gamma}k^2\,\delta\vec{m}, \quad \text{with} \quad \omega_{\text{ex}} = \gamma D/M_s \tag{2.5}$$

Note, because m_z is spatially homogeneous, we have $B_{\text{ex,z}} = 0$.

DEMAGNETIZING FIELD

The demagnetizing field experienced by the magnetization is determined by summing over the dipole fields generated by all other spins in the material. The dipole field generated by a magnetic film with magnetization $\vec{M}(\vec{r}) = M_s \vec{m}(\vec{r})$ can be written as[58, 73]:

$$\vec{B}_{\text{dip}}(\vec{r}) = \mu_0 M_s \int d\vec{r}\, \vec{D}(\vec{r} - \vec{r}')\vec{m}(\vec{r}) \tag{2.6}$$

where $\vec{D}$ is the dipolar tensor with its components the spatial derivatives of the Coulomb kernel[58, 73]:

$$D_{\alpha\beta}(\vec{r}) = \frac{\partial}{\partial\alpha} \frac{\partial}{\partial\beta} \frac{1}{4\pi|\vec{r}|}, \quad \text{with} \quad \alpha, \beta = x, y, z \tag{2.7}$$

The demagnetizing field in terms of the in-plane wavevector $\vec{k}$ is obtained by taking the 2D Fourier transform and averaging the dipole field contributions inside the magnetic film (Eq.2.6) over the film thickness (t) [58, 73]:

$$\vec{B}_{\text{dem}}(\vec{k}) = -\frac{\omega_{\text{dem}}}{\gamma} \overline{D}(\vec{k}) \vec{m}(\vec{k}), \quad \text{with} \quad \omega_{\text{dem}} = \gamma\mu_0 M_s \tag{2.8}$$

where we assumed that the magnetization does not vary across the thickness direction and with $\overline{D}(\vec{k})$ the 2D Fourier transform of the averaged dipolar tensor[73]:

$$\overline{D}(\vec{k}) = \begin{pmatrix} 1 - f_t & 0 & 0 \\ 0 & f_t \frac{k_y^2}{k^2} & f_t \frac{k_y k_z}{k^2} \\ 0 & f_t \frac{k_y k_z}{k^2} & f_t \frac{k_z^2}{k^2} \end{pmatrix}, \quad \text{with} \quad f_t = 1 - \frac{1 - e^{-kt}}{kt} \tag{2.9}$$

where the factor f_t follows from taking the average over the film thickness. From the Zeeman, exchange, and demagnetizing contributions we obtain B_{eff}:

$$\gamma B_{\text{eff},x} = \left(-\omega_{\text{ex}}k^2 - \omega_{\text{dem}}(1 - f_t)\right)\delta m_x \tag{2.10a}$$

$$\gamma B_{\text{eff},y} = \left(-\omega_{\text{ex}}k^2 - \omega_{\text{dem}}f_t \sin^2 \phi_k\right)\delta m_y \tag{2.10b}$$

$$\gamma B_{\text{eff},z} = \omega_B \tag{2.10c}$$

where we used $\sin\phi_k = k_y/k$.

2.2.3. MAGNETIC SUSCEPTIBILITY

Having determined all contributions to the effective field, we go back to where we left off, and we substitute Eq. 2.10 into Eq. 2.2 while including a time-dependent transverse drive field: $\vec{B}_{\text{eff}} \rightarrow \vec{B}_{\text{eff}} + \vec{B}_{\text{AC}}$, with $\vec{B}_{\text{AC}} = (B_{\text{AC},x}, B_{\text{AC},y}, 0)$, we get:

$$i\omega\delta m_x = \delta m_y \left(\omega_B + \omega_{\text{ex}}k^2 + \omega_{\text{dem}}f_t \sin^2 \phi_k - i\alpha\omega\right) - \gamma B_{\text{AC},y} \tag{2.11a}$$

$$i\omega\delta m_y = \delta m_x \left(-\omega_B - \omega_{\text{ex}}k^2 - \omega_{\text{dem}}(1 - f_t) + i\alpha\omega\right) + \gamma B_{\text{AC},x} \tag{2.11b}$$

Next, we rewrite Eq. 2.11 into matrix form to obtain the relation between the transverse magnetization and the drive field:

$$\gamma\vec{B}_{\text{AC}} = \begin{pmatrix} \omega_2 - i\alpha\omega & i\omega \\ -i\omega & \omega_3 - i\alpha\omega \end{pmatrix} \begin{pmatrix} \delta m_x \\ \delta m_y \end{pmatrix} \tag{2.12}$$

where we used the definitions:

$$\omega_0(\vec{k}) = \omega_B + \omega_{ex}k^2 \tag{2.13a}$$

$$\omega_2(\vec{k}) = \omega_0 + \omega_{dem}(1 - f_t) \tag{2.13b}$$

$$\omega_3(\vec{k}) = \omega_0 + \omega_{dem}f_t\sin^2\phi_k \tag{2.13c}$$

$$\Lambda(\omega) = (\omega_2 - i\alpha\omega)(\omega_3 - i\alpha\omega) - \omega^2 \tag{2.13d}$$

By taking the inverse of the matrix in Eq. 2.12, we obtain the transverse magnetic susceptibility $\vec{S}$ describing the response of the transverse magnetization to a drive field ($\delta\vec{m} = S\vec{B}_{AC}$) for a film with an in-plane magnetization:

$$S(\vec{k}, w) = \frac{\gamma}{\Lambda}\begin{pmatrix} \omega_3 - i\alpha\omega & -i\omega \\ i\omega & \omega_2 - i\alpha\omega \end{pmatrix} \tag{2.14}$$

From the magnetic susceptibility, we will now evaluate the spin-wave dispersion of YIG.

2.3. SPIN-WAVE DISPERSION RELATION

Now, we can calculate the spin-wave dispersion, an important relation we use throughout this thesis to relate a spin wave with frequency ω to its wavevector $\vec{k}$, or wavelength $\lambda = 2\pi/|\vec{k}|$. The spin-wave dispersion is given by the frequencies for which the susceptibility is singular, i.e., when: $\Lambda(\omega) = 0$ (Eq. 2.13d). We can obtain the resonance frequency in the limit of zero Gilbert damping (Fig. 2.4a):

$$\omega = \sqrt{\omega_2\omega_3} \tag{2.15}$$

For low-k spin waves, which we consider here, the dispersion is characterized by its anisotropic dependence on the direction of the spin-wavevector (Fig. 2.4a). This anisotropy is due to the dominant contribution of the dipolar energy for small wavenumbers. As a result, spin waves of the same wavelength have a different frequency when travelling along the magnetization (described by finite k_z and $k_y = 0$), compared to when travelling perpendicular to the magnetization (described by finite k_y and $k_z = 0$).

The mode at $k = 0$ is called the *ferromagnetic resonance (FMR)*, which has an infinite wavelength, meaning that all magnetic moments precess in phase throughout the entire magnetic film. For an in-plane magnetization and external field ($\theta_B = \pi/2$), the associated frequency is given by:

$$\omega_{FMR} = \gamma\sqrt{B_0(B_0 + \mu_0 M_s)} \tag{2.16}$$

which is also referred to as the Kittel mode (Fig. 2.4b)[78]. The FMR can be driven efficiently due to, e.g., a spin-wave excitation stripline having the highest amplitude at $k = 0$. The homogeneous FMR mode does not generate a stray field above the magnetic film. Nevertheless, through the subsequent scattering of high-amplitude FMR magnons into higher-frequency modes, which do generate stray fields, NV-detection of the FMR is possible[79].

Due to the anisotropic spin-wave dispersion, the FMR is not necessarily the lowest energy state. Spin waves with $k_y = 0$ have a characteristic negative group velocity for low-k modes, yielding a finite wavenumber ($\pm k_{\min}$) lowest energy state. This spin-wave branch on the dispersion is also called the *backward-volume (BV) spin-wave* dispersion. Below this minimum frequency, which we refer to as the bottom of the spin-wave band f_B, no spin-wave excitations exist (Fig. 2.4b).

Damon-Eshbach (DE) spin waves, which propagate perpendicular to the magnetization ($k_z = 0$), are known for their exponential confinement to the top/bottom surface depending on the sign of the wavevector[73, 80]. For this reason, DE spin waves are often referred to as magnetostatic *surface* spin waves that produce chiral magnetic fields with a handedness and an amplitude that depend on the travel direction. This chirality is essential to understanding their detection using NV centers, as discussed in the following paragraphs.
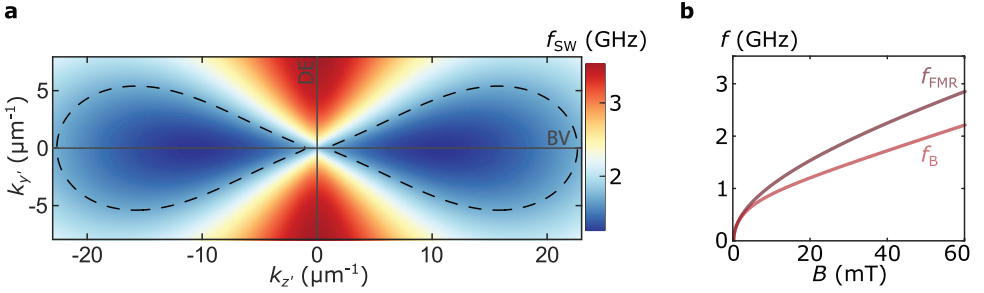
Figure 2.4: Spin-wave dispersion. Calculated spin-wave dispersion for $B_0 = 35\,\mathrm{mT}$ and $\theta_B = \theta_{NV} = 0.95$ with material parameters: $L \approx 235\,\mathrm{nm}$, $M_s = 1.42 \times 10^5\,\mathrm{A\,m^{-1}}$, $A_{ex} = 3.7 \times 10^{-12}\,\mathrm{J\,m^{-1}}$ and $\alpha = 1 \times 10^{-4}$. The dashed line represents an iso-frequency contour at $f = 1.89\,\mathrm{GHz}$, which is the NV f_--frequency at this field. At this field, the f_--frequency is between the ferromagnetic resonance f_{FMR} and the bottom of the spin wave band f_B such that there exist no NV resonant DE-spin waves. (b) The frequencies of the ferromagnetic resonance f_{FMR} and the bottom of the spin-wave band f_B as a function of the magnetic field B_0.

2.4. SPIN-WAVE STRAY MAGNETIC FIELDS

Now that we know the spin-wave dispersion and have summarized the important properties of the different modes, we can calculate their stray fields and their projection onto the axis of the NV centre that we use for spin-wave detection.

To do so, we calculate the magnetic field as a result of a magnetization (as we did to obtain the demagnetizing field in §2.2.2). Instead, we compute here the dipole field as seen from above the magnetic film:

$$\vec{B}(\vec{k}) = D(\vec{k})\delta\vec{m} \tag{2.17}$$

where the dipolar tensor $D(\vec{k})$ now describes the spin-wave stray field at a distance d_{NV} above the magnetic surface (still assuming perfect in-plane magnetization, such that lab

frame and magnet frame overlap):

$$D(\vec{k}) = A_k \begin{bmatrix} -1 & ik_y/k & ik_z/k \\ ik_y/k & k_y^2/k^2 & k_zk_y/k^2 \\ ik_z/k & k_zk_y/k^2 & k_z^2/k^2 \end{bmatrix},$$ (2.18)

with

$$A_k = -\frac{\mu_0 M_s}{2} e^{-k d_{\mathrm{NV}}}(1 - e^{-kt})$$ (2.19)

where the factor $1 - e^{-kt}$ arises from averaging over the film thickness. From Eq. 2.18, we can see that circularly polarized fields of which the amplitude and the handedness depend on the spin-wavevector characterize the stray fields of spin waves:

$$B_x(\vec{k}) = A_k[-\delta m_x + ik_y/k\,\delta m_y]$$ (2.20a)

$$B_y(\vec{k}) = -ik_y/kB_x(\vec{k})$$ (2.20b)

$$B_z(\vec{k}) = -ik_z/kB_x(\vec{k})$$ (2.20c)

Now we use these relations to study the effect of spin-wave fields on the spin state of a nearby NV centre. We first discuss microwave-excited spin waves driving coherent NV spin rotations (§2.4.1-2.4.2) and later study the effect of thermally-excited spin waves that form an incoherent bath of background spin waves that cause NV spin relaxation (§2.4.3).

2.4.1. SPIN-WAVE GENERATED NV RABI OSCILLATIONS

If resonant with the NV ESR frequencies ($f_{\mathrm{sw}} = f_{\pm}$) and of the correct handedness, the stray field generated by a coherent spin wave can drive coherent NV spin rotations (*Rabi oscillations*, chapter 3) at a rate that is given by the Rabi frequency:

$$\Omega_R^{\pm} = \frac{\gamma}{\sqrt{2}}|B_x^{\mathrm{NV}} \mp iB_y^{\mathrm{NV}}|$$ (2.21)

Here B_x^{NV} and B_y^{NV} are the complex contributions of the transverse components of the stray field projected on the NV axis (defined along z^{NV}), as denoted by the superscript NV and where the $\mp$ refers to driving the $|0\rangle \leftrightarrow |\mp 1\rangle$ transition. From Eq. 2.21, it is clear that circularly polarized fields of opposite handedness are required to drive the two ESR transitions. This preferential NV Rabi driving by a field of a specific handedness is essential when detecting spin waves.

We will now illustrate this difference in Rabi frequency for the model situation in which the axis of the NV spin aligns with the magnetization such that the magnet and NV frames overlap. We distinguish between the stray fields generated by spin waves travelling parallel (BV spin waves) or perpendicular (DE spin waves) to the magnetization:

2

BV spin waves are characterized by $k_y = 0$, such that $B_x \propto -\delta m_x$ and $B_y = 0$ (Eq. 2.20). We, therefore, find that BV spin waves generate an equal Rabi rate along both ESR transitions for both left- and right-travelling spin waves:

$$\Omega_{R,\text{BV}}^{\mp} = \frac{\gamma}{\sqrt{2}} |B_x| = \frac{\gamma}{\sqrt{2}} |A_k \delta m_x| \tag{2.22}$$

DE spin waves are characterized by $k_x = 0$, such that $k_y/k \to \text{sign}(k_y)$, $B_x = A_k(-\delta m_x + i \text{sign}(k_y) \delta m_y)$ and $B_y = -i \text{sign}(k_y) B_x$ (Eq. 2.20). Since both B_x and B_y are non-zero, their phase relation becomes important, generating circularly polarized fields of a different handedness depending on the travel direction and yielding the following Rabi rates:

$$\Omega_{R,\text{DE}}^{-} = \frac{\gamma}{\sqrt{2}} |B_x(1 + \text{sign}(k_y))| = \begin{cases} 0 & \text{for} \quad k_y \leq 0 \\ \sqrt{2}\gamma |A_k \delta m_y(\eta + 1)| & \text{for} \quad k_y > 0 \end{cases} \tag{2.23a}$$

$$\Omega_{R,\text{DE}}^{+} = \frac{\gamma}{\sqrt{2}} |B_x(1 - \text{sign}(k_y))| = \begin{cases} \sqrt{2}\gamma |A_k \delta m_y(\eta - 1)| & \text{for} \quad k_y < 0 \\ 0 & \text{for} \quad k_y \geq 0 \end{cases} \tag{2.23b}$$

Where we used the parameter η, which describes the ellipticity of the spin-wave precession[i], and that the precession of spin waves is right-handed, which enabled substituting $\delta m_x = -i\eta \delta m_y$ and $B_x = i A_k \delta m_y(\eta + \text{sign}(k_y))$.

To conclude, we see that for an NV that aligns with the in-plane magnetization, the DE spin-wave generated field has a handedness that depends on their travel direction and, therefore, preferentially drives either the f_- or the f_+ ESR transition. In fact, the rate along f_+ vanishes entirely for a spin-wave precession that is perfectly circular ($\eta = 1$), which is the case if k becomes large[58]. This is very different for BV spin waves that generate an equal Rabi rate along both ESR transitions that are not dependent on the direction of the spin wave.

2.4.2. SPIN-WAVE EXCITATION VIA A MICROWAVE STRIPLINE

In the previous paragraph, we calculated the NV Rabi frequency caused by coherent spin waves. Now, we briefly sidetrack and explain which wavevector spin waves are excited via the inductive coupling to the stray field of a microwave stripline, the method employed in this thesis to excite coherent spin waves.

In our work, we use a long stripline, e.g., with length $L_{\text{SL}} \approx 1\,\text{mm}$, width $w_{\text{SL}} \approx 15\,\mu\text{m}$, and thickness $t_{\text{SL}} \approx 200\,\text{nm}$, yielding an essentially one-dimensional spin-wave excitation geometry with a negligible in-plane component of the stray-field along the length of the stripline. For such a stripline, the two non-zero components of the effective mag-

---

[i]The spin-wave ellipticity can be calculated using: $\eta = \frac{|S_{xx}|}{|S_{yx}|} = \frac{|S_{xy}|}{|S_{yy}|} = \sqrt{\frac{\omega_3^2}{\omega_2 \omega_3}} = \sqrt{\frac{\omega_3}{\omega_2}}$, where we used the resonance condition $\omega = \sqrt{\omega_2 \omega_3}$ and which is valid in the limit of $\alpha = 0$.

netic field in reciprocal space were derived in the supplement of Ref.[58]:

$$\tilde{B}_{AC;x_{SL}} = -2i\mu_0 J(\omega) \frac{1-e^{-kt}}{kt} \frac{e^{-kt_{SL}}-1}{k^2} \sin\left(k_{z_{SL}} \frac{w_{SL}}{2}\right) \frac{\sin\left(k_{y_{SL}} \frac{L_{SL}}{2}\right)}{k_{y_{SL}}} \tag{2.24a}$$

$$\tilde{B}_{AC;y_{SL}} = i \frac{k}{k_{y_{SL}}} \tilde{B}_{AC;x_{SL}} \tag{2.24b}$$

Here the length of the stripline is along z_{SL}, and the out-of-plane coordinate is along x_{SL}. J is the current density at the drive frequency ω, μ_0 is the vacuum magnetic permeability, and the factor $\frac{1-e^{-kt}}{kt}$ follows from averaging the stripline field over magnetic film thickness t, again assuming no magnetization variations occur across the film thickness, yielding an effective magnetic field for spin-wave excitation.
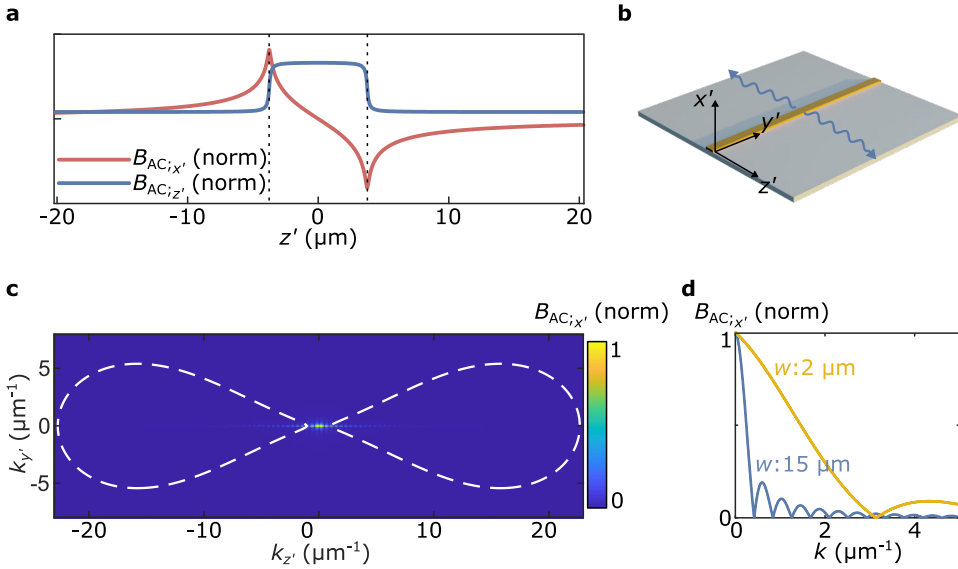
Figure 2.5: Field of a long stripline aligned perpendicular to the magnetization enabling the efficient excitation of backward-volume spin waves. The field is generated by a stripline with length $L_{SL} = 1\,mm$ and width $w = 15\,\mu m$. (a) Real-space components of the stripline field. Depending on the stripline's orientation with the magnetization, its stray field either excites backward volume (BV) spin waves ($L_{SL} \perp m_{eq}$) or Damon Eshbach (DE) spin waves ($L_{SL} \parallel m_{eq}$). (b) Illustration showing a stripline (yellow) exciting spin waves travelling perpendicular to the stripline length. (c) Out-of-plane component of the stripline field in reciprocal space (Eq. 2.24a) in the BV geometry ($L_{SL} \perp m_{eq}$). The dashed line represents the iso-frequency contour of spin waves resonating with f_- at $B = 35\,mT$ and $\theta_B = 0.95$ (as in Fig. 2.4). The excitation efficiency is negligible for DE spin waves ($k_z = 0$) and highest for low-k BV spin waves ($k_y = 0$). (d) By choosing a narrower stripline of $w = 2\,\mu m$, we enhance the relative excitation efficiency for higher k-spin wave modes.

To excite spin waves of a specific wavevector, the drive field (Eq. 2.24) must have a non-zero amplitude at that wavevector. Therefore, to excite BV spin waves, we align the stripline perpendicular to the magnetization (Fig. 2.5a-c, $L_{SL} \parallel y$). In this orientation, the out-of-plane component of the stripline field couples to BV spin waves, while

the in-plane component of the stripline field aligns with the equilibrium magnetization ($\tilde{B}_{AC;y_{SL}} \parallel z$) and therefore does not contribute to spin-wave excitation in our linear approximation. We find that this geometry yields a symmetric excitation efficiency for both left and right travelling spin waves:

$$\delta m_y \propto i\omega \tilde{B}_{AC;x_{SL}}, \quad \text{when} \quad L_{SL} \parallel y \tag{2.25}$$

To efficiently excite DE spin waves, we align the stripline parallel to the magnetization so that the stripline and magnet frame overlap. Now both stripline field components couple to the transverse magnetization, yielding (in the limit of zero Gilbert damping):

$$\delta m_y \propto i\omega \tilde{B}_{AC;x_{SL}} + \omega_2 \tilde{B}_{AC;y_{SL}} = -i\omega_2 \tilde{B}_{AC;x_{SL}}(\eta + \text{sign}(k_y)), \quad \text{when} \quad L_{SL} \parallel z \tag{2.26}$$

where we used $\frac{k}{k_y} \to \text{sign}(k_y)$ for DE spin waves and inserted the definition of the spin-wave ellipticity parameter η. We find that the stripline field is efficient in exciting DE spin waves that travel to the right, while the spin-wave excitation efficiency vanishes for DE spin waves travelling to the left.

In the previous two paragraphs, we found that chirality plays a prominent role in detecting and exciting DE spin waves. We can now summarize the reasons that cause the enhanced Rabi frequency along the f_--ESR transition on the right-hand-side of the spin-wave excitation stripline, which helps understand chapter 5, where we study the directional excitation of spin waves:

- A large amplitude spin-wave field with a matching handedness for driving $|0\rangle \leftrightarrow |-1\rangle$ NV spin rotations (Eq. 2.23a).

- A preferential excitation of $+k_y$ spin waves by the stripline (Eq. 2.26).

- The confinement of the field generated by DE spin waves to the bottom/top surface for left/right propagating DE spin waves[73].

Finally, we note that, due to a wavenumber mismatch, wide striplines do not efficiently excite high-k-modes (Fig. 2.5c). By reducing the width of the stripline w, one can enhance the relative efficiency to excite higher-k spin waves (Fig. 2.5d). However, below a certain width, the real part of the stripline impedance increases, hampering the excitation of small wavelength spin waves[77]. To increase the wavenumber excitation cut-off, one can use more advanced geometries such as nanogratings[81] or magnetic coplanar waveguides[82].

IMAGING OF COHERENT SPIN WAVES

So far, we have shown how to determine the amplitude of a coherent spin wave by measuring the Rabi frequency of a proximal NV centre. To achieve sensitivity to the local phase of the spin-wave stray field and to determine the spin wavelength in imaging experiments, we let the spin-wave field interfere with the spatially homogeneous (on the scale of the spin-wavelength) stripline field. This results in a Rabi frequency that spatially varies with a period set by the spin wavelength (Fig. 2.6):

$$\Omega_R = \frac{\gamma}{\sqrt{2}} |B_{SW}^0 e^{ik(x-x_0)} + B_{AC}| \tag{2.27}$$

Here B_{SW}^0 and B_{AC} are the components of the spin-wave and stripline field that rotate with the correct handedness in the plane perpendicular to the NV-axis.
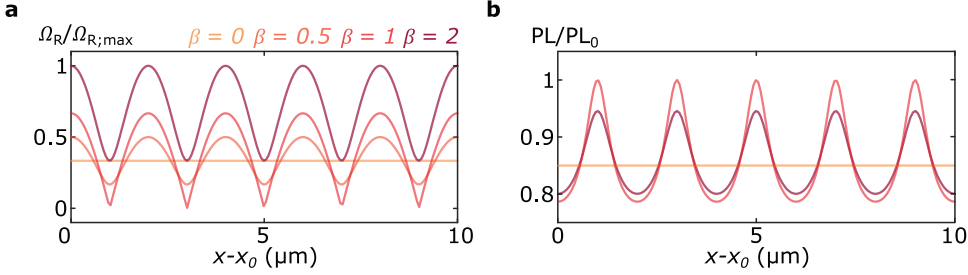
Figure 2.6: Spatial profile of a single spin-wave mode interfering with a reference field. (a) The expected Ω_R for various strengths of the reference field, where we define $B_{SL} = \beta B_{SW}^0$. For $\beta = 0$, there is no spatial contrast. (b) The expected PL/PL_0 that we defined as: $PL/PL_0 = 1 - C_{ESR}$ where $C_{ESR} = C_{max} \frac{\Omega_R^2}{\Omega_R^2 + \Phi^2}$ where C_{max} describes the maximum ESR contrast and Φ describes a parameter that depends on the optical pumping rate [33] which we fix here to be constant (see chapter 3).

2.4.3. INCOHERENT MAGNETIC FIELD NOISE FROM THERMAL SPIN WAVES

Up to this point, we discussed the excitation and detection of coherent spin-wave modes with a well-defined wavevector $\vec{k}$ and showed how microwave magnetic imaging experiments enable extracting the spin-wavelength.

We have yet to discuss the spin waves that are present even without external driving and how they affect the spin state of a nearby NV centre. Namely, at a finite temperature, thermally excited magnons occupy the whole spin-wave band following a Rayleigh-Jeans distribution[73, 79] where the average number of magnons in a spin-wave mode of frequency ω is given by: $n(\omega) = \frac{k_B T}{\hbar \omega}$ [ii]. Although the associated magnetic signals are incoherent and do not drive coherent NV spin rotations, this magnon gas generates magnetic field noise that causes relaxation of the spin state of a nearby NV centre.

To understand how we can compute the magnetic amplitude of thermal spin-wave noise, we first consider that the dynamic susceptibility of a many-particle system is related to the functions that describe the correlation between the system's constituents, following the fluctuation-dissipation theorem [83]. Hence, for a magnon gas, we can write the correlation function between individual spins as:

$$C_{ij}(\vec{r} - \vec{r}', t - t') = \langle \delta m_i'(\vec{r}, t) \delta m_j'(\vec{r'}, t') \rangle \tag{2.28}$$

For a spin-wave system that is at thermal equilibrium, we can rewrite this in terms of the magnetic susceptibility that we defined in the Fourier domain, following Ref.[73]:

$$C_{ij}(\vec{k}, \omega) = 2D_{th} \sum_{\nu = \{x, y\}} S_{i\nu}(\vec{k}, \omega) S_{j\nu}(-\vec{k}, -\omega) \tag{2.29}$$

[ii] Assuming $k_B T >> \hbar \omega$

where $D_{\text{th}} = \frac{\alpha k_B T}{\gamma M_s L}$, with k_B the Boltzmann constant.

Subsequently, we calculate the associated magnetic fields while remembering Eq. 2.17, such that we obtain the autocorrelation function of the magnetic field noise produced by a thermal occupation of magnons:

$$\langle B(t)B(0)\rangle = \int \frac{d\vec{k}}{(2\pi)^2} \sum_{i,j\in\{x,y\}} D_{\pm i}(\vec{k})D_{\mp j}(-\vec{k})C_{ij}(\vec{k},\omega_{\mp}) \tag{2.30}$$

Where we integrate over the magnetic fields produced by thermally occupied spin-wave modes at the NV frequency $\omega_{\mp}$, and with $D_{\pm v} = D_{xv} \pm iD_{yv}$ with D_{ij} the components of the dipolar tensor describing the stray fields generated by the transverse spin fluctuations (Eq. 2.18), for simplicity, we again assumed that the equilibrium magnetization lies in the plane so that the lab and magnet frames overlap.

To compute how the magnetic noise affects the NV spin state, we follow Refs.[73, 84–86], that have derived the NV relaxation rates along the NV ESR frequencies $f_{\pm}$ in the presence of an incoherent field using Fermi's golden rule:

$$\Gamma_{\mp}(\omega_{\mp}) = \frac{\gamma^2}{2} \int_{-\infty}^{\infty} dt\, e^{i\omega_{\mp}t} \langle B_{\pm}^{\text{NV}}(t)B_{\mp}^{\text{NV}}(0)\rangle \tag{2.31}$$

Here $\Gamma_{\mp}$ are the NV relaxation rates corresponding to the $\omega_{\mp}$ ESR frequencies, and γ is the electron gyromagnetic ratio. Additionally, $B_{\pm}^{\text{NV}} = B_x^{\text{NV}} \pm iB_y^{\text{NV}}$ is the component of the perturbing field that is transverse to the NV symmetry axis, causing spin transitions between $|0\rangle \leftrightarrow |\mp 1\rangle$.

We can now use the result from Eq. 2.30 to write down the NV relaxation rate in terms of the magnetization correlations[73]:

$$\Gamma_{\mp}(\omega_{\mp}) = \frac{\gamma^2}{2} \int \frac{d\vec{k}}{(2\pi)^2} \sum_{i,j\in\{x,y\}} D_{\pm i}(\vec{k})D_{\mp j}(-\vec{k})C_{ij}(\vec{k},\omega_{\mp}) \tag{2.32}$$

which is again defined for the simplified case where the NV and magnet frames overlap; Calculating the magnetic noise for an NV aligned at a general angle to the magnetization first requires rotating the dipolar tensor as described in Ref[73]. To conclude, Eq. (2.32) shows that the NV relaxation rates give access to the power spectral density of the spin-wave stray fields at the NV frequencies without having to perturb the spin-wave system using, e.g., microwave excitation of spin waves.

2.4.4. Wavenumber-dependent filtering function
Tuning the NV-sample distance can act as a wavelength filter for detecting frequency-degenerate spin waves, enabled by the exponential decay of the spin-wave stray fields on a length scale set by the spin-wavenumber (Fig. 2.7):

$$B_{\text{SW}} \propto f_k = ke^{-kd} \tag{2.33}$$

where f_k is the filtering function which peaks at $k = 1/d$ (Eq. 2.20, Fig. 2.7a).

We use this in chapter 6 when imaging frequency-degenerate coherent spin waves of varying wavelengths at different NV-sample distances. By decreasing the NV-sample distance, we increase the relative contribution of high k-spin waves to the stray-field signal. In chapter 5, we use this principle to study the wavenumber content of the thermal magnon gas by their rapidly decaying magnetic stray fields (Fig. 2.7b).
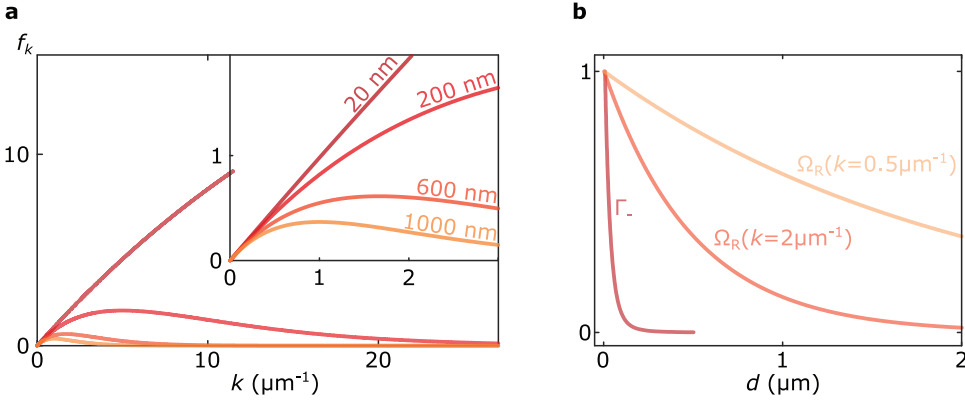
Figure 2.7: Spin-wave filtering action of the NV-sample distance. (a) The spin-wave stray field is proportional to a prefactor f_k (filter function) that depends on the NV-sample distance d. The filter function peaks at $k = 1/d$, where k is the spin-wavenumber. The filter function is plotted for several values of d. (b) Calculation comparing the NV relaxation rate Γ_- caused by thermal spin waves to the NV Rabi oscillation rate caused by a coherently driven spin wave. Both rates are normalized to their value at $d = 0$ to highlight the different scaling with distance. The calculation of Γ_- assumes an equal population of all spin-wave modes at frequency f_- as expected for a Rayleigh-Jeans distribution[73]. The calculation of Ω_R assumes only a single spin-wave mode with wavenumber $k = 2\mu m^{-1}$ (or $k = 0.5\mu m^{-1}$).

3

NV MAGNETOMETRY

The nitrogen-vacancy (NV) centre in diamond is an atomic-sized magnetic field sensor. In this chapter, we discuss the physics of the NV centre relevant to understanding the working principles of NV magnetometry (§3.1). First, we explain the Zeeman interaction of an NV spin in a magnetic field which causes an energy level splitting of the NV's spin sublevels. We describe a standard measurement that utilizes the NV's spin-dependent photoluminescence to obtain the NV electron spin resonance frequencies. These frequencies provide a precise measurement of the magnetic field at the NV site (§3.2). Second, we describe three measurement modalities that enable the detection of oscillating magnetic fields, such as the stray fields produced by coherent or incoherent spin waves (§3.3). Finally, we describe the experimental setup built to perform the measurements in this thesis (§3.4).

3.1. A FLUORESCENT SPIN IN DIAMOND

T HE nitrogen-vacancy centre is an atomic defect consisting of a substitutional nitrogen atom adjacent to a vacancy in the diamond carbon lattice (Fig.3.1a). This configuration with dangling bonds from the carbon and nitrogen atoms gives rise to an electronic state in the vacancy. When the NV centre captures an additional electron from a nearby donor, it obtains a negative charge: NV$^-$ [87]. The negatively charged NV centre, which we refer to as NV centre from here on, has convenient spin and optical properties that are useful for magnetometry:

The NV centre has a $S = 1$ spin triplet configuration. The zero-field quantization axis points along the line connecting the nitrogen and vacancy sites[88], which can have four different directions as determined by the diamond's crystal structure[89]. Its position within high-purity single-crystal diamond ensures that the NV spin state can have a long lifetime of several ms at room temperature, limited by thermal phonons[31, 32].

The NV centre is optically active and has a spin-selective transition into a metastable dark state. This enables spin initialization via non-resonant optical excitation and optical readout through spin-dependent photoluminescence (PL)[90]. These convenient spin-optical properties, combined with its long spin-lifetime, have made the NV a building block in advancing quantum technologies [91, 92] such as quantum computing[34, 35], quantum networks[36, 37] and quantum sensing [38–40].
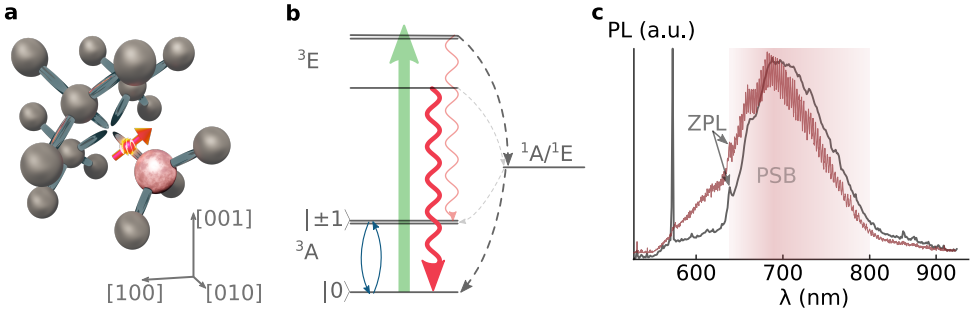
Figure 3.1: The nitrogen-vacancy (NV) centre in the diamond lattice and its spin-optical properties (a) Diamond carbon (grey) lattice with a substitutional nitrogen atom (pink) adjacent to an empty lattice site forming the NV centre lattice defect. The bond between the nitrogen atom and the vacancy is referred to as the NV-axis, which can point along any of the four bond directions in the diamond crystal. The pink arrow represents the NV spin, which we drew in a random direction for visibility. The coordinate system defines the orientation of the lattice vectors. (b) Energy level structure of the NV centre and its optical excitation/decay paths (spin-conserving, solid arrows) and non-radiative decay paths (grey dashed arrows). A 532 nm laser (green arrow) excites the NV from the ground triplet state (^{3}A) to the excited triplet state (^{3}E). Decay to the ground state can occur radiatively, generating red photoluminescence (PL; wiggly red arrows). The second path is via the singlet states (^{1}A/^{1}E), which is optically dark with a negligible decay rate for $m_s = |0\rangle$ compared to $m_s = |\pm1\rangle$, leading to a spin-dependent PL. Blue arrows describe the ESR transitions between $|0\rangle \leftrightarrow |\pm1\rangle$, mediated by microwave magnetic fields. (c) Spectrum under 532 nm excitation of two different diamonds: a diamond with NVs distributed through the bulk (grey) and one with a layer of NV centres implanted ~10 nm below the surface (red). The grey graph shows an NV$^-$ zero phonon line (ZPL) at 637 nm, and a broad phonon sideband (PSB; ≈ 650-850 nm) with >90% of the NV PL. The red graph shows a more substantial contribution for wavelengths $< \lambda_{ZPL}$, indicating a larger contribution of NV^0 due to surface proximity[93].

To understand the NV's spin-dependent optical properties, we first describe its energy level structure (Fig. 3.1b). Here, the spin-triplet ground state consists of three spin sub-levels where the $m_s = |\pm 1\rangle$ states are split via the zero-field splitting ($D = 2.87\,\text{GHz}$) from the $m_s = |0\rangle$ state, due to spin-spin interactions. At room temperature, the electronic excited state can also be described as a spin-1 manifold, but with a zero-field splitting of $D_{\text{ex}} = 1.42\,\text{GHz}$. Finally, there exist two intermediate states that have a singlet spin configuration[29, 33, 87, 94, 95].

Optical pumping from the ground state allows for spin-conserving transitions to the excited state, which has a lifetime of $\approx 13\,\text{ns}$ for NVs in bulk diamond[33]. At room temperature, the existence of vibrational modes allows for off-resonant pumping using standard green lasers ($\lambda \approx 532\,\text{nm}$) [28]. The subsequent decay to the ground state can occur via two distinct paths:

Firstly, via the same optical and spin-conserving transition while emitting into the zero phonon line (ZPL) or the broad phonon side band (PSB) via electric two dipoles that are in the plane perpendicular to NV axis (Fig. 3.1c)[96].

And secondly, via decay into the metastable singlet states, an optically dark transition, also referred to as intersystem crossing[29, 95]. Interestingly, the decay rate towards the singlet states is much higher for the $m_s = |\pm 1\rangle$ states, leading to reduced PL compared to $m_s = |0\rangle$ as well as an efficient spin-polarization into the $m_s = |0\rangle$ spin state under continuous illumination [28, 33, 87, 94, 95, 97].

To conclude, the NV centre represents a stable spin system with long coherence times, even at room temperature. Combined with the optical readout and initialization measurement scheme, it presents an excellent platform for magnetic sensing at the single spin level, as we will discuss below[47, 98, 99].

3.2. A SINGLE-SPIN SENSOR FOR MAGNETIC FIELDS.

To explain how we use the NV spin as a sensor for magnetic fields, we take a closer look at the NV spin Hamiltonian in the electronic ground state, where we define z to be along the NV axis:

$$H = DS_z^2 + \gamma \vec{B} \cdot \vec{S} \tag{3.1}$$

with units of Hz and where $\gamma = 28\,\text{MHz}\,\text{T}^{-1}$ is the electron gyromagnetic ratio and with $\vec{S} = [S_x, S_y, S_z]$, the spin-1 Pauli matrices. The first term describes the aforementioned zero-field splitting. The second term describes the Zeeman energy splitting of the spin states in a magnetic field $\vec{B}$.

For the NV spin-triplet, electron spin resonance (ESR) transitions corresponding to $\Delta m_s = 1$ can be driven using microwave fields resonant with the NV ESR frequencies: $f_\pm = |f_{|\pm 1\rangle} - f_{|0\rangle}|$. For a magnetic field B_0 aligned along the NV axis, the NV ESR frequencies become $f_\pm = D \pm \gamma B_0$, from which it is clear that measuring $f_\pm$ enables the extraction of the magnetic field (Fig. 3.2a).

One method to obtain $f_\pm$ is by monitoring the NV's spin-dependent PL in a continuous wave optically detected magnetic resonance measurement (CW-ODMR). Here, we use continuous illumination to continuously pump the NV spin into the $m_s = |0\rangle$ state. At the same time, we apply a microwave field with a varying drive frequency f_{MW}. At $f_{MW} = f_\pm$, the microwave field can drive the NV ESR transitions, causing a change in population from $|0\rangle$ into the optically darker $|\pm1\rangle$ state (Fig. 3.2b). The microwave power at the NV site determines the ESR transition rate and the amplitude of the ESR contrast C, which has a maximum of $\approx$ 20% under CW illumination[33][i]. The width of the ESR resonance dip $\Delta\nu$ sets the measurement's sensitivity, according to[33]:

$$\eta_{\text{CW-ODMR}} \ [\text{T}/\sqrt{\text{Hz}}] = \delta B_{\min}\sqrt{\Delta t} \approx \mathscr{P}_F \frac{1}{\gamma} \frac{\Delta\nu}{C\sqrt{\text{PL}_0}} \tag{3.2}$$

where we assumed small C and a photon-shot-noise-limited measurement[33]. Here, PL_0 is the PL rate without microwave driving, and $\mathscr{P}_F$ is a numerical prefactor related to the lineshape of the ESR resonance dip that resembles either a Gaussian function such that $\mathscr{P}_F \approx 0.70$ in the limit of low optical and microwave power, or a power broadened Lorentzian function with $\mathscr{P}_F \approx 0.78$[33].

Optimal sensitivity is obtained by tuning the microwave and optical power to obtain high ESR contrast while preventing power broadening that increases $\Delta\nu$ [33, 100]. For ultra-pure diamond with the least amount of impurities, the minimum $\Delta\nu$ is limited by the frequency shifts induced by interactions with nearby nuclei, as described by the inhomogeneous dephasing rate Γ_2^*.

Alternatively, the ODMR sensitivity can be improved by optimizing the PL collection efficiency. One way to do so is by embedding the NV in a diamond waveguide, such as a diamond nanopillar. While normally, a large part of the NV PL remains trapped inside the diamond due to the diamond's high refractive index ($n \approx 2.4$) and total internal reflections at the diamond-air interfaces. Instead, a narrow waveguide may guide the NV PL toward our external collection optics more efficiently and limit the amount of total internal reflections at the diamond's detector side. Shape optimization of the diamond pillar to enhance its waveguiding abilities and the sensitivity of NV magnetometry is an ongoing effort[101–103], and it is one of the goals of our work presented in chapter 4.

When probing an NV ensemble's ESR response, the PL dips at more than two frequencies when the four NV families, corresponding to the four possible NV orientations in diamond, experience different field projections (Fig. 3.2d). These multiple measurements of $f_\pm$ give access to all vector field components, which is one of the advantages of using an NV ensemble.

---

[i]For NV ensembles, the ESR contrast is limited further due to background PL from the other NV families.
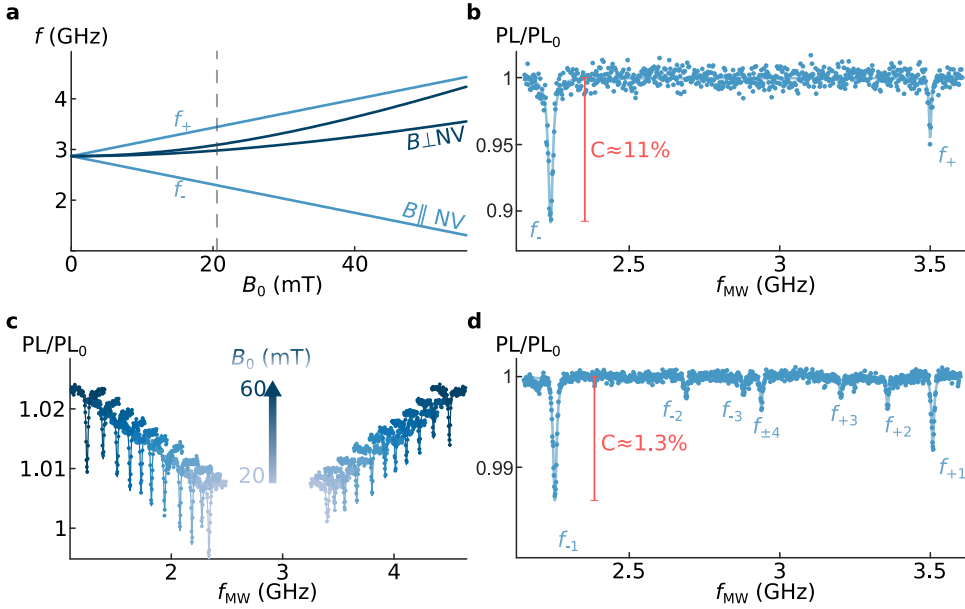
Figure 3.2: Nitrogen-vacancy (NV) electron spin resonance (ESR). (a) The NV ESR frequencies ($f_\pm$) as a function of the magnetic field B_0 applied along (light blue) or perpendicular (dark blue) to the NV axis. (b)-(d) The NV photoluminescence (PL) under microwave driving as a function of the drive frequency f_{MW}. A dip in the PL occurs when $f_{MW} = f_\pm$. The PL is normalized by the PL without microwave driving (PL$_0$). (b) ESR measurement of a single-NV probe at a field of approximately 20 mT along the NV axis (dashed line in (a)). The contrast C depends on the power of the microwave drive. (c) Several ESR traces around $f_\pm$ for increasing field B_0 along the NV axis. (d) ESR measurement focusing on an ensemble-NV probe. The presence of eight dips in the ESR trace indicates that all four NV families experience a different field projection. The solid line is an eight-peak Lorentzian function fitted to the data to obtain the ESR frequencies. The maximum ESR contrast C is smaller than the contrast obtained in (b), which is primarily due to the larger PL background from the other NV families.

3.3. DETECTION OF OSCILLATING MAGNETIC FIELDS

So far, we have discussed how we can measure *static* magnetic fields. Here, we focus on probing *oscillating* magnetic fields that are resonant with $f_\mp$ and drive NV ESR transitions. In particular, we describe the measurement modalities used in this thesis to probe the microwave stray fields generated by spin waves.

3.3.1. ESR CONTRAST

The ESR contrast obtained in the CW-ODMR measurement discussed above depends on the amplitude of the oscillating magnetic field driving ESR transitions via[33]:

$$C_\mp = C_{max} \frac{(\Omega_R^\mp)^2}{(\Omega_R^\mp)^2 + \Phi} \tag{3.3}$$

where C_{max} is the maximum ESR contrast, Φ depends on the optical excitation power and the NV coherence time, and $\Omega_R^\mp$ is the NV Rabi frequency associated with the drive

field amplitude[33]. The NV Rabi frequency describes the NV ESR transition rate along $f_{\mp}$, and it follows the relation[58]:

$$\Omega_R^{\mp} = \frac{\gamma}{2}|B_x^{\text{NV}} \pm i B_y^{\text{NV}}| \tag{3.4}$$

where $B_{x,y}^{\text{NV}}$ are the components of the microwave magnetic field that are transverse to the NV axis (as indicated by the superscript NV).

The ESR contrast provides a simple method for probing variations in low-amplitude microwave fields as it does not require complex pulse sequences that can extend measurement overhead. On the other hand, obtaining a quantitative measure of the microwave field amplitude from the ESR contrast is challenging as it requires calibrating the optical power and measuring the NV coherence time, which determine the parameter Φ in Eq. 3.3[33, 104]. Furthermore, in the case of high-amplitude fields, the ESR contrast saturates, rendering it insensitive to variations in the field. We now describe a pulsing sequence to measure the Rabi frequency directly, allowing for quantitative extraction of the magnetic field amplitude.

3.3.2. COHERENT SPIN ROTATIONS

To measure NV Rabi oscillations, we first initialize the NV in its $m_s = |0\rangle$ state (Fig. 3.3a; top). Next, we apply a microwave pulse of varying duration on the $f_{\mp}$ transition. After the pulse, we read out the spin state by characterizing the spin-dependent PL during the first ~ 500 ns of a laser readout pulse. The microwave pulse rotates the spin state from the bright $|0\rangle$ toward the darker $|\mp 1\rangle$ spin state, depending on the pulse length (τ) and the Rabi frequency. In the reference frame rotating at the NV and drive field frequency ($f_{\mp}$), this rotation is described by an angle $\alpha = 2\pi \Omega_R \tau$. By monitoring the PL as a function of pulse length, we can detect coherent NV spin rotations and extract the associated Rabi frequency (Fig. 3.3a; bottom).

This protocol is useful for studying NV-resonant coherent magnetic fields, such as the stray fields of coherent spin waves excited by a microwave stripline. Below, we discuss a measurement protocol that allows for probing incoherent magnetic fields of which the time dependence is unknown.

3.3.3. SPIN RELAXOMETRY

Fluctuating magnetic fields at a spin's resonance (ESR) frequency cause spin relaxation. As such, characterizing the spin relaxation rates is a powerful method for providing insight into the magnetic noise generated by systems of interest. In particular, the NV spin relaxation rate in the presence of incoherent AC magnetic fields is described by ($\Gamma_{\mp}$)[73, 84–86]:

$$\Gamma_{\mp}(\omega_{\mp}) = \frac{\gamma^2}{2} \int_{-\infty}^{\infty} dt\, e^{i\omega_{\mp}t} \langle B_{\pm}^{\text{NV}}(t) B_{\mp}^{\text{NV}}(0) \rangle \tag{3.5}$$

3
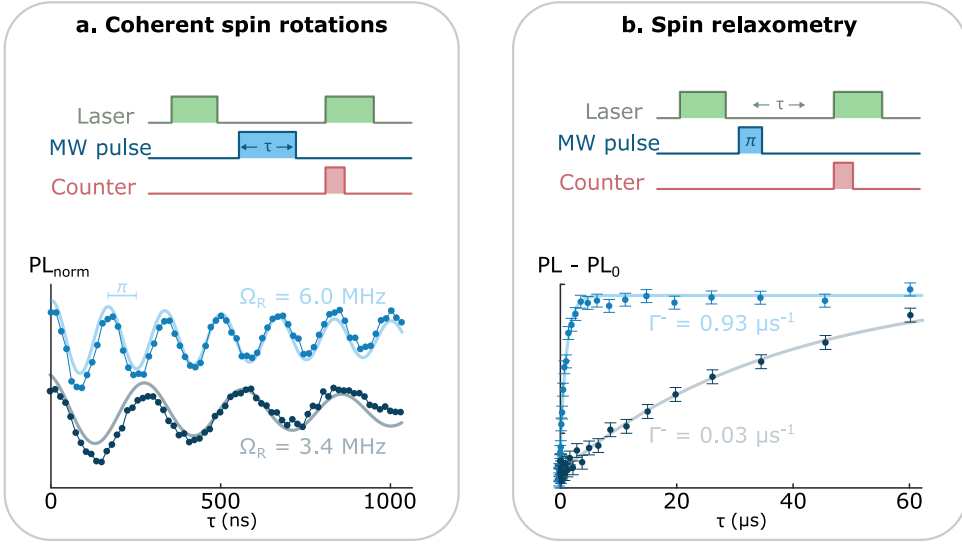
Figure 3.3: Detection of oscillating magnetic fields using NV spin dynamics (a) To detect coherent microwave magnetic fields, we use Rabi measurements. Top: Diagram describing the pulse sequence for the Rabi measurement. A green laser pulse initializes the NV spin into $|0\rangle$. We apply a microwave pulse at f_- that causes the NV spin to rotate coherently between $|-1\rangle$ and $|0\rangle$ as a function of the pulse duration τ. The spin state is optically read out (counter channel) during a final laser pulse. We repeat this sequence without the MW pulse (not shown in the diagram) that we use for normalization. Bottom: Rabi measurements using microwave pulses of a different amplitude. At $\tau = 0$, the NV is initialized to $|0\rangle$, where we measure a bright PL. Half a cycle later ($\tau = \pi$), the NV spin has rotated to the optically darker $|-1\rangle$ state. Since its relaxation time to the steady state is large enough, the NV spin can rotate several periods before it is dephased. (b) Spin relaxometry to characterize magnetic field noise. Top: Diagram describing the pulse sequence for a relaxometry measurement to obtain Γ_-, the NV spin relaxation rate associated with the $|-1\rangle \to |0\rangle$ decay. A green laser pulse initializes the system to $m_s = |0\rangle$. Next, a microwave pulse with duration t_π (as defined in (a)) rotates the spin into $m_s = |-1\rangle$. During a time τ, the spin relaxes back to the steady state. The spin state is read out optically (Counter) during a final laser pulse. We repeat this sequence (not shown in the diagram) without the π-pulse as a background measurement. Bottom: NV relaxation rate along f_- for two different amplitude sources of incoherent magnetic field noise, a nearby magnon gas in thermal equilibrium (dark blue) and a nearby magnon gas that is driven at its ferromagnetic resonance (light blue) to raise its chemical potential[79] (see Chapter 5). Here, the solid lines represent fits to the data using: $PL - PL_0 = Ae^{-2\Gamma^- \tau}$.

as follows from Fermi's golden rule. This equation shows how the relaxation rate between the $|0\rangle \leftrightarrow |\mp 1\rangle$ spin states is determined by the magnetic field power spectral density at the $\omega_\mp$ NV ESR frequencies, with $B_\pm^{NV} = B_x^{NV} \pm i B_y^{NV}$.

To measure $\Gamma_\mp$, we first initialize the NV spin in its $|\mp 1\rangle$ state by applying a laser pulse and a subsequent $\pi_\mp$-pulse on the $|0\rangle \to |\mp 1\rangle$ transition (Fig. 3.3b; top). The duration of the microwave $\pi_\mp$-pulse is determined from a prior Rabi measurement (Fig. 3.3a;bottom). We then let the spin relax over a time τ until we read it out. We repeat this sequence without a $\pi_\mp$-pulse to obtain a background measurement. By subtracting these two measurements, we cancel out spin-independent PL variations caused by, e.g., laser instability or the response from other NV families when interrogating an NV ensemble. Below, we describe the procedure to extract $\Gamma_\mp$ from such a series of measurements for which we vary

the evolution time τ.

First, the PL collected during the readout of the sequence without a $\pi_{\mp}$ pulse is determined via:

$$N(\tau) = p_0(\tau)N_0 + p_{-1}(\tau)N_{-1} + p_{+1}(\tau)N_{+1} + N_{\mathrm{BG}} \tag{3.6}$$

where $N_{i=-1,0,+1}$ are the number of collected photons when the NV is in state $|i\rangle$ and $p_{i=-1,0,+1}$ are the associated occupation probabilities and N_{BG} is the background PL.

Applying a $\pi_{\mp}$-pulse on the $|0\rangle \leftrightarrow |\mp 1\rangle$ transition (of the target NV family) switches the populations of these states. The PL collected during the readout is now:

$$N_{\pi_{\mp}}(\tau) = p_{\mp 1}(\tau)N_0 + p_0(\tau)N_{\mp 1} + p_{\pm 1}(\tau)N_{\pm 1} + N_{\mathrm{BG}} \tag{3.7}$$

By taking the difference of equations 3.6 and 3.7, the background contribution drops out, giving:

$$N - N_{\pi_{\mp}}(\tau) = (p_0(\tau) - p_{\mp 1}(\tau))(N_0 - N_{\mp 1}) \tag{3.8}$$

For the external field range used in our measurements (chapters 5 and 6), f_+ is resonant with short wavelength modes that less affect the spin dynamics of an NV such that $\Gamma_- \ll \Gamma_+$ (for details, see chapter 2 or Ref. [73]). In this case, the NV relaxation dynamics describe that of a two-level system such that the time dependence of $N - N_{\pi_-}$ follows an exponential decay with decay constant: $2\Gamma_-$ (Fig. 3.3b; bottom).

This protocol is useful for probing incoherent magnetic field noise at the NV ESR frequencies, such as those generated by thermally-excited spin waves (chapter 5) [73, 79, 85].

3.4. A SCANNING NV-MAGNETOMETRY SETUP

Here we describe our magnetometry setup built to perform the experiments in this thesis. It consists of a confocal microscope combined with a commercially available atomic force microscope (AFM, Fig. 3.4a). An NV probe is glued to the AFM tuning fork to control the NV-sample positions precisely. We either use custom-made NV probes (see the following chapter 4) or commercially available ones (*Qzabre Ltd* or *Qnami*). We use the confocal microscope to initialize and read the NV spin state optically. Finally, we use on-sample microwave signals to drive NV ESR transitions and to excite spin waves. We will now describe these elements in more detail.
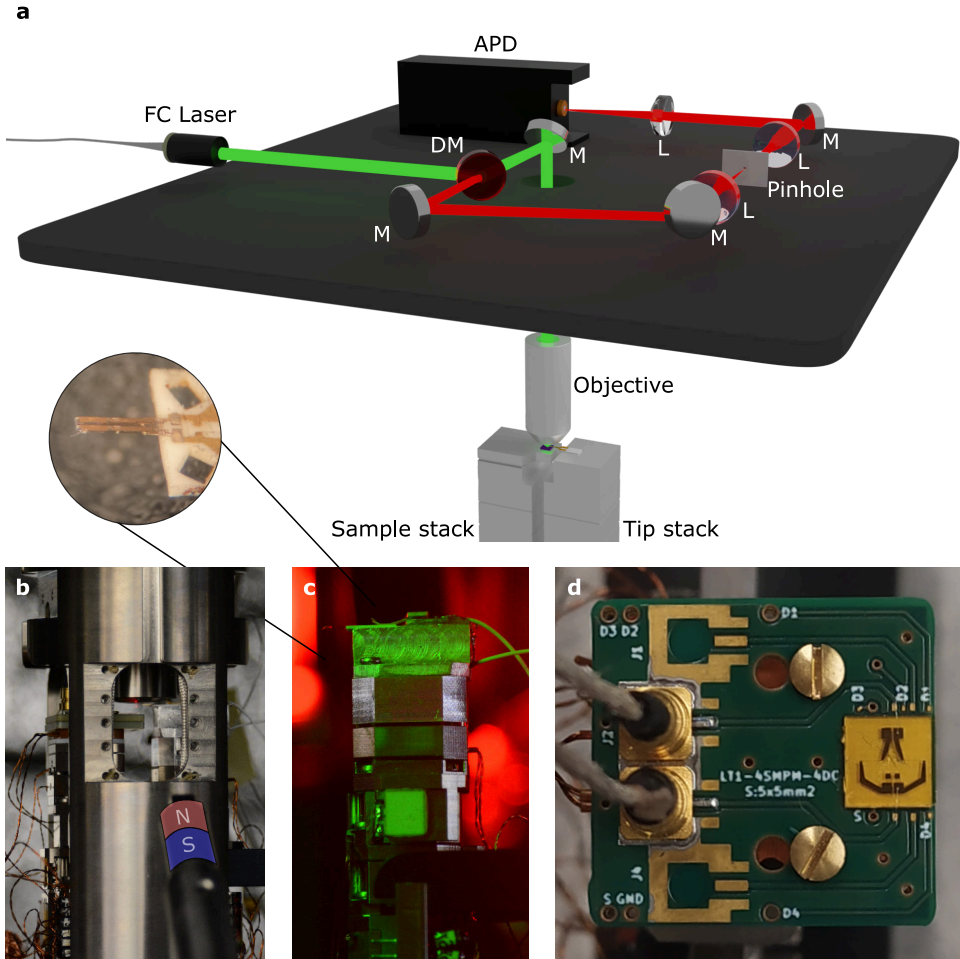
Figure 3.4: Confocal & atomic force microscope for scanning nitrogen-vacancy magnetometry (a) Illustration of the setup with a breadboard and the optical elements used to read out and initialize the NV spin state. Below the breadboard, we mount our NV probe onto an atomic force microscope stage for nanoscale control over the NV-sample distance. A fiber-coupled laser (FC Laser) emits collimated green light (515 nm) towards a dichroic mirror (DM), here the green light reflects towards a mirror (M) and is subsequently focussed by an objective onto the tip of a diamond probe (below breadboard, not visible) which we bring into focus using the positioners and scanners of the tip stack. The NV PL (red light) is collected back by the same objective and follows the excitation path until the DM, where the PL is transmitted and focused (using a lens (L)) onto the avalanche photodiode (APD) (after being filtered via a spatial pinhole filtering system). We use the sample stack to bring a sample near the NV probe and scan the sample underneath the tip. (b) Image of the scanning probe head containing the sample and tip stack (left and right). We use a small magnet that we move towards the tip and sample to tune the external magnetic field B_0 (artificial coloring red (N)- blue (S) to highlight the magnet). (c) Side-view image of the tip stack containing the positioners and scanners used to move the NV probe into the focus of the objective, where the NV probe is glued to an Akiyama tuning fork (inset). The dither piezo is glued below the tip (not visible) and is used for driving the quartz tuning fork. (d) Top view of the sample stack onto which a custom-designed PCB is mounted. Two microwave (MW) cables (SM050, *Dekave Berkel-Enschot*) are connected via SMPM connectors (*Molex*) to a coplanar waveguide that is wire-bonded to an on-sample stripline (right) for NV-spin manipulation. One MW cable is terminated via 50 Ω to the ground.

3.4.1. OPTICAL SETUP FOR NV INITIALIZATION AND READOUT

Our confocal microscope is equipped with a 515 nm laser (*Cobolt 06-MLD, pigtailed*) for off-resonant NV excitation. We use a fibre collimator (*Schäfter+Kirchhoff-60FC-T*) with an adaptable focus to couple the laser out into free space on a compact breadboard (30x30 cm^2). A dichroic mirror (*Semrock Di03-R532-t3-25x36*) reflects the green laser towards a mirror, after which the light is focused by a ≈ 650 μm-working-distance objective lens (*LT-APO/VISIR/0.82*) onto the tip of the NV probe that is below the breadboard. The NV PL is collected via the same path until the dichroic, where it is transmitted and passed to a spatial filter (50 μm pinhole system). Finally, we include an additional long-pass filter (*BLP01-594R-25*) before focusing the PL onto the chip of an avalanche photodiode (APD) (*Excelitas SPCM-AQRH-13*). The PL signal is collected and counted using a data acquisition card (NI DAQ; *National Instruments*). We use a pulse generator (PulseBlasterESR-PRO; *SpinCore Technologies, Inc.*) to generate high-speed pulses for the measurements discussed in (§3.3).

3.4.2. NANOSCALE CONTROL OF THE NV-SAMPLE POSITION

Our AFM (*attoCFM; Attocube*) is equipped with two stacks of closed-loop positioners (*ANPx51/RES/LT*) and open loop scanners (*ANSxy50/LT* and *ANSz50/LT*) that allow for individual positioning of the tip and sample (Fig. 3.4b). We use the NI DAQ card and a scan voltage amplifier (*ANC250*) to control the open loop xy scanners for lateral displacements. The NV probe is glued to a quartz tuning fork (TF; Fig.3.4c, inset; For zoom-in, see Fig.4.6) that is driven by a dither-piezo at its resonance frequency. At close NV-sample distance, the TF's resonance frequency and oscillation amplitude shift slightly, which we measure electronically via the piezo-electric charge accumulation onto one of its electrodes. The charge is converted to voltage via a charge amplifier (HQA-15M-10T, *FEMTO*) and analyzed by our scanning probe microscopy (SPM) controller (*ASC500*). To maintain a constant NV-sample distance when scanning, we use the SPM's feedback control to adapt the position of our sample z-scanner according to the measured TF frequency shift.

3.4.3. MICROWAVES FOR DRIVING THE NV SPIN AND SPIN WAVES

We use microwave signals for driving the NV ESR transitions and for exciting spin waves in our samples. To generate these signals, we use a dual-channel microwave generator (SynthHD (v2) *Windfreak Technologies, LLC*) that we connect to our custom-designed sample-PCB (Fig. 3.4d) via two highly flexible RF cables (SM050; *Dekave*, SMPM-connectors; *Molex*). To improve the flexibility further and prevent the wires from straining the piezo scanners, we strip the plastic part of the shield and the crimp sockets on the PCB side of the cables. On the PCB, we define a coplanar waveguide that we connect to a lithographically-defined on-sample stripline that generates a local microwave field. To amplify the microwave drive, we use a ZHL-16W-43-S+ high power amplifier (*Mini Circuits*), and we use the ZASWA-2-50DRA+ as microwave switches (*Mini Circuits*).

4

DESIGN AND FABRICATION OF DIAMOND FOR NV MAGNETOMETRY

The spin associated with a diamond's nitrogen-vacancy (NV) defect provides a unique tool for studying magnetic phenomena due to its atomic size and spin-dependent photoluminescence (PL). When used in a scanning probe geometry in which the NV centre is embedded just below the apex of a sharp diamond-scanning probe, NV magnetometry can achieve high-sensitivity sensing of evanescent fields due to nanometre NV-sample proximity. Additionally, by optimizing the diamond probe shape, the NV PL is efficiently waveguided toward our collection optics, improving the magnetometer's sensitivity. Using simulations, we show here that the PL collection efficiency from an NV in highly tapered diamond probes enhances twofold compared to conventional cylindrical-shaped probes. We also experimentally realize such highly tapered diamond nanopillars, with tapering angles almost three times higher than obtained using previous protocols. Preliminary optical characterization shows PL rates reaching up to 3 MHz, a promising indication of the high collection efficiency of our probes.

4.1. INTRODUCTION

IN the last decade, the electron spin associated with the nitrogen-vacancy (NV) centre in diamond has been established as a powerful system for high sensitivity magnetometry[29, 44, 98, 99, 105, 106]. NV magnetometry operates across a broad frequency range and is thus applicable for studying a wide variety of magnetic systems: From detecting static magnetic textures in condensed matter systems [41, 107, 108], or paleomagnetic rocks[48, 49] to the detection of the gigahertz oscillating magnetic fields associated with the elementary excitations in magnets [58, 84, 109] or microwave electronic devices [110].

An essential property of the NV centre is its atomic size, enabling a spatial imaging resolution that is only limited by the NV-sample distance. At the same time, the high-purity environment of single-crystal diamond, its host material, yields a long NV spin coherence for high-sensitivity magnetometry. As such, all-diamond scanning-NV probes with an NV just below the diamond probe's apex aim to combine the nanoscale spatial resolution obtained when reaching close NV-sample distance with the sensitivity of a highly coherent single spin sensor [52, 54, 103, 111] (Fig. 4.1). Note that although the coherence of NV centres that reside closer than ~50 nm to the diamond surface degrades [112, 113], this loss in sensitivity is compensated by the larger amplitude of evanescent magnetic stray fields at decreased NV-sample distance.

In addition to enabling nanometre-proximity probing of evanescent stray fields and a high spatial resolution, such an NV in diamond-probe geometry also benefits the magnetometer's sensitivity by improving the NV photoluminescence (PL) collection efficiency. Namely, by embedding the NV in a photonic nanostructure, such as a diamond scanning probe, one can improve the out-coupling of the PL at the detector side of the diamond.

Established diamond photonic structures for optimized PL collection efficiency are diamond solid immersion lenses (SILs) with a prelocated NV centre in the lens focal point [114]. Such devices yield detected single NV-PL rates up to ~1 MHz [115] enabling the high-fidelity readout of the NV spin state, necessary for quantum information applications[94, 116]. Recently, the production of NVs embedded in SILs was scaled up by switching fabrication methods from using focused ion beam milling around a single NV centre to using lithography and reactive ion etching around automatically located NV centres finding record high PL rates of ~4 MHz[102]. For magnetic field sensing, however, such blunt devices with ~100 nm (or more) deep NV centres limit the spatial resolution and sensitivity to evanescent fields due to a large d_{NV}. For that reason, NV probes with small-diameter cylindrical pillars and shallowly implanted NVs are currently the standard for scanning NV magnetometry[52, 111, 117].

This chapter describes the fabrication of such cylindrical probes following protocols originally developed by Refs. [52, 111]. Since there was no experience with the nanofabrication of diamond in our lab prior to this work, a key challenge was to implement these protocols in our cleanroom facilities (§4.2-4.3). These efforts led to the fabrication of our first generation of NV probes used in chapter 5 for the magnetic imaging of spin

waves. In addition, they formed the basis for the diamond fabrication in several ongoing projects in our group, such as the fabrication of micron-sized diamond membranes[75] and diamond nanobeams compatible with fibre-based optics[118].

In the second part of this chapter, we show our progress in fabricating a new generation of NV probes with an optimized pillar shape for larger PL collection efficiency and using a protocol that produces reliable fabrication results (§4.4). Specifically, we start in §4.4.1 by simulating the PL emission in conical diamond nanopillars with varying tapering angles, where we extend the range of tapering angles studied in Ref.[101]. We find that increasing the tapering angle above 5° can enhance the NV PL collection efficiency twofold compared to cylindrical pillars. Next, we experimentally realize such large tapering angle diamond nanopillars ($\alpha > 12°$) using a masking method that relies on resist reflow and a silicon nitride (Si_3N_4) mask (§4.4.2). We show that we can implement this method into the scanning NV probe fabrication process without introducing additional steps in the already lengthy protocol (§4.4.3), yielding ~3 µm long semi-conical pillars with tapering angles of ~14°. Finally, in §4.4.4, we discuss a preliminary optical characterization of our new NV probes, showing PL rates reaching up to 3 MHz and a good electron spin resonance (ESR) contrast, similar to the current state-of-the-art presented in Ref. [103] using truncated parabolic-shaped pillars. Therefore, our new protocol, involving a reliable etch mask material and no additional gasses in the diamond etch procedure, presents an accessible alternative for fabricating high-collection efficiency NV probes for high-sensitivity scanning NV magnetometry.
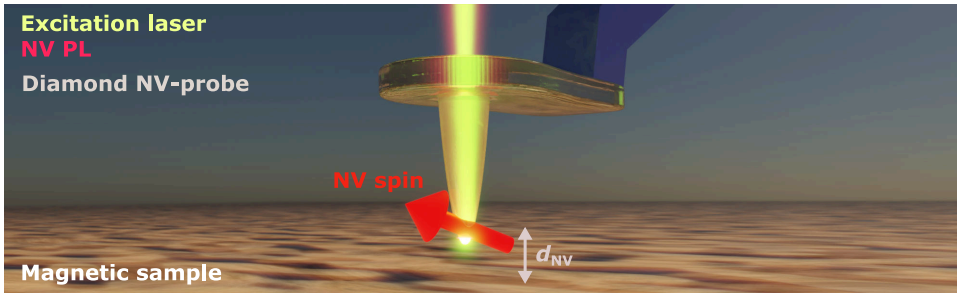
Figure 4.1: Illustration of an all-diamond scanning NV probe for imaging evanescent magnetic stray fields. By embedding the NV centre in the apex of a sharp diamond probe, it can be brought in nanometre proximity to a sample of interest. The minimum NV-sample distance (d_{NV}) determines the spatial resolution of the magnetometer and its sensitivity to evanescent stray fields. Conveniently, embedding the NV into a nanostructure like the diamond pillar illustrated here improves the NV photoluminescence collection efficiency and the magnetometer's sensitivity.

4.2. CREATION OF SHALLOW NV CENTRES

For the fabrication of NV probes, we use (001)-oriented, electronic grade type IIa diamond which has a very low density of intrinsic defects, typically less than five ppb of nitrogen, as specified by the supplier (*Element six*) [i].

---

[i]For testing the fabrication recipes, e.g., the ones shown in §4.4.2, we use lower cost type diamond (145-500-0549 SC Plate CVD, *Element Six*) without additional polishing (by *Almax easyLab*).

4.2.1. Etch step 0: Removal of polishing induced surface damage

Since surface roughness may trap impurities that introduce charge noise causing decoherence of near-surface NV centres [112, 113], we first prepare the diamond surface:

The diamond is cut and polished with a high-quality finish into eight 2x2x0.05 mm^3 pieces (by *Almax easyLab*), out of an originally 4x4x0.5 mm^3 piece of diamond. After polishing, we clean the diamond samples in fuming nitric acid (10 min, SI Note 4.6.1).

Next, we etch the surface that will host the shallow NV centres using an inductively coupled Ar/Cl (RIE-ICP) plasma (30 min, etch recipe #1, table 4.1) to remove 1-2 μm from the diamond surface that may include impurities and other surface damage introduced by the polishing. Next, we etch another 5-6 μm using an O_2 plasma to remove possible chlorine contamination introduced in the previous recipe (20 min, etch recipe #2, table 4.1)[111, 119–121]. It is key to avoid surface contamination, such as small particles, before etching the surface, as they may act as micromasks and cause surface roughening [122]. In addition, we use a quartz carrier wafer to prevent the redeposition and micromasking of silicon from the standard Si/SiOx wafer during the Ar/Cl etch[111, 121, 123].

Via a topography inspection over a 3x3 μm^2 area using atomic force microscopy (AFM), we find that the polishing and subsequent etching yield a surface roughness average of $R_a = 0.08$ nm and an average maximum height of the roughness of R_z(ISO) = 0.47 nm (SI Note 4.6.2)[ii].

Plasma	F (sccm)	P_{RF} (W)	P_{ICP} (W)	T (°C)	R (nm/min)	Etch material
#1 Ar/Cl	20/30	200	500	30	40-80	Diamond
#2 O_2	50	90	1100	20	200-300	Diamond
#3 O_2	50	70	1000	20	200-300	Diamond
#4 SF_6/He	12.5/10	40	0	20	20-40	Titanium
#5 SF_6/He	12.5/10	30	0	20	15-20	Titanium

Table 4.1: Summary of all recipes used in this chapter for reactive ion etching (RIE) in the Oxford Plasmalab 100. The Oxford Plasmalab 100 is a reactive ion etcher with a separate plasma source to generate an inductively coupled plasma (ICP) with a power that sets the plasma density (P_{ICP}) and a sample bias that can be controlled via a separate source (P_{RF}). The operating pressure is kept at 10 μbar. For etch recipe #1, we use a quartz carrier wafer (*Siegert Wafer*) as the Ar/Cl plasma chemistry also etches silicon and may cause diamond surface roughening [111, 121, 123]. For recipes 2-5, we use a standard SiOx/Si carrier wafer. In column R, we list an indication of the etch rates that can vary over time. Etch recipes #2-3 are similar and are used to etch diamond with high anisotropy, and large etch rates. Both recipes can be used interchangeably, but we mainly used etch recipe #2 for etch step 0 & III and etch recipe #3 for etch steps I & II, creating finer structures such as platforms and pillars. Etch recipes #4-5 (with #5 having a slightly lower etch rate) are used for etching masking materials (titanium, silicon, silicon oxide (HSQ), and silicon nitride) and barely affect diamond.


[ii]Since 2022, Almax easyLab also offers *quantum* polishing, which we found to reduce the surface roughness of single crystal diamond already before etching to $R_a = 0.05$ nm and R_z(ISO) = 0.40 nm

4.2.2. NITROGEN IMPLANTATION AND DIAMOND ANNEALING

Having prepared the diamond surface, we create the NV centres using nitrogen-ion implantation (by *INNOViON*[iii])[iv] (Fig. 4.2a). Due to the low number of intrinsic defects in our high-purity diamonds, practically all defects are created in this step, generating a layer of nitrogen and vacancy defects at a depth and density set by the energy and dose of the implantation (Fig. 4.2b) [124]. For example, to create NVs 10-20 nm below the diamond surface and aiming for an average of about 1 NV/probe, we use an energy of 12 keV, a sample tilt of 7°, and a dose of 2×10^{11} N/cm^2 (Table 4.2) [103]. Here, we assumed a N→NV$^-$ conversion of ≈1% given the implantation energy[124].

After implantation, we use a mixture of sulfuric acid (95-98% H_2SO_4), nitric acid (65% HNO_3), and perchloric acid (60% $HClO_4$) with a 1:1:1 ratio that is kept at a constant temperature of 120°C for 1 h to clean the diamonds (SI Note 4.6.1). This triacid procedure in boiling acid is used to remove graphitic carbon and other surface contaminants from diamond surfaces [119]. However, we recently learned from literature that our maximum operating temperature, limited by the glassware specifications, might not be sufficient to generate oxidation from perchlorate, which requires temperatures of at least 150°C[125]. As such, a thin graphite layer may remain on the diamond, causing a layer of charge noise that can degrade the coherence of our shallow NV centres (SI Note 4.6.1)[112]. We are currently testing a new setup with glassware rated up to higher temperatures to improve our diamond surface treatment.
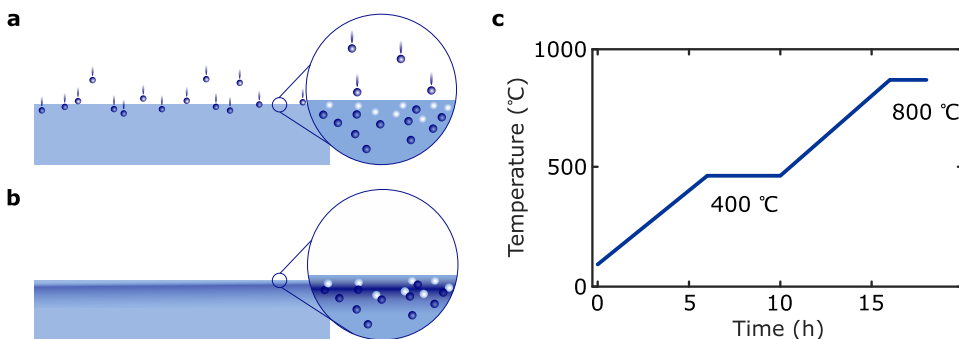
Figure 4.2: Creation of shallow NV centres. (a) Illustration of the nitrogen implantation process in diamond (light blue), where the blue spheres represent the nitrogen ions and the white spheres below the diamond surface the lattice vacancies also caused by the implantation of nitrogen. (b) After annealing, the created NVs are distributed across a layer (indicated by the blue gradient) with a thickness that scales with the implantation depth [124, 126]. The implantation energy determines the depth, while the final density of NVs is determined by several factors, including both the implantation dose and the energy [124]. (c) In our annealing sequence, the temperature in our furnace (*Nabertherm*) is raised from room temperature to 400°C in 6 hours, where we stabilize for 4 hours. Then, the temperature is ramped up to 800°C in 6 hours, where we hold for another 2 hours until we let it cool down to room temperature. During annealing at high temperatures, the vacant lattice sites become mobile and form the NV centres when binding to nitrogen atoms[124, 127]. The pressure is ~3×10^{-6} mbar throughout the process.

[iii]II-VI acquired INNOViON around 2021
[iv]We glue the diamonds to silicon carrier wafers (4") before sending them out for implantation.

Next, we anneal the clean diamonds (Fig. 4.2c) in high vacuum ($\sim 3 \times 10^{-6}$ mbar), during which vacant lattice sites become mobile and pair up with nearby nitrogen ions forming the NV defect[124, 126, 127]. Subsequently, we clean the diamonds again in the high-temperature triacid solution to remove any surface graphite that might have formed during annealing.

Dose (N^{15}/cm^2)	E (keV)	Tilt (°)	Depth (nm)	NVs / pillar
$2 \cdot 10^{11}$	12	7	~20[103]	~1-2
$1 \cdot 10^{13}$	6	0	10-20[128]	~50-100

Table 4.2: Implantation parameters and expected stopping depth. We indicate the expected NV density assuming a yield of approximately 0.5-1% for the implantation energies (E) and sample tilts used in this work[124]. The diamonds are glued to 4-inch silicon wafers during the implantation (SI Note 4.6.3).

4.3. FABRICATION OF SCANNING NV PROBES V1.0

In this section, we describe the fabrication of our first generation of all-diamond scanning NV probes, which we use in chapter 5. A key challenge was implementing the existing fabrication protocols for scanning NV probes, originally developed by Refs. [52, 111], to comply with the facilities available in our cleanroom.

a Etch step I   **b** Etch step II   **c** Etch step III
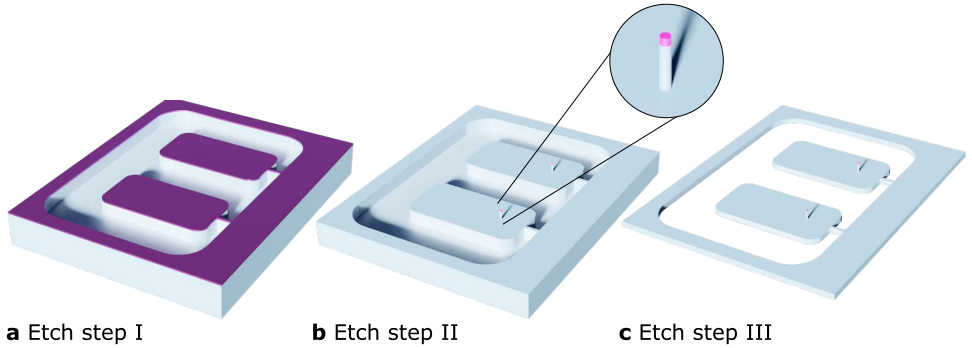
Figure 4.3: Three etch step protocol to fabricate scanning NV probes from a bulk single-crystal diamond, based on Refs.[52, 111]. We start with a clean diamond in which we implant shallow NV centres (§4.2). In this illustration, the NV side is facing up. (a) In etch step I, we use a titanium mask (purple) to create the diamond platforms. (b) In etch step II, we use small-diameter cylindrical masks of flow-able oxide (HSQ-16) (pink) to create cylindrical diamond nanopillars with a ~400 nm diameter. (c) In etch step III, we flip the diamond and release the platforms by etching the diamond's backside.

The fabrication of all-diamond scanning probes is built on three etching steps: In etch step I, we form 20x50 μm^2-sized platforms (Fig. 4.3a). In etch step II, we create the nanopillars (Fig. 4.3b). In etch step III, the platforms are released from the bulk by etching the diamond from the backside, yielding platforms of several microns thick connected to the bulk by only a narrow holding bar (Fig. 4.3c). We will now describe each etch step in more detail:

4.3.1. Etch step I: Defining the platforms

In etch step I, we define the diamond platforms using O_2 etching and a titanium mask (Fig. 4.3a). To create the titanium mask, we first glue the ~2x2x0.05 μm^3 diamond to a ~1 cm^2 silicon carrier chip for ease of handling and to enable spincoating on our small sample. It is crucial the NV surface is clean of particles and facing up (SI Note 4.6.1). Glueing is a critical and finicky step due to the diamond's small dimensions and the glue (PMMA) that can quickly spread on top of our just-cleaned diamond surface (for a short discussion, see SI Note 4.6.3). As such, in the subsequent steps, we want to avoid removing the diamond from its carrier piece as much as possible.

Next, we deposit a 50 nm film of titanium (RF sputtering; *Alliance Concept 450*) onto the diamond-on-carrier. Subsequently, we spincoat at 4000 rpm an 800 nm layer of positive *e*-beam resist (polymethyl methacrylate (PMMA) 950K, A8), which is baked for 3 min at 175 °C[v]. To define the pattern in the resist, we use *e*-beam lithography at a dose of 1600 $\mu C\,cm^{-2}$[vi]. After exposure, we develop the resist in a mixture of methyl isobutyl ketone (MIBK) and isopropanol (IPA) (ratio of 1:3) for 90 s followed by rinsing with IPA for 30 s.

We use a 3 min SF_6/He plasma (etch recipe #4, table 4.1) to transfer the pattern into the titanium film. The titanium film is etched at a rate of $R \approx 20\,nm\,min^{-1}$, while the PMMA mask is etched at a rate of $\approx 240\,nm\,min^{-1}$, yielding a titanium (Ti) etch selectivity of $s_{Ti/PMMA} \approx 0.08$.
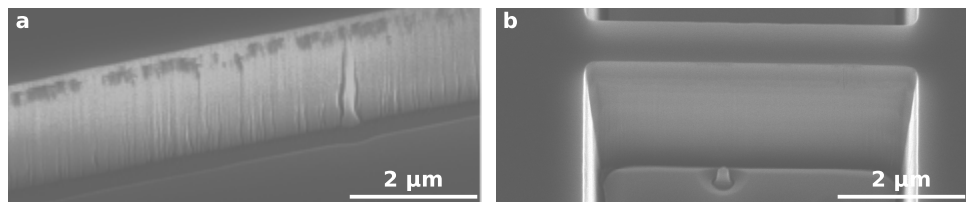
Figure 4.4: Scanning electron microscope (SEM) images of the edge of a single diamond platform after etch step I. Images taken at 30° sample tilt. (a) After RIE-ICP O_2 etching (#3, table 4.1) for 15 min yielding $\approx 3.5\mu m$ thick platforms. (b) After RIE-ICP etching using a cyclic recipe consisting of the following steps: O_2 etching (3 min, #3, table 4.1) - pumping to base pressure (2 min) - SF_6/He etching (10 s, #5, table 4.1), that are repeated four times to obtain the $\approx 3.3\mu m$ platform shown here. The titanium mask is still present in both images but is almost at its end for (b).

Now, we etch the diamond platforms. We use an O_2 diamond etch recipe that is periodically interrupted by an SF_6/He etch. Specifically, we repeat the following steps four times: A 2 min high-bias O_2 plasma (#3, table 4.1), followed by a 10 s low-bias SF_6/He plasma (#5, table 4.1). This cyclic procedure ensures that titanium that is redeposited onto the diamond platform sidewalls and could lead to sidewall roughening is removed. We compare the platform sidewalls with a sample made with a continuous O_2-plasma

---

[v]Spin coating is done right after the titanium deposition for optimal adhesion
[vi]Thicker PMMA layers require higher doses and also a little overdosing in this step is preferred

and observe an improved sidewall smoothness (Fig. 4.4). However, the introduction of SF_6 significantly shortens the titanium mask's lifetime, reducing its diamond (d) etch selectivity from $s_{d/Ti} \approx 250$ without SF_6 (Fig. 4.4a) to $s_{d/Ti} \approx 66$ (Fig. 4.4b).

Finally, we remove the titanium mask by immersing the diamond in hydrofluoric acid (HF, ~10 min, SI Note 4.6.1). Since HF does not affect the glue (PMMA), the diamond conveniently remains on its carrier during this step.

4.3.2. Etch step II: Defining pillars

In etch step II, we create the diamond nanopillars (Fig. 4.3b). To create the etch mask, we use a ~300 nm layer of HSQ (FOx-16, *DuPont*) spincoated onto the diamond-on-carrier at 6000 rpm. HSQ is a negative *e*-beam resist that is highly etch-resistant and is therefore used in many works for etching diamond [52, 101, 111, 117, 129, 130]. Its adhesion to the diamond surface, however, is poor and is often promoted by depositing an adhesion layer before spincoating, such as the 5 nm film of titanium used here [111, 130].

We expose circular patterns with diameters of ~600 nm via *e*-beam lithography, using a $2000\,\mu C\,cm^{-2}$ dose. We develop the pattern in tetramethylammonium hydroxide solution (20 s, TMAH 25%) followed by rinsing in water and IPA.

Prior to structuring the diamond nanopillars, it is essential to remove the titanium sticky layer, as even tiny residues may lead to surface roughening because of titanium's high selectivity (etch for 30 s; etch recipe #4, table 4.1). This is difficult for titanium sputtered onto rough surfaces, underscoring the importance of optimizing the diamond surface roughness prior to and during the etch steps.

Finally, we again use the cyclic etch procedure and repeat the following steps three times: A 2 min O_2-plasma (#3, table 4.1), followed by a 10 s low-bias SF_6/He plasma (#5, table 4.1), creating ~1.5 μm-long pillars with tapering angles of 4-5° (Fig.4.5).
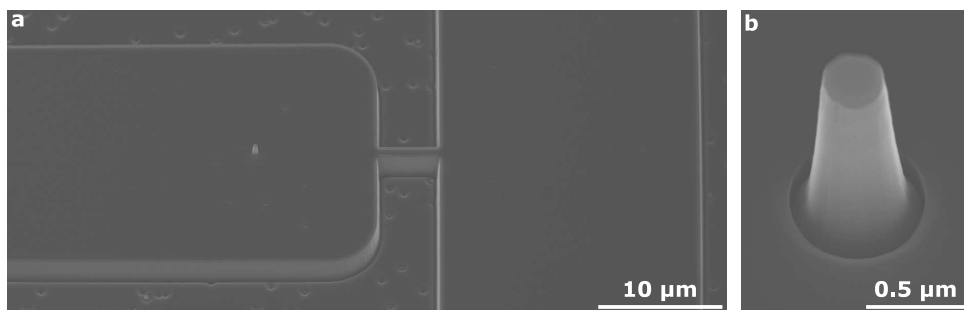
Figure 4.5: Scanning electron microscope (SEM) images of scanning NV probe after etch step II. Taken at a sample tilt of 30°. (a) Scanning probe device. (b) Zoom-in on pillar with a top diameter of 300 nm and a length of approximately 1.5 μm and a tapering angle of about $\theta \approx 5°$. The HSQ-16 mask is not removed yet.

4.3.3. Etch step III: Releasing the devices

For the final etch step, we first protect the NV surface by depositing 50 nm of titanium. Next, we remove the diamond from its carrier and remove the PMMA glue using HNO_3 (100%, SI Note 4.6.1). We then flip the diamond with the NV side facing down into a droplet of PMMA glue[vii] on a quartz carrier wafer. We cover the diamond with a square quartz (or diamond) mask (*Lasertec, Barendrecht*) (as in Refs. [111, 121, 123]) which has a centre-window of 1.2x1.2 mm^2 that exposes the centre of the diamond to the plasma without thinning down its outer edges, such that the diamond maintains its robustness, convenient when handled with tweezers.

Next, we etch the diamond's backside for 90 min using the Ar/Cl plasma (#1, table 4.1), followed by the anisotropic O_2 etch (#2, table 4.1) until the platforms are released. Note that before thinning down the diamond, its thickness must be determined precisely (SI Note 4.6.4). In addition, since etch rates can fluctuate substantially (e.g., #2, table 4.1 can vary between 200-300 nm min^{-1} during the same etch), we monitor the etch-rate in-situ (SI Note 4.6.5). Depending on the stability of the etch rate, we take out the diamond 3-8 μm early and optically inspect if the devices have been released.

We finish the fabrication by gently removing the diamond from its carrier by keeping it in acetone overnight to dissolve the glue. Next, to remove the masking material (HSQ and titanium), the diamond is immersed in HF (40%) followed by a final cleaning step in HNO_3 (100%, SI Note 4.6.1). From the array of ~ 400 fabricated NV probes, we now take a target device and mount it in our confocal -/atomic force microscope by glueing it to a quartz tuning fork (TF) that is used to monitor the NV-sample distance (Fig. 4.6). Here the diamond was implanted with an NV ensemble. Therefore, all fabricated devices contain several NVs and are useful NV probes, as we discuss below. When instead using a diamond with an average density of 1 NV/probe, a prior optical characterization is required to identify useful devices (as we discuss in §4.4.4).
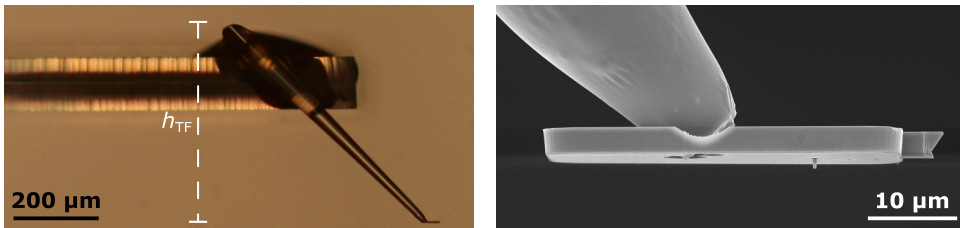
Figure 4.6: An NV probe glued to an atomic force microscope tuning fork (TF). (a) Optical image showing a pulled optical fiber that we glued (UV NOA81, *Norland*) to a TF (Akiyama, *NanoAndMore*) to connect it to the NV probe (SI Note 4.6.6), following Ref.[111]. The top of the fibre is cut-off close to the glueing point, ensuring the total height of the NV probe-to-TF device $h_{TF} \approx 450$ μm is less than the working distance of the objective (i.e., 650 μm). Subsequently, the pulled end of the fibre (right below) is glued to a target NV probe (UV CS20K2, *Thorlabs*). This geometry allows for optical access from the pillar base while it fits within the working distance of the objective lens. (b) SEM image of a (similar) diamond scanning probe with highly smooth etch profiles. The device is coated with a thin titanium layer for visibility.

[vii]We never observed any pillars breaking after this step, indicating that they are robust and that the PMMA sufficiently prevents pressure on the pillars when facing down.

We successfully concluded the in-house fabrication of our first generation of scanning NV probes that have an NV ensemble embedded below their apex. Although ensemble-NV probes do not provide high-resolution imaging, they do enable nm proximity between the NV ensemble and the sample. This ensures sensitivity to evanescent stray fields that rapidly decay from the magnetic surface, such as those of thermal spin waves, as shown in chapter 5. Ensemble-NV probes may also provide higher sensitivity and access to all components of the vector magnetic field. With all four NV orientations at our disposal, we gain experimental flexibility when alignment between the NV and sample and bias magnetic field orientation is required. Finally, with all devices containing several NVs, the yield of useful devices is 100%, a fabrication yield that is currently much lower for our single NV devices (~16%; For details, see §4.4.4).

After using our first generation of NV probes, we found several points of improvement concerning the design and sample fabrication. First, the short pillar length (1.5 μm) requires precise alignment between the platform and a sample. Secondly, several diamond fabrication iterations failed after using HSQ, even when taking great care in handling and storing the resist. In the next part of this chapter, we show that in our newest protocol, we can create longer pillars and exclude the use of HSQ resist, thereby significantly improving the fabrication protocol and device shape.

4.3.4. Membranes for wide-field sensing

We can extend the techniques developed here to other applications. One of those is the fabrication of thin (1-5 μm) diamond membranes with an ensemble of NV centres shallowly implanted below the surface (Fig. 4.7a). Using the micromanipulators of our probe-to-tuning-fork-mounting setup (SI Note §4.6.6), such membranes were recently placed onto a superconducting strip with μm lateral precision to study the interaction between spin waves and superconductors[75] (Fig. 4.7b). Such a diamond-membrane-on-sample geometry also minimizes the NV-sample distance and enables studying evanescent fields in standard confocal or widefield microscopes.
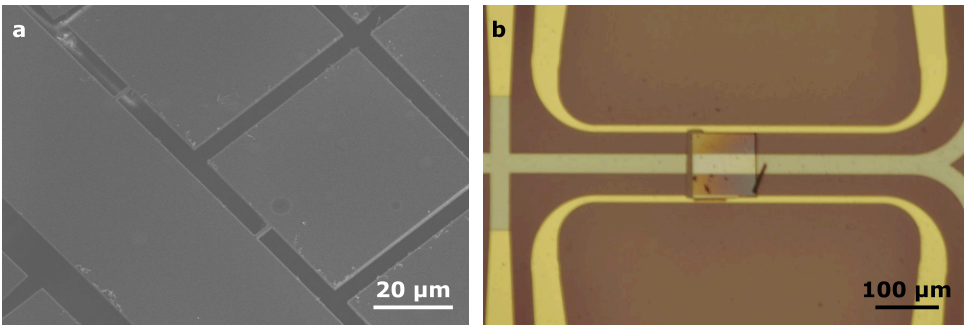
Figure 4.7: Small diamond platforms with NV ensembles for widefield NV magnetometry while ensuring proximity between the NV and sample of interest. (a) Scanning electron microscope image of a diamond etched into small platforms following the protocol described in §4.3 but skipping etch step II. (b) One of the platforms is pushed onto a hybrid superconductor(grey)-on-magnet(pink) device to study spin-wave transport underneath a superconductor. Striplines (yellow) are for spin-wave excitation.

4.4. A NEW GENERATION OF SCANNING NV PROBES

In the next part of this chapter, we present our new generation of scanning NV probes created for two main reasons. First, to improve the fabrication yield. Second, to optimize the NV probe shape for better NV PL collection efficiency and magnetometry sensitivity. We accomplish both goals by using a single mask made from a silicon nitride (Si_3N_4) film for etching platforms and pillars, thereby excluding the use of HSQ resist that has performed unreliably so far. As the Si_3N_4 film is deposited before the first etch step, it forms a well-defined and uniform thickness across the diamond surface. Additionally, this method enhances the pillar tapering angle to about ~14°. Using simulations, we will now first show that such large tapering angles lead to a ~twofold enhancement of the PL collection efficiency compared to cylindrical pillars.

4.4.1. SIMULATING THE NV PL IN CONICAL DIAMOND NANOPILLARS

Here, we use simulations to estimate the PL collection efficiency of NV probes with varying tapering angles up to 25°, extending the range studied in Ref.[101]. We use the finite element simulator COMSOL MultiPhysics in which we define a simulation geometry that represents our diamond probe (n_d = 2.4) with a pillar on top of a platform surrounded by air (n_{air} = 1) (SI Note §4.6.7). We simulate the NV PL emission by an electric dipole situated 20 nm below the probe apex. We consider that PL emission occurs via two electric dipoles oriented in the plane perpendicular to the NV-axis[96] and that there exist four distinct NV directions for our (001)-oriented diamond. It is, therefore, convenient to decompose these dipole contributions into two components that are parallel (*s*) and perpendicular (*p*) to the diamond surface, which can then reconstruct the emission pattern for all four NV orientations[103]. In addition, since the *p*-contribution couples poorly to the probe's waveguide [101, 103], we discard its small contribution and only assess the emission from an *s*-polarized dipole to save computational time.

We start by studying the PL emission for several devices with a fixed pillar length and top diameter and varying tapering angles (Fig. 4.8a). To compare their performance, we evaluate the power flow (Poynting vector) of the PL emission on the detector side (facing the pillar base). Specifically, we first determine the angle (θ_i) of the light incident on the diamond-air interface. We then recall that the maximum cone of light that can enter a certain NA objective is given by: NA = $n_d \sin\theta_{NA}$, where we take into account the diamond's refractive index (n_d). Finally, we sum over the power flow terms corresponding to incident angles smaller than θ_{NA}. We find that the PL in finite tapering angle pillars is guided into smaller solid angles and may yield a larger PL collection efficiency (Fig.4.8b).

So far, we have assessed the angular distribution of the PL intensity at a plane inside the diamond, which is often done to compare the performance of nanophotonic structures [101, 103]. This evaluation, however, neglects phase aberrations introduced by the travel of light inside the diamond. We now aim to include the effect of phase aberrations by implementing a second method of assessing the PL collection efficiency using a formalism from Novotny and Hecht[131]:
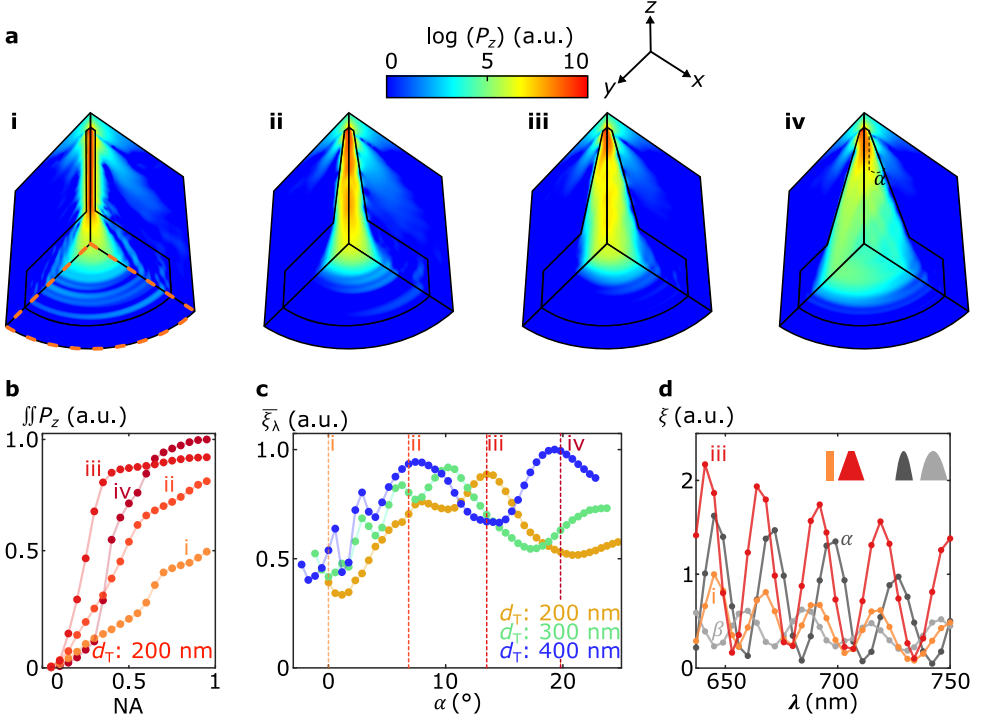
Figure 4.8: Simulating the PL emission and collection efficiency for varying NV probe shapes. The simulation geometry consists of a diamond pillar (2.5 μm length) on top of a platform (3.5 μm diameter, 1 μm thickness) and an electric dipole (pointing along x) 20 nm below the pillar apex (SI Note §4.6.7). (a) Power flow of the PL emission in the z-direction (z-component of the time-averaged Poynting vector, P_z) for varying bottom diameters d_B: (i) 200 nm, (ii) 800 nm, (iii) 1400 nm,(iv) 2000 nm and a fixed top diameter d_T: 200 nm. P_z is evaluated at 637 nm and plotted in a normalized and logarithmic scale. (i) The dashed orange outline represents the diamond-air interface at the detector side, which is the integration area used for evaluating the PL collection efficiency in b-d. (b) Integrated P_z over the area indicated in a-i as a function of incident angle $\tan\theta_i = \sqrt{P_x^2 + P_y^2}/|P_z|$. We relate the incident angle to the angle of the out-coupled light that can enter a specific NA-objective ($\sin\theta_{NA} = NA/n_d$). Here, $n_d = 2.4$ is the diamond's refractive index, and $\iint P_z(\theta_{NA}) = \int\int_0^{\theta_i \leq \theta_{NA}} dS P_z$. (c) The average collection efficiency as a function of the pillar tapering angle for top diameters: $d_T = 200, 300, 400$ nm. Here, the average collection efficiency $\overline{\xi_\lambda}$ is defined by the average $P_{pinhole}$ (SI Note 4.6.8) computed at 15 linearly spaced wavelengths between 637-750 nm, normalized to the maximum found for $d_T = 400$ nm and $\alpha = 19.3°$. (d) Collection efficiency as a function of emission wavelength for a d_T =200 nm cylindrical pillar (orange), a d_T =200 nm and d_B =1400 nm conical pillar (red) and two parabolic-shaped pillars with $f = 100$ nm (light gray) and $f = 42$ nm (dark gray) with the NV in the parabola's focal point. Here the collection efficiency is defined as $P_{pinhole}$ normalized to the maximum of orange (cylindrical pillar).

We propagate the COMSOL electric field profiles, computed at a plane inside the diamond, to the diamond-air interface. We then use Fresnel coefficients to calculate the transmitted electric field that we subsequently project onto an objective facing the pillar base and which collimates the electric field. We then define a second lens with a long focal length ($f' \gg f_{obj}$) to focus the electric field into a narrow spot. Finally, we remove all terms focused beyond a certain pinhole radius and sum over the square of the remain-

ing terms, yielding the emission power passed through the pinhole. Phase aberrations broaden the spot, thereby lowering the transmitted power. We repeat this calculation for different objective positions around its focal distance and extract the maximum pinhole power (P_{pinhole}), which we, from here on, use as a figure of merit to quantify the collection efficiency. For more details on the equations describing the electric field propagators, we refer to SI Note 4.6.8 and Ref. [131].

We now compare the average P_{pinhole}, evaluated over a range of wavelengths representing the NV spectrum, to find the optimal NV probe shape(Fig. 4.8c). Despite the wavelength averaging, all curves show non-monotonic behaviour, with minimal values around half their maximum value. This indicates that small variations in the tapering angle for a given pillar length significantly alter the collection efficiency. We find a maximum collection efficiency at a tapering angle of $\alpha \approx 19°$ and a 400 nm top diameter. At this tapering angle, the collection efficiency is twice that of a cylindrical pillar of the same top diameter. Furthermore, we find a similarly high-performing device (only ~10% lower) along the $d_{\text{T}} = 200$ nm-curve at $\alpha \approx 14°$, corresponding to a 2.3 performance enhancement compared to a cylindrical $d_{\text{T}} = 200$ nm device. Overall, Fig. 4.8c shows that the collection efficiency increases for tapering angles larger than 4-5 degrees up to a maximum increase factor of about 2-2.3. Nevertheless, it is crucial to realize precise shape control to obtain the best results due to the non-monotonic behaviour as a function of α.

Finally, we compare P_{pinhole} as a function of wavelength between four different device shapes: The high-performing conical device with $d_T = 200$ nm and $\alpha = 14°$, a same $d_T = 200$ nm cylindrical probe, and two different parabolic-shaped probes having an NV precisely positioned at their lens focal point (Fig. 4.8d). We see slight variations in the wavelength dependence between the different devices, underscoring the importance of wavelength averaging when evaluating the collection efficiency. Despite the minimal range of parabolic shapes studied here, the relatively high collection efficiency of our conical probe is interesting and indicates that conical probes provide an alternative route toward high-collection efficiency NV probes suitable for shallow NV centres.

4.4.2. FABRICATION OF CONICAL DIAMOND NANOPILLARS.

To realize large tapering angle nanopillars for high collection efficiency NV probes, we explore an alternative masking method for etching diamond nanopillars here. To do so, we largely follow Ref. [102] and use cylindrical masks of positive e-beam resist (Fig. 4.9a-i) that, when heated above the resist's glass transition temperature, reflow into parabolic shapes with smooth sidewalls (Fig. 4.9a-ii)[132–134]. Next, the resist pattern is transferred into a Si_3N_4 film to create a mask with a selectivity to etch diamond of about $s \approx 35$[viii] (Fig. 4.9a-iii). Unlike Ref. [102], however, that uses ≈ 100 nm deep NV centres, we do not transfer the full parabolic shape into the diamond, but we stop etching once the probe reaches a top diameter of about 200-400 nm (Fig. 4.9a-iv)). This ensures that the top part of the Si_3N_4 mask still protects the NV centres that are shallowly implanted below the diamond surface.

[viii]We find that the selectivity of the Si_3N_4 film is higher for larger mask areas, e.g., for 10x10 μm^2 Si_3N_4 masks, we obtain a selectivity of roughly $s \approx 100$.
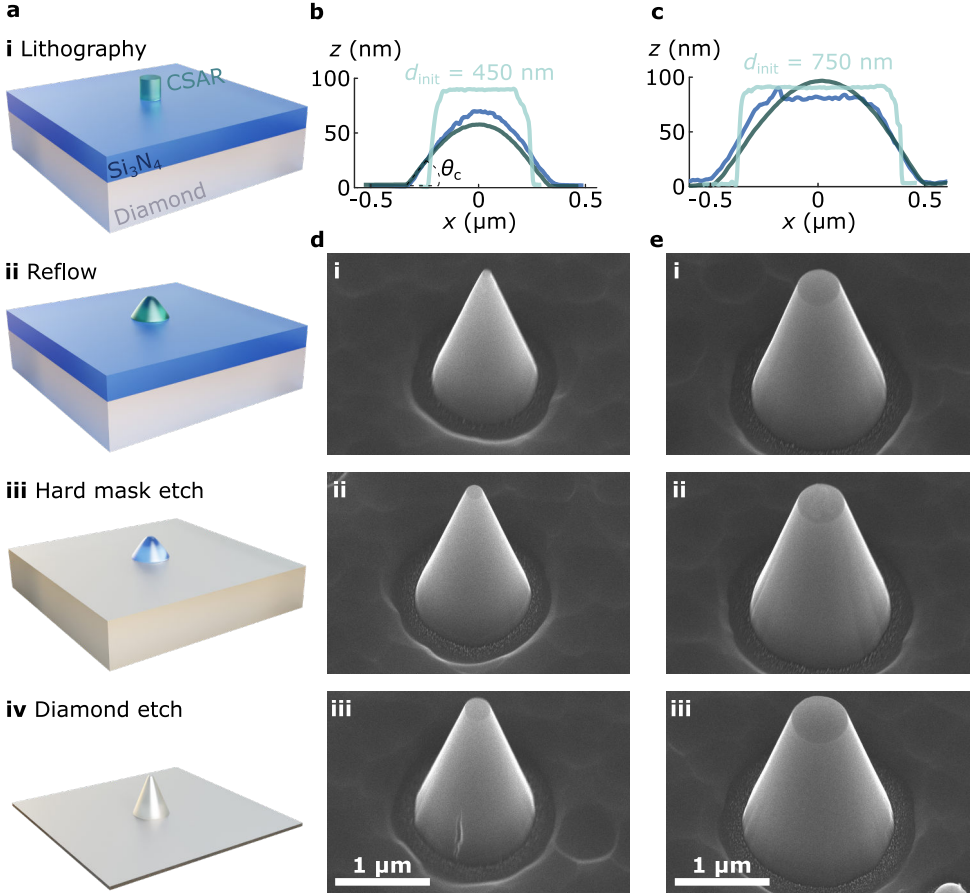
Figure 4.9: Creating conical diamond nanopillars using parabolic etch masks. (a) Illustration of the fabrication scheme (for details, see table 4.3): (i) We lithographically define cylindrical masks using CSAR e-beam resist. (ii) Resist reflow by baking on hotplate (175 °C). (iii) Resist transfer into Si_3N_4 film using RIE. (iv) Mask transfer into diamond using ICP-RIE. (b)-(c) AFM (*Bruker*) height profiles of the etch mask at different stages in the process using a dose of $350\,\mu C\,cm^{-2}$ and an initial mask diameter of $d_{init} = 450\,nm$ (b) and $d_{init} = 750\,nm$ (c): After developing (light green), after resist reflow (dark green), after transfer into the Si_3N_4 film (dark blue). After the reflow, the resist assumes a contact angle of $\theta_c \approx 13°$ with the Si_3N_4/diamond surface. (d)-(e) SEM images of the diamond nanopillars after the diamond etch for varying doses, yielding diamond nanopillars with different top/bottom d_T/d_B diameters with a final length of $\sim 2.2\,\mu m$. Images taken at a sample tilt of 30°. (d) Using $d_{init} = 450\,nm$, we obtain $\approx$: (i) $450\,\mu C\,cm^{-2}$: 80/1100 nm/nm. (ii) $350\,\mu C\,cm^{-2}$: 180/1220 nm/nm. (iii) $250\,\mu C\,cm^{-2}$: 280/1280 nm/nm.(e) Using $d_{init} = 750\,nm$, we obtain $\approx$: (i) $450\,\mu C\,cm^{-2}$: 430/1420 nm/nm. (ii) $350\,\mu C\,cm^{-2}$: 500/1490 nm/nm. (iii) $250\,\mu C\,cm^{-2}$: 600/1600 nm/nm.

Scanning electron microscope (SEM) images show that our new protocol yields conical probes with smooth sidewalls and tapering angles of about 12-13° for probe lengths of 2.2 μm and varying top diameters (Fig.4.9d-e) (for details, see table 4.3). Such tapering angles are about 2-3 times higher than the 4-5° angle we obtained using an HSQ resist

mask (Fig.4.5), thereby enhancing their expected collection efficiency. We will now discuss the additional advantages of this new method compared to our previous protocol.

First, we find that the CSAR resist (Step 2, table 4.3) does not degrade over several weeks, obtaining reproducible results over many iterations, in contrast to HSQ-resist.

Second, an O_2 plasma is sufficient to generate smooth etch profiles due to the smooth resist profile created during the reflow process (recipe # 3, table 4.1). We note that the cyclic etch recipe used before (§4.3.1) might still be useful to enhance mask erosion and increase the tapering angle further(as in Refs. [103, 135]).

1.	**Si_3N_4 dep.**	Si_3N_4 deposition: 2 min 12 s at 100 °C (ICP-CVD) (~100 nm)
2.	**Spincoating**	AR-P 6200.04 (CSAR) (positive *e*-beam resist): 4000 rpm (~100 nm), bake 3 min at 150 °C.
3.	**Spincoating**	Elektra92 (conductive layer): 1000 rpm, bake 1 min at 90 °C.
4.	***e*-beam**	Exposure pillar pattern, i.e. inverted circles with diameters from 400-750 nm: ~400 μC cm^{-2} dose, ~32 nm spotsize, ~ 59 nA beam current.
5.	**Develop**	Immerse sample: -1 min in water (to remove Elektra92), -1 min in pentyl acetate, -1 min in MIBK:IPA (1:1), -1 min in IPA. Blow dry.
6.	**Reflow**	Bake at hotplate: 10 min at 175 °C.
7.	**Hard mask etch**	Transfer resist mask into the Si_3N_4 film using plasma #6, table 4.4: For 9 min (~225 nm; $s \approx 1$).
8.	**Diamond etch**	Transfer pillar mask into diamond, using plasma #3, table 4.1: For 15 min (~3 μm; $s \approx 35$).

Table 4.3: Step-by-step protocol with recipe parameters for fabricating conical diamond probes using a Si_3N_4 mask and resist reflow. Prior to step 1, we clean the diamond in fuming nitric acid (4.6.1). In steps 2-3, we choose the same thickness for the resist, and the Si_3N_4 film because the selectivity of CSAR in the Si_3N_4 etch in step 7 is approximately 1. Note that for the sample shown in Fig. 4.9, we deposited a 5 nm layer of titanium before spincoating resist (step 2) to promote the resist adhesion, requiring its subsequent removal prior to transferring the pattern into the Si_3N_4 film (step 7) using plasma recipe #7, table 4.4 for 10 s. Additionally, we used for this sample plasma enhanced CVD (PECVD) Si_3N_4 deposition (8 min at 300 °C; PlasmaPro80+, *Oxford Instruments*). We left these steps out of the current protocol since we found the titanium to be unnecessary and obtained the same results using a low-temperature SiN deposition, using inductively coupled plasma CVD (ICP-CVD; PlasmaPro 100, *Oxford Instruments*). Low-temperature deposition is more convenient because it allows glueing of the diamond to a carrier before deposition. For *e*-beam lithography (step 4), we use a RAITH 5200 EBPG system at 100 keV accelerating voltage.

Third, we can vary the probe length, provided we carefully tune the mask thickness and diameter (d_{init}). Namely, during the reflow, the resist reshapes from a cylinder to a parabola while finding a balance between its surface area exposed to air and the Si_3N_4-diamond interface. Here, we find that the resist assumes a fixed contact angle (θ_c) of about ≈14° (Fig.4.9b-c). As such, depending on the mask's original volume (given by its initial diameter (d_{init}) and thickness), its maximum thickness after reflow will either shrink (Fig.4.9b, dark green) or increase (Fig.4.9c, dark green). For creating longer pil-

lars, a thicker Si_3N_4 mask is required to withstand the longer duration O_2 plasma, and consequently, the resist thickness and diameter (d_{init}) must be increased too.

Finally, patterning of Si_3N_4 films to fabricate high-end photonic waveguides is performed by numerous groups, including some in our department, [136–138], making the patterning methods and etch recipes readily available and well-characterized. In addition, it complements other work in our group on diamond photonic cavities [118].

| Gasses	F (sccm)	P_{RF} (W)	P (μbar)	R (nm/min)
6. CHF$_3$/O$_2$	50/2.5	50	10	24-25
7. SF6$_6$/He	12.5/10	40	10	15

Table 4.4: Recipe parameters for reactive ion etching of titanium and silicon nitride in Plasma System SI 200 (*SENTECH*). *F* is the gas flow rate, P_{RF} is the power, *P* is the operating pressure and *R* is an indication of the etch rate.

4.4.3. Integrating conical pillars into the NV probes protocol

To implement conical pillars into the NV probe fabrication, we now slightly adjust the initial protocol (§4.3). As before, the NV probe fabrication protocol relies on three main etch steps: step I defines the probe's platform, in step II, we define the pillar, and finally, in step III, the platforms are released from the bulk diamond. One essential difference is the reuse of the same mask for step I and II. This ensures that the platform sidewalls are free from Si_3N_4 that is otherwise difficult to remove when etching the pillars. Moreover, it reduces the number of deposition steps. Step III has remained unchanged from the original protocol (§4.3.3). A more detailed description of the protocol is provided in table 4.5.

Using the protocol described in table 4.5, we successfully fabricated a diamond with a total of 13x5x6= 390 NV probes (Fig.4.10a-b)[ix]. Because we also used resist reflow for the platform etch mask, the diamond platforms have rounded and smooth edges with little roughness that can impede reaching NV-sample proximity (Fig. 4.10c). The probes have a length of 3 μm (Fig. 4.10d), which is twice the length of the probes fabricated using our initial protocol. Surprisingly, the pillars have a semi-conical shape (unlike in §4.4.2), where the first ~1 μm is cylindrical, and the final ~2 μm is conical with a tapering angle between 13-15°, depending on the top diameter. The cylindrical part of the pillar is likely a result of the thicker resist used here, of which the high-curvature part was not fully transferred into the Si_3N_4 film. Finally, because we varied the initial resist mask diameters (d_{init}), we realize pillars with varying top diameters ranging from 100 to 700 nm.

[ix]Not all of the devices are released from the bulk, due to the spatially inhomogeneous etch rate during etch step III

4
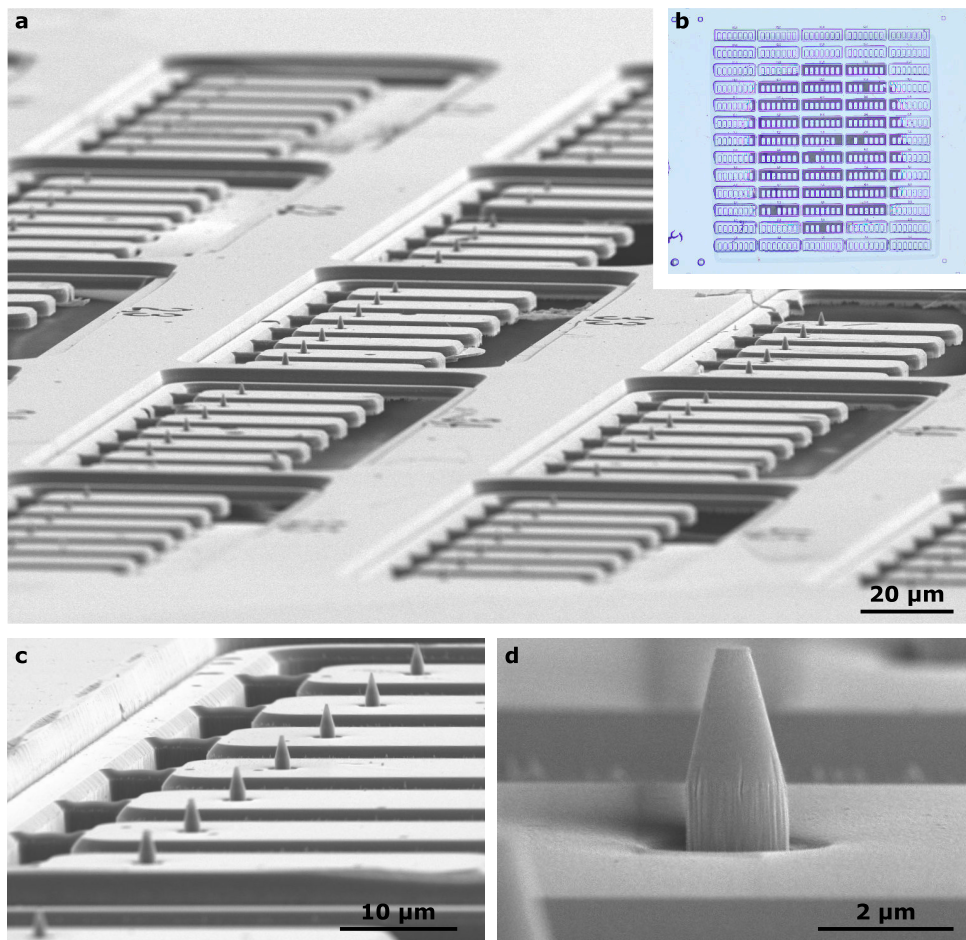
Figure 4.10: Diamond after final etch step with conical probes. (a) Scanning electron microscope (SEM) overview image of several scanning probe devices that are released from the bulk (a 2x2x0.05 mm^3) diamond. Each 6x1 cell of devices is labelled with an identifier for ease of recognition in the confocal microscope. Taken at an angle of about 85° to the sample normal. (b) Optical image of diamond, taken immediately after final cleaning step (i.e., without the glue residues observed in (a)) showing all 13x5x6= 390 devices. During the backside etch, the etch rate is fastest in the centre of the diamond. As such, the centre devices are released first. Distance between the rectangular markers on the outer corners is 1700 μm. (c) Close-up of several devices. Within a 6x1 cell, we used masks with different diameters resulting in pillars with varying top diameters. The platforms have round edges, a combined result of the reflowed resist and the low selectivity of the silicon nitride mask in the O$_2$ diamond etch. (d) Close-up of one of the pillars with length ≈3.0 μm. The first 2 μm from the top the pillar is tapered with a top diameter of 460 nm going to a bottom diameter of 1.5 μm yielding a tapering angle of about 14.5°. Then, for the final ~ 1.0 μm, the tapering angle is almost zero.

4

		Preparation
1.	**Determine t_{init}**	Measure the initial diamond thickness (SI Note 4.6.4).
2.	**Cleaning**	To remove particles or organic material on NV-surface clean in HNO$_3$ 100% for 10 min(SI Note 4.6.1).
3.	**Glue to carrier**	See SI Note 4.6.3
4.	**Prepare dep.**	Overnight cool down of ICP-CVD from 300 °C (typical operating temperature) to 100 °C (~6 h).
		Etch step I
5.	**Si$_3$N$_4$ dep.**	ICP-CVD deposition: 4 min 24 s at 100 °C (~ 200 nm)
6.	**Spincoating**	AR-P 6200.13: 4000 rpm (~400 nm), bake 3 min at 150 °C.
7.	**Spincoating**	Elektra92 (conductive layer): 1000 rpm, bake 1 min at 90 °C.
8.	**e-beam**	Exposure platform pattern: ~400 µC cm^{-2} dose, ~32 nm spotsize, ~ 59 nA beam current.
9.	**Develop**	Immerse sample: 1) 1 min in water (to remove Elektra92), 2) 1 min in pentyl acetate, 3) 1 min in MIBK:IPA (1:1), 4) 1 min in IPA. Blow dry.
10.	**Reflow**	Bake at hotplate: 10 min at 175 °C.
11.	**Si$_3$N$_4$ etch**	Transfer platform pattern into SiN hard mask: plasma #4, table 4.4: 9 min (~ 225 nm)
12.	**Diamond etch**	Transfer platforms into diamond: plasma #3, table 4.1: 15 min (~ 3 µm)
		Etch step II
13.	**Spincoating**	See step 6 and 7.
14.	**e-beam**	Exposure pillar pattern: ~400 µC cm^{-2} dose, ~32 nm spotsize, ~ 59 nA beam current.
15.	**Develop**	See step 9.
16.	**Reflow**	See step 10.
17.	**Si$_3$N$_4$ etch**	Transfer pillar pattern into remaining SiN (~140 nm): plasma #4, table 4.4: 11 min (~ 264 nm)
18.	**Diamond etch**	Transfer pillars into diamond: plasma #3, table 4.1: 15 min (~ 3 µm)
		Etch step III (for details, see §4.3.3)
19.	**Protect NV side**	Protect pillars by depositing 50 nm of titanium.
20.	**Glue to quartz carrier**	Remove diamond from Si-carrier. Flip and clean its backside (not NV side). Glue to quartz carrier with pillars facing down and place the quartz mask for the deep etch.
21.	**Diamond etch**	Release NV probes by etching remaining diamond from the backside.
22.	**Cleaning**	Removal of masking material (using HF) and organic resist residues (using HNO$_3$) (SI Note 4.6.1).

Table 4.5: Step-by-step protocol with recipe parameters for fabricating diamond scanning probes. We start with a clean diamond with shallow NV centres (for prep. details, see §4.2.1). We deposit a 200 nm Si$_3$N$_4$ film (step 4-5). We find that a layer of ≈140 nm remains after etching the platforms, yielding a mask etch rate of approximately $r ≈ 4$ nm/min (step 12). Note, the remaining mask on the platforms is now slightly thicker than the ≈90-100 nm mask used for the conical pillars in §4.4.2, which allows us to slightly increase the etch duration and create longer probes (step 21). Conveniently, we can keep track of the Si$_3$N$_4$ film thickness throughout the process by monitoring its colour onto the silicon carrier piece. For e-beam lithography (step 8 & 14), we use a RAITH 5200 EBPG system at 100 keV accelerating voltage.

4.4.4. OPTICAL CHARACTERIZATION OF SEMI-CONICAL NV PROBES

We now present a preliminary study of the optical properties of our new NV probes. First, we study the expected collection efficiency for semi-conical probes, resembling the device shapes fabricated above (Fig. 4.11a-b). Here, we find a maximum performing device with $d_T = 400$ nm and $\alpha \approx 19.5°$. For devices with $d_T = 200$ nm, a tapering angle of 14° leads to a similarly high collection efficiency and provides a more than 2.5 enhancement compared to a cylindrical device with the same small d_T. Since a tapering angle of $\alpha = 14°$ corresponds well to what we experimentally realize in Fig. 4.10, we, therefore, expect an improved collection efficiency for our new NV probe shapes.
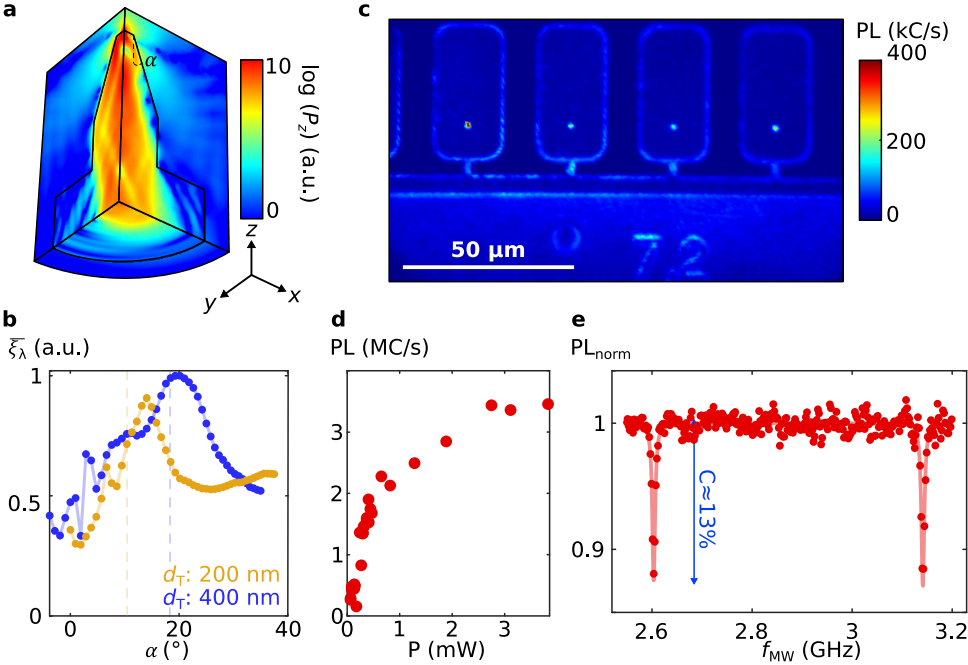
Figure 4.11: Optical properties of new generation NV probes. (a) Emission pattern of an s-dipole (pointing along x) in a semi-conical NV probe (for details see SI §4.6.7) with a conical top with $d_T = 400$ nm, $d_B = 1500$ nm and $L = 1.5$ µm and a cylindrical end with $L_{cyl} = 1$ µm-long, corresponding to the device with maximum collection efficiency in b. (b) Collection efficiency as a function of tapering angle for a top diameter of 200 and 400 nm. The collection efficiency is defined here as the average $P_{pinhole}$ (§4.6.7), evaluated over 15 linearly spaced wavelengths between 637 and 750 nm, representing the NV spectrum. Values are normalized to the maximum found at $d_T = 400$ nm and $\alpha = 19.3°$. (c) Spatial PL map ($\lambda > 600$ nm) of four released devices of the sample also shown in (Fig. 4.10) using 36 µW laser power (at 532 nm). (d) PL as a function of optical power while focusing on one of the pillars. The optical power is adjusted by optical density filters. (e) Electron spin resonance (ESR) measurement. Solid line represents a double Lorentzian fit from which we obtain an ESR contrast of 13% for both peaks and a magnetic field of $B_\parallel \sim 10$ mT (532 nm). For details on the characterization setup, see Ref. [139].

Using a confocal microscope, we now characterize the PL from the fabricated devices shown in Fig. 4.10 (for setup details, see Ref.[139]). Recall that this sample was implanted with shallow NVs with an expected density of ~1 NV/probe (Table 4.2) before structuring

the diamond into NV probes. A spatial PL map shows four released devices of which the pillars light up from a dark background with PL rates reaching up to $\approx 400\,\mathrm{kC\,s^{-1}}$ suggesting the presence of NV centres (Fig. 4.11b). Targeting one single device, we find that the PL emission from a high-intensity pillar can saturate to more than $3\,\mathrm{MC/s}$ (Fig. 4.11c), similar to the saturation rates observed in state-of-the-art devices from Refs. [102, 103]. We then confirm the presence of an NV centre by performing an electron spin resonance (ESR) measurement with a small magnetic field aligned along one of the NV orientations, causing the ESR frequencies to split. For a device with an NV centre that aligns with the field, we measure two distinct ESR resonances with an ESR contrast of $\approx 13\%$ (Fig. 4.11d). Note that although we do not observe additional resonances, we can not exclude the presence of another NV with the same orientation, contributing to the observed high PL rate and ESR contrast. This confirmation would require additional characterization, e.g., using a photon correlation $g^2(\tau)$ measurement[111, 140].

4

Finally, we extend our optical inspection to the other devices. Disappointingly, our preliminary results show that only ~16% of the fabricated devices host an NV centre that produces ESR contrast. This yield is lower than expected considering our implantation dose (aiming for an average of 1-2 NVs per device) and previous works using similar doses[103, 111, 117]. Additionally, if we consider that some of these devices contain more than one NV or one with poor spin-optical properties, the actual yield of useful devices is even lower. However, we also observe this low NV density in other fabricated diamond samples with shallow NV centres. Therefore, as we also previously found out that our triacid procedure is not able to remove thicker graphite layers (SI Note 4.6.1)[125], we suspect that our current diamond surface treatment is insufficient, leaving impurities that quench shallow NV centres and cause the low yield.

4.5. Conclusions

The purpose of this chapter was twofold: First, we described the fabrication of our first generation of scanning NV probes. In chapter 5, we use this first generation of scanning NV probes for the magnetic imaging of spin waves. Second, we developed a new protocol for fabricating NV probes with an optimized, highly tapered pillar shape for a higher PL collection efficiency and magnetic field sensitivity. In addition, we reduce the protocol's complexity by excluding the use of HSQ resist and using standard oxygen-based diamond etch recipes. Although creating high-quality shallow NV centres is still a work in progress and limits our device yield, a first optical inspection shows that some devices demonstrate auspicious optical properties, such as a high PL rate and ESR contrast. Finally, we anticipate that optimizing the NV environment further by improving diamond surface treatments, such as cleaning recipes and polishing techniques, will enhance our device performance[112, 113]. Ultimately, the deterministic fabrication around NV centres based on their spin-optical properties will scale up the device yield and enable optimally utilizing the waveguiding abilities of our diamond nanopillars[102].

ACKNOWLEDGMENTS

4

4.6. SUPPORTING INFORMATION

4.6.1. CLEANING PROCEDURES OF DIAMOND SURFACE

Fuming nitric acid: To remove organic residues and particles, we immerse the diamond in fuming nitric acid (100% HNO_3) for ~10 min. Subsequently, the diamond is thoroughly rinsed in water. To prevent drying marks, we move the sample to a wetbench suitable for organic solutions and immerse it in isopropanol (IPA) prior to blow drying the sample.

Hydrofluoric acid: To remove silicon nitride, titanium and/or HSQ-resist from our diamond samples, we immerse the diamond in hydrofluoric acid (40% HF) for ~10 min. Finally, we repeat the rinsing procedure using water and IPA as described above.

Boiling triacid: To remove graphite and other surface contaminants before and after annealing, we clean the diamonds using a triacid solution, which is a mixture of sulfuric acid (95-98% H_2SO_4), nitric acid (65% HNO_3), and perchloric acid (60% $HClO_4$) with a 1:1:1 ratio, which we heat to a temperature of 120 °C for about ~1 h. In addition, we use a reflux system to prevent the perchloric acid to form salts, which react explosively with organic materials such as acetone and isopropanol [125]. Note, since 120 °C is near the maximum rated temperature of the glassware used during this work, we could not further increase the temperature to realize more aggressive boiling. We are currently testing the triacid procedure at higher temperatures using a new setup to improve the cleaning process and the quality of our shallow NV centres.

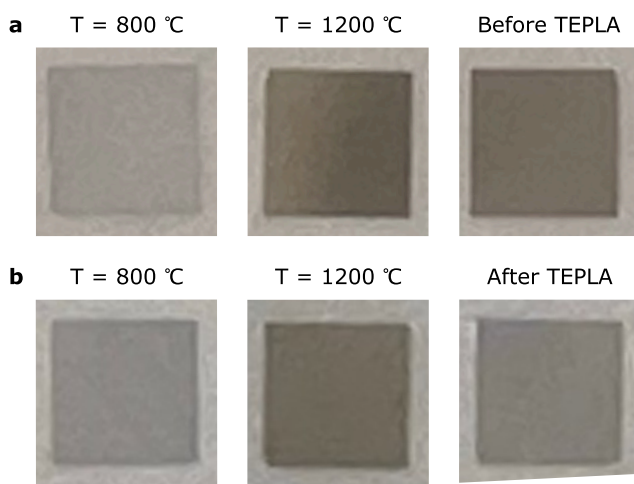#### GRAPHITIZATION OF DIAMOND SURFACE AFTER ANNEALING

One time, our diamond samples came out of the annealing oven with dark surfaces, indicating an increase in graphite formation that we could not remove via our triacid procedure (Fig. 4.12a). This increase was most likely caused by the degradation of one of the o-rings sealing the system, causing an unstable pressure and subsequent burning of the diamond surface.

From this observation, we could conclude, however, that our triacid cleaning procedure (with maximum solution temperatures of 120 °C) is not sufficient to remove thicker layers of graphitized diamond. Later, we learned from literature that this is most likely because efficient oxidation from perchlorate requires temperatures of at least 150 °C[125]. Such a remaining layer of graphite can generate an environment of charge noise that may quench our shallow NV centres [112].

Instead, we found that using an isotropic oxygen plasma removed most of the graphite without etching away[x] our shallow NV centres. Nevertheless, more investigation is required to confirm that the shallow NV centres are unaffected and to determine the maximum etch time.

a   T = 800 °C   T = 1200 °C   Before TEPLA

b   T = 800 °C   T = 1200 °C   After TEPLA

Figure 4.12: Graphitization of diamond after long and high-temperature annealing sequence (a) From left to right: Diamond that was annealed up to 800 °C/ 1200 °C/ 1200 °C. All samples have undergone triacid cleaning at 120 °C for one hour after annealing. (b) Removal of graphite of right diamond using 600 SCCM O_2 600 W for 10 min and 30 s on both sides inside a Faraday cage (Tepla). Images taken with an iPhone (i.e. the environment light is not constant between a-b). Diamonds are 2x2 mm^2.

4.6.2. Surface topography after polishing and etch step 0

Below (Fig. 4.13), we include a topography characterization of one of our diamonds polished (in 2019 *by Almax Easylab*) and etched according to §4.2.1, yielding the following surface roughness parameters: A roughness average (R_a) of 0.08 nm and an average maximum height of the roughness (R_z ISO) of 0.47 nm.

---

[x]Preliminary PL scans show no reduction in the number of NVs
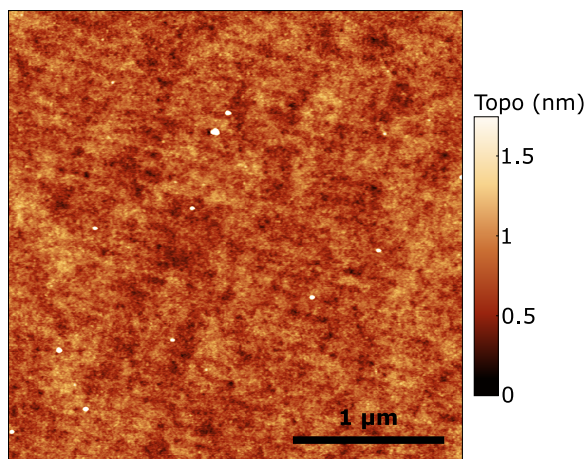
Figure 4.13: Diamond surface roughness characterization using atomic force microscopy (AFM, *Asylum Cypher*). A 3x3 μm² scan to determine the surface roughness of a diamond that was first polished (*Almax Easylab*, 2019) and later etched as described in §4.2.1. An external noise source was present during scanning causing the diagonal lines, which we exclude from the characterization by only considering line profiles that run parallel to the vibration lines. Additionally, the surface contains several dirt particles (white), which we also exclude. We obtain a roughness average (R_a) of 0.08 nm and an average maximum height of the roughness (R_z ISO) of 0.47 nm.

4.6.3. GLUE DIAMOND TO A CARRIER PIECE

To enable spincoating on a small sample like our 2x2 mm² diamond and for ease of handling, we glue our diamond sample onto a ~1x1 cm² piece of silicon. To do so, we put a tiny droplet of low-viscosity PMMA (950K, A3) resist onto the silicon carrier piece and carefully place (using sharp metal tweezers: TL SS-SA-SL, *LINDSTRÖM*) our diamond on top while ensuring the correct side is facing up. Additionally, we try to ensure that the diamond is not tilted by using as little glue as possible. We bake the sample for 1 min at 175 °C to cure the resist.

Some shortcomings of this method are that even when using sharp tweezers, it can be challenging to realize a steady grip on the diamond due to the small and especially thin sample sizes. As a result, the diamond might fall or jump away, creating another opportunity to collect dirt on its surface. For that reason, we reduce the number of times we pick up the diamond. In case we do have to move the diamond, other methods could be more reliable depending on the situation:

For samples for which it is important to maintain a clean top surface, one could use a thin tissue (cleanroom grade) and try pushing it underneath the diamond and subsequently transfer the diamond together with the tissue without having to touch the diamond with tweezers (that often introduce contamination). A downside of this approach is that the final position of the diamond is more difficult to control. Alternatively, we sometimes use a vacuum tweezer (*Loenen Instruments*) to pick up the diamond. Here, however, it is required to have a large enough free surface area, and at the same time, the

tweezer's nozzle might introduce extra dirt.

Another tricky part of our glueing method is that the glue (PMMA) dissolves in most organic solvents, such as acetone and anisole, and could, therefore, dissolve in a subsequent spincoating step when using anisole-based resists, such as CSAR and PMMA. Therefore it is important to carefully cure the resist (by baking long enough) before spincoating and only use tiny droplets that do not spread out over the bare carrier or diamond. On the other hand, this high dissolvability also presents the biggest advantage of using PMMA over other types of glue, ensuring that the diamond can be easily cleaned afterwards.

4.6.4. Diamond thickness determination

To prevent thinning down the diamond too much during etch step III, it is essential to determine the initial diamond thickness with 1-2 μm accuracy across the entire surface. We do so, by evaluating the intensity peaks in the confocal signal of a microscope that is available in our cleanroom, i.e., the WAFERinspect (*Confovis measuring systems*). This microscope uses LED light and a structured illumination method allowing us to conveniently determine the diamond thickness across the field of view of the microscope objective (areas of about 350 μm^2) (Fig.4.14a).
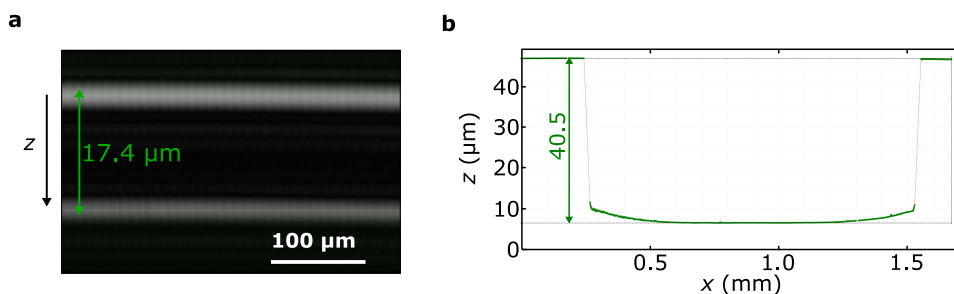
Figure 4.14: Determing the total diamond thickness before nanofabrication and the etched thickness after performing etch step III. (a) Diamond thickness evaluation. The vertical axis represents the position of the microscope's objective (*z*). The horizontal axis, described by the white scale bar, represents a spatial line (~ 350 μm) parallel to the sample plane. Intensity peaks from top to bottom represent the reflection from the top surface (highest intensity), and subsequently, reflection from the bottom surface and their distance (17.4 μm, green arrow) determines the diamond thickness across the line trace. A factor of 2.4 must be used to take into account the refractive index of diamond. After defining the initial thickness, we know how much we must thin down the diamond's backside to release the platforms in etch step III. (b) A line trace of the reflection signal after having etched the diamond backside by 40.5 μm.

4.6.5. In-situ monitoring of the etch rate during etch step III

We can monitor the etch progress in situ via a laser interferometer system. Since the field of view and laser positioning resolution of this system is limited (Fig. 4.15a), it can only be used when etching large surface areas, such as the 1.2x1.2 mm area window in the quartz mask used during etch step III. During the etch, the intensity of the reflected laser light oscillates with a frequency that depends on the etch rate (Fig. 4.15b), and the number of oscillations determine the total thickness change (Fig. 4.15c). Although in-

situ monitoring of the etch rate allows for careful determination of the etched thickness, we remain careful and stop the process $\sim 3-8\,\mu m$ early (depending on the uncertainty in initial diamond thickness and stability of the etch rate) for optical inspection and to prevent from thinning down the diamond too much (Fig. 4.15d-e).
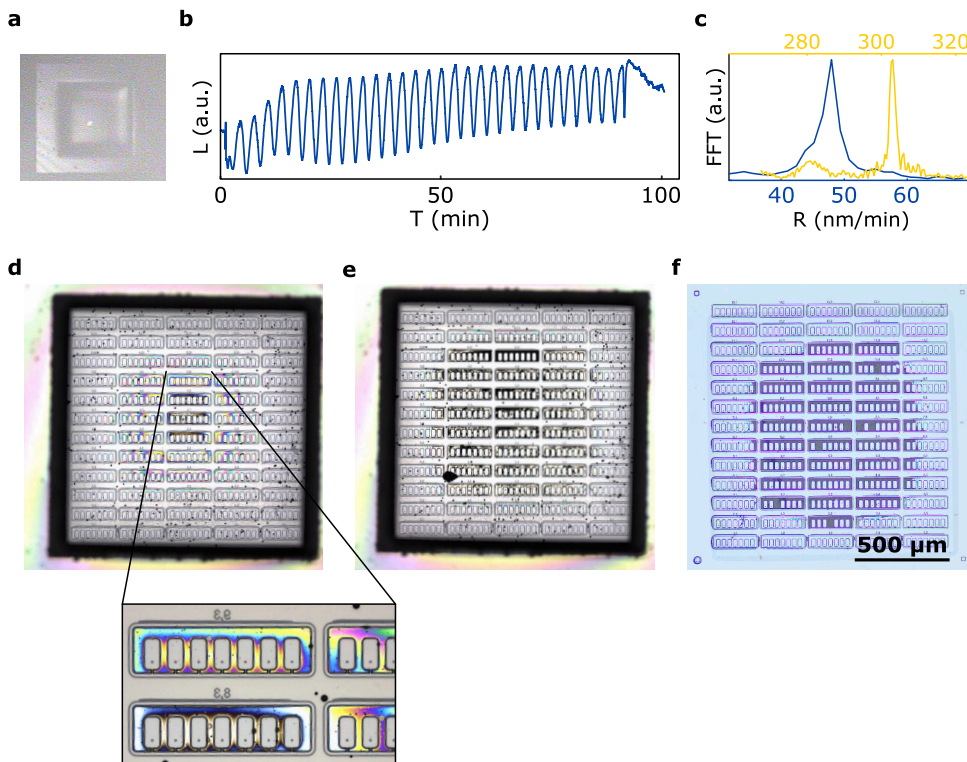
Figure 4.15: In-situ monitoring of the etch rate. (a) Camera field of view of the etcher's interferometer system with the laser spot reflecting from the centre of the exposed area. Here a quartz mask with a center window of $\sim 1.2\text{x}1.2\,\text{mm}^2$ is covering the outer edges of the $2\text{x}2\,\text{mm}^2$ diamond. The diamond's NV side is facing down. (b) Laser Intensity during the Ar/Cl etch (#1, table 4.1) periodically varies depending on the etch rate. Each period corresponds to a difference in thickness of $\approx \lambda/(2n_d) = 138\,\text{nm}$, where λ is the laser wavelength (672 nm). Fourier transforms of the trace in (b) (blue) and of a similar trace during an O_2 etch (yellow) (#2, table 4.1) finding an average etch rate of 48 nm/min and 303 nm/min respectively. (d) The diamond after 97 min of O_2 etching (#3, table 4.1). Some of the centre devices are (about to be) released. (e) After etching another $\approx 1\,\mu m$ more devices have been released. We stop etching from this point. (f) Diamond sample after removing the titanium protection layer on the NV-side using HF (40%) and cleaning in HNO_3 (100%) (SI Note 4.6.1).

4.6.6. Mount NV probe to tuning fork via a optical fiber

Below, we provide a step-by-step protocol for glueing a single diamond probe device to a tuning fork:

1. Fibre pulling: We use a pulled optical fibre as the connection between the mm-sized tuning fork (TF) and the μm-sized NV probe.

2. Glue fibre to TF: We mount the TF at an angle of 45° w.r.t. the fibre and ensure (using micromanipulators) that the vertical distance from the fibre end to the TF does not exceed the objective working distance (h_{TF} in Fig. 4.6a). We use a small droplet of UV-glue (NOA81, *Norland*), which we apply using another fibre. The glue is cured in UV light (CS20K2, *Thorlabs*). We remove the rest of the fibre using a ruby fibre scribe (S90R, *Thorlabs*) as close as possible to its connection point to the TF.

3. Glue NV probe to fibre: We mount the TF-with-fibre in a micromanipulator stage. Next, we carefully immerse the end (5-10 μm) of the fibre in UV-glue (high viscosity NEA 123, *Norland*). We then move the fibre end to a target device. At close proximity, the glue can flow onto the device platform. Use little glue such that it does not spread out too much and cover the pillar base. The UV glue is cured using UV light. Finally, we break the device out of the bulk diamond by gently moving the stage carrying the TF-with-fibre-with-NV probe away from the bulk diamond.

Step 2 is performed using a standard stereo microscope (*Olympus*) with max. 6 X magnification and a 3-axis micromanipulator stage (PT3/M, *Thorlabs*). Step 3 is performed in a probe station with a long-working distance objective with max. 20 X magnification. The probe station allows for independently moving the diamond sample and the TF-with-fibre with respect to each other via several micromanipulator stages.

4.6.7. SIMULATION SETUP

For our simulations, we use a finite element simulator (*COMSOL MultiPhysics*) in which we define the geometry of the diamond ($n \approx 2.4$) probe device consisting of a conical pillar on top of its platform surrounded by a cylindrical box of air ($n \approx 1$) (Fig. 4.16). The NV is simulated by a point located at a depth h below the pillar apex of radius r_T.
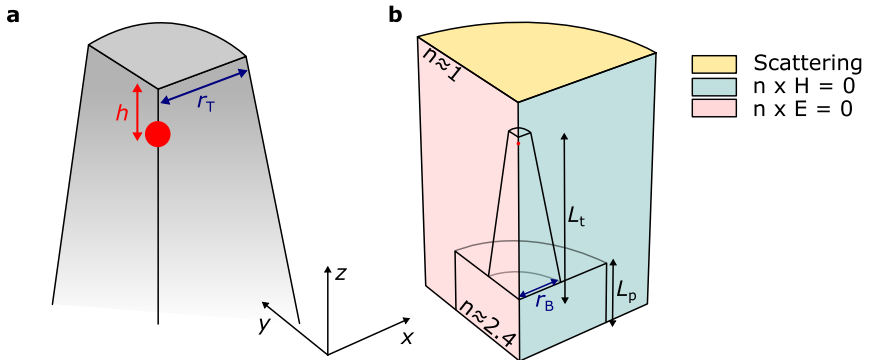
Figure 4.16: Simulation setup for COMSOL. (a) Close-up of the diamond pillar with a top radius r_T and a dipole located at a depth of h below the pillar apex. (b) Full geometry consisting of the diamond (i.e. $n \approx 2.4$) scanning probe with a conical pillar on top of 1.75 μm-radius cylindrical platform. The device is surrounded by a cylindrical box of air (i.e. $n \approx 1$; radius 2.3 μm, length 4 μm). The diamond pillar length (L_t) is fixed at 2.5 μm, the platform thickness (L_p) at 1 μm and the platform radius at 1.5 μm. The outer boundaries of the simulation setup are chosen to be transparent, i.e. scattering boundary conditions. Moreover, we reduce the computation time by only simulating one-quarter of the full device.

The outer boundaries of the geometry are set to transparent. Due to the geometry's symmetry, we can reduce the computation time by only simulating one-quarter of the device. After cutting the geometry in four, we must carefully choose the inner boundary conditions that depend on the dipole direction. For the s-dipole $n = (1,0,0)$, the inner boundary that is in the xz-plane is set to a perfect magnetic conductor (transparent for B-fields, with no tangential component along the boundary), and the other inner-boundary plane (zy-plane) is set to a perfect electric conductor. Both inner boundary planes are chosen as perfect magnetic conductors when simulating the p-dipole, pointing along z. Note these boundary conditions only hold when the NV is positioned precisely at the centre of the pillar apex.

4.6.8. Computing the collection efficiency

The collection efficiency determines the amount of light we can collect from the NV in a nanophotonic structure like our diamond nanopillar. Below we describe how we can determine how much light we can detect with our collection optics if we have calculated the field at a plane inside the diamond, following the formalism from Notovny and Hecht [131].

Using COMSOL, we numerically calculated the 2D electric field $\vec{E}_i(x, y, z = 0)$ (Fig. 4.17b) from which we compute the associated 2D spatial Fourier transform denoted by $\vec{E}_i(\vec{k}, z = 0)$. The subscript i refers to inside the diamond.

To account for light that remains trapped inside the diamond waveguide due to total internal reflection, we set $\vec{E}_i(|\vec{k}| > k_2, z = 0) = 0$, where $k_2 = k_1 \frac{\sin\theta_1}{\sin\theta_2}$ (Fig. 4.17c).

We then propagate the field to the diamond surface ($z = \delta$) (but still inside the diamond) by multiplying with the propagator:

$$\vec{E}_i(\vec{k}, z = \delta) = \vec{E}_i(\vec{k}, 0) e^{ik_1 \cos\theta_1 \delta} \tag{4.1}$$

At the diamond-air interface, part of the light is transmitted, as described by the Fresnel transmission coefficients:

$$t_s = \frac{2n_{z1}}{n_{z1} + n_{z2}} \tag{4.2}$$

$$t_p = \frac{2n_{z1}}{n_2 \cos\theta_1 + n_1 \cos\theta_2} \tag{4.3}$$

$$\tag{4.4}$$

where we used that: $\cos\theta_2 = \sqrt{1 - n_1^2/n_2^2(1 - \cos^2\theta_1)}$, $n_{z1} = n_1 \cos\theta_1$ and $n_{z2} = n_2 \cos\theta_2$. The field outside the diamond at the interface can now be written as:

$$\vec{E}_t(\vec{k}, \delta) = t_p \left(\vec{E}_i(\vec{k}, \delta) \cdot \hat{\theta}_1 \right) \hat{\theta}_2 + t_s \left(\vec{E}_i(\vec{k}, \delta) \cdot \hat{\phi} \right) \hat{\phi} \tag{4.5}$$

where the subscript t denotes that the field is evaluated outside the diamond. Here, we decomposed the field into the s-(which is the $\hat{\phi}$) and p-(which is the $\hat{\theta}_1$) components.
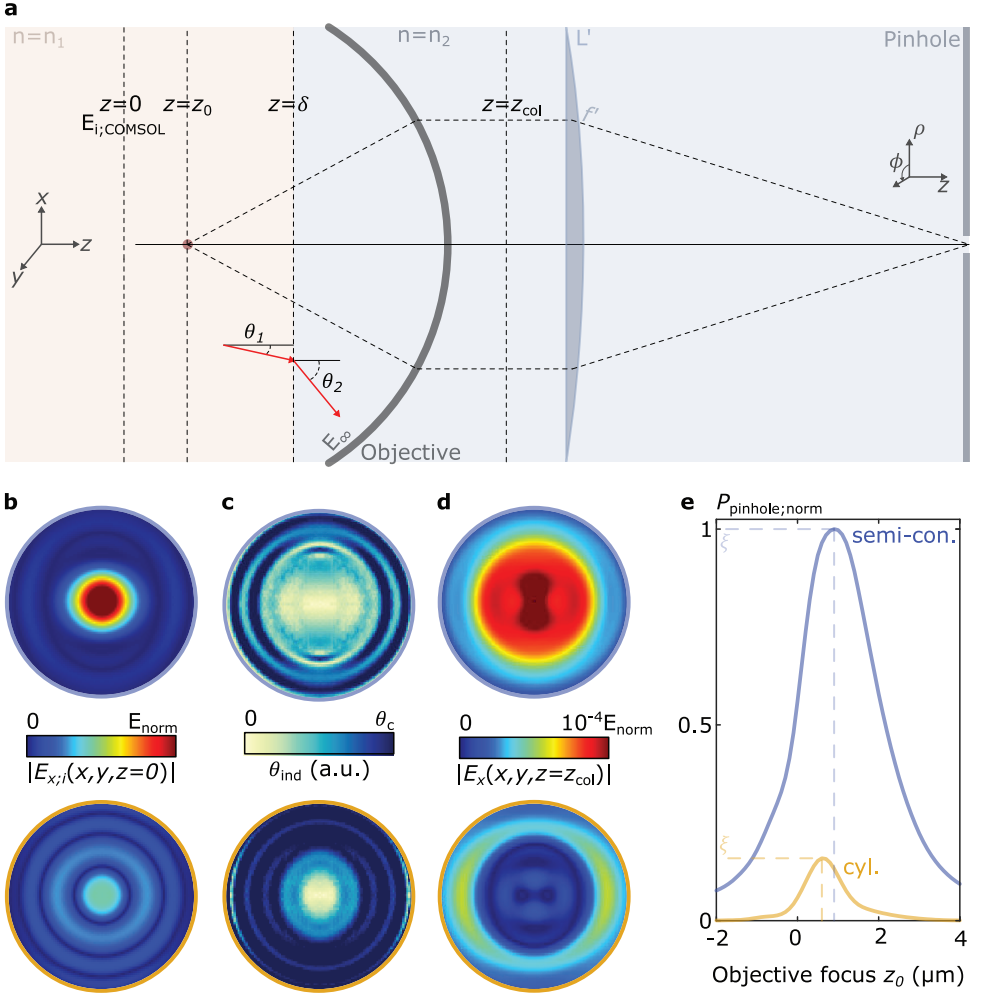
Figure 4.17: Estimating the collection efficiency from the COMSOL simulated electric field profiles. (a) To estimate the collection efficiency from the electric field computed at a location below the pillar base, which is still inside the diamond ($E_i(x, y, z = 0)$), we first compute how much light is transmitted at the diamond-air interface and subsequently passes through a high-NA objective. Finally, the collection efficiency is defined by how much power of the electric field can pass through a narrow pinhole ($r_{\text{pinhole}} = 25\,\mu\text{m}$) when focused via a low-NA lens (L') with focal distance $f' = 1\,\text{mm}$. Note that electric fields with large optical aberrations are more difficult to focus on a narrow pinhole, resulting in low collection efficiency. (b)-(d) Electric field associated with a top: semi-conical probe (as in §4.11a, with $d_T = 200\,\text{nm}$ and $d_B = 950\,\text{nm}$ and bottom: cylindrical probe with $d_T = 200\,\text{nm}$. (b) COMSOL simulated electric field profile at $z = 0$. (c) Incident angle associated with the electric field profile of (a). Light that is incident with angles larger than $\theta_1 > \theta_c = \sin^{-1}\left(\frac{n_2}{n_1}\right) = 0.43$ does not exit the diamond air interface. (d) Propagated electric field as if it passed through a high-NA objective for collimation. (e) Power of the electric field as it is passed through a narrow pinhole. We define the collection efficiency (ξ), evaluated at a single wavelength, from the maximum of (e). The distance δ is set to $2.8\,\mu\text{m}$ for all our calculations.

Having defined the field outside the diamond, we can now propagate the field $\vec{E}_t(\vec{k}, \delta)$

back to the centre of the reference sphere representing our objective (as if there is no interface with the $n = n_1$ medium):

$$\vec{E}_t(\vec{k}, z_0) = \vec{E}_t(\vec{k}, \delta) e^{i k_2 \cos\theta_2 (z_0 - \delta)} \tag{4.6}$$

Such that the field on the reference sphere becomes:

$$\vec{E}_\infty(\theta_2, \phi) = \frac{1}{2\pi i} k_2 \cos\theta_2 \frac{e^{i k_2 f}}{f} \vec{E}_t(\vec{k}, z_0) \tag{4.7}$$

Collimation by the objective leads to (Fig. 4.17d)

$$\vec{E}(\rho, \phi) = \frac{1}{\sqrt{\cos\theta_2}} \left(\vec{E}_\infty(\theta_2, \phi) \cdot \hat{\theta}_2 \right) \hat{\rho} + \left(\vec{E}_\infty(\theta_2, \phi) \cdot \hat{\phi} \right) \hat{\phi} \tag{4.8}$$

Where we have multiplied by $\sqrt{\frac{1}{\cos\theta_2}}$ for energy conservation.

We now focus the field onto a pinhole with a second, low-NA lens (L') of focal length $f' \gg \rho$. Then, the field in focus $z' = 0$ of the pinhole lens is given by (Fig. 4.17e):

$$\vec{E}(\vec{k}', z' = 0) = \vec{E}(\rho, \phi) \sqrt{\cos\theta'} \frac{2\pi i}{k_2 \cos\theta'} f' e^{-i k_2 f'} \tag{4.9}$$

where $\vec{k}' = \frac{f}{f'} \vec{k}$. Putting everything together, and assuming that the pinhole lens has a long focal length so that $\cos\theta' \approx 1$ and $\hat{\theta}' \approx \hat{\rho}$, the Fourier transform of the electric field at the pinhole is

$$\begin{aligned}
\vec{E}(\vec{k}', z' = 0) &= \frac{f'}{f} e^{i k_2 (f - f_2)} e^{i k_2 \cos\theta_2 (z_0 - \delta)} e^{i k_1 \cos\theta_1 \delta} \ldots \\
&\quad \sqrt{\cos\theta_2} \left(t_p (\vec{E}_i(\vec{k}, 0) \cdot \hat{\theta}_1) \hat{\rho} + t_s (\vec{E}_i(\vec{k}, 0) \cdot \hat{\phi}) \right) \\
&:= \frac{f'}{f} A \vec{E}_i(\vec{k}, 0)
\end{aligned} \tag{4.10}$$

The real-space profile is given by the inverse Fourier transform

$$\begin{aligned}
\vec{E}(x, y, 0) &= \iint \hat{E}(\vec{k}'; z' = 0) e^{i k'_x x + i k'_y y} dk'_x dk'_y \\
&= \frac{f}{f'} \iint A \hat{E}_i(\vec{k}, 0) e^{i \frac{f}{f'} k_x x + i \frac{f}{f'} k_y y} dk_x dk_y
\end{aligned} \tag{4.11}$$

so that

$$\vec{E}\left(\frac{f'}{f} x, \frac{f'}{f} y, 0\right) = \frac{f}{f'} \iint A \hat{E}_i(\vec{k}, 0) e^{i k_x x + i k_y y} dk_x dk_y \tag{4.12}$$

which shows how the magnification $\frac{f'}{f}$ re-scales the spatial coordinates and the amplitude of the field.

Finally, to obtain the emission power passed through the pinhole, we sum the components of the electric field amplitude squared while excluding the components that are focused onto radii beyond the pinhole radius. Finally, we repeat this evaluation for different objective focal distances z_0 and determine the maximum pinhole power, a figure of merit for the collection efficiency (Fig. 4.17e). Note that the pinhole power strongly depends on the wavelength at which the field was initially computed. As such, we average the pinhole power obtained for electric field profiles computed at 15 different linearly spaced wavelengths, defined across a wavelength range of 637 - 750 nm, representing the NV spectrum to obtain the average collection efficiency.

To perform calculations, we need to express the θ's in terms of ρ or v.v. using:

$$
\begin{aligned}
\hat{\rho} &= \cos\phi\hat{x} + \sin\phi\hat{y} \\
\hat{\phi} &= -\sin\phi\hat{x} + \cos\phi\hat{y} \\
\hat{\theta_2} &= \cos\theta_2\cos\phi\hat{x} + \cos\theta_2\sin\phi\hat{y} - \sin\theta_2\hat{z} \\
\hat{\theta_1} &= \cos\theta_1\cos\phi\hat{x} + \cos\theta_1\sin\phi\hat{y} - \sin\theta_1\hat{z} \\
\sin\theta_2 &= \frac{\rho}{f} \\
\cos\theta_2 &= \sqrt{1 - \rho^2/f^2} \\
\cos\theta' &= \sqrt{1 - \rho^2/f'^2} \\
\sin\theta_1 &= \frac{k_2}{k_1}\sin\theta_2 = \frac{k_2}{k_1}\frac{\rho}{f} \quad \text{(Snell's law)} \\
\cos\theta_1 &= \cos\left(\arcsin\left(\frac{k_2}{k_1}\sin\theta_2\right)\right) = \sqrt{1 - (\frac{k_2}{k_1}\frac{\rho}{f})^2}
\end{aligned}
\tag{4.13}
$$

5

Directional excitation of a high-density magnon gas using coherently driven spin waves

Controlling magnon densities in magnetic materials enables driving spin transport in magnonic devices. We demonstrate the creation of large, out-of-equilibrium magnon densities in a thin-film magnetic insulator via microwave excitation of coherent spin waves and subsequent multi-magnon scattering. We image both the coherent spin waves and the resulting incoherent magnon gas using scanning-probe magnetometry based on electron spins in diamond. We find that the gas extends unidirectionally over hundreds of micrometres from the excitation stripline. Surprisingly, the gas density far exceeds that expected for a boson system following a Bose-Einstein distribution with a maximum value of the chemical potential. We characterize the momentum distribution of the gas by measuring the nanoscale spatial decay of the magnetic stray fields. Our results show that driving coherent spin waves leads to a strong out-of-equilibrium occupation of the spin-wave band, opening new possibilities for controlling spin transport and magnetic dynamics in target directions.

5.1. INTRODUCTION

Spin waves are collective, wave-like precessions of spins in magnetically ordered materials. Magnons are the bosonic excitations of the spin-wave modes. The ability to control the number of magnons occupying the spin-wave energy band is important for driving spin transport in spin-wave devices such as magnon transistors[14, 63, 141, 142]. In addition, the generation of large magnon densities can trigger phenomena such as magnetic phase transitions[143], magnon condensation[16, 144, 145], and domain-wall motion[146–149]. As such, several methods to control magnon densities have been developed, with key methods including spin pumping based on the spin-Hall effect[63, 141, 150, 151], in which magnons are created by sending an electric current through heavy-metal electrodes, and microwave driving of ferromagnetic resonance (FMR)[79, 152–154] via metallic electrodes deposited onto the magnetic films.

Here, we demonstrate how the excitation of coherent, travelling spin-wave modes in a thin-film magnetic insulator can be used to generate a high-density, out-of-equilibrium magnon gas unidirectionally with respect to an excitation stripline. We characterize this process using scanning-probe magnetometry based on spins in diamond, a technique which enables probing magnons in thin-film magnets at microwave frequencies by detecting their magnetic stray fields[58, 84, 106, 154]. We find that the magnon gas has an unexpectedly high density that far exceeds the density expected for a magnon gas following a Bose-Einstein distribution with the maximum possible value of the chemical potential[155], opening new opportunities for creating and manipulating magnon condensates[16, 144, 145, 156]. We further characterize the gas by probing its momentum distribution through distance-dependent measurements of the stray-field magnetic noise it creates. The observed nanoscale spatial decay lengths reveal the presence of large-wavenumber magnons in the gas and underscore the need for nanometer proximity enabled by our scanning-probe magnetometer.

5.2. DETECTING SPIN WAVES USING SPINS IN DIAMOND.

Our scanning-probe magnetometer is based on nitrogen-vacancy (NV) ensembles embedded in the tip of a diamond probe (Fig. 5.1a)[52](SI Note 5.7.1-5.7.3). The electron spins associated with the NV centres act as magnetic-field sensors that we read out via their spin-dependent photoluminescence[106]. We use the NV sensors to locally characterize the magnetic stray fields generated by spin waves in a 235 nm-thick film of yttrium iron garnet (YIG)[157], a magnetic insulator with record-long spin-wave lifetimes[10]. We employ two measurement modalities to shed light on the interaction between coherently driven spin waves and the resulting out-of-equilibrium magnon gas at higher frequencies: in the first, we measure the coherent NV-spin rotation rate (Rabi frequency) to image the coherent spin waves excited by the stripline. In the second, we drive coherent spin waves with frequencies near the bottom of the spin-wave band while we measure the NV spin relaxation rates at frequencies hundreds of MHz above the drive frequency to characterize the local density of the magnon gas.
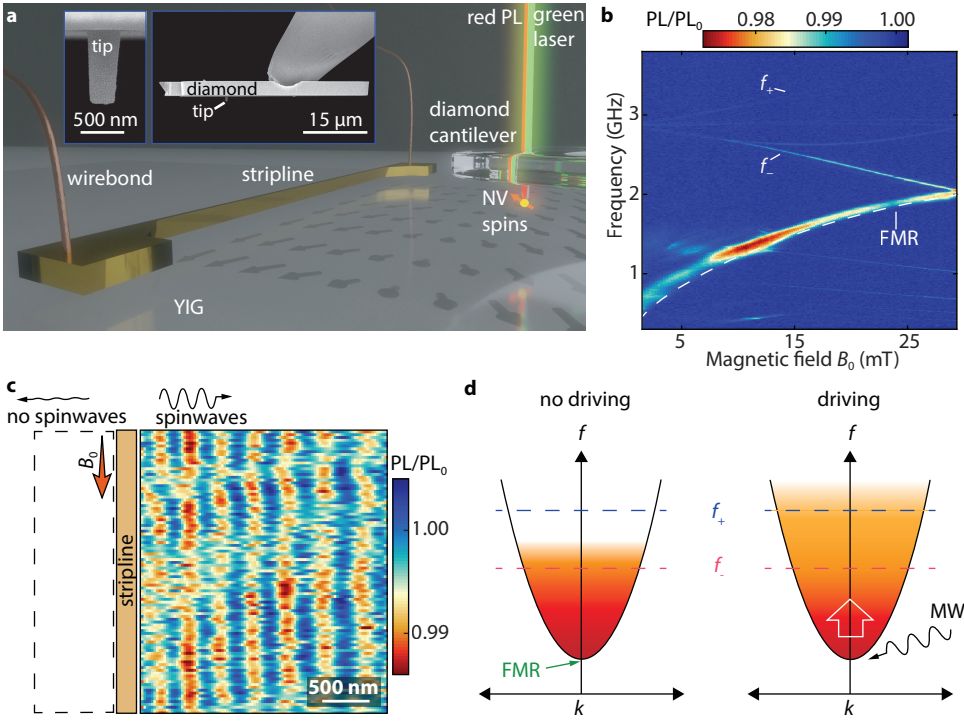
Figure 5.1: Detecting coherent spin waves and incoherent magnon densities using NV spins in diamond. (a) A diamond cantilever, with NVs implanted ∼ 20 nm below the tip surface, is mounted in an atomic force microscope (AFM) setup and used for probing the stray fields of spin waves that are excited by a gold stripline. The NV spins are initialized using green laser light and read out via spin-dependent photoluminescence (PL). Insets: scanning electron micrographs of diamond cantilever and tip. (b) Normalized NV photoluminescence vs external field B_0 and microwave drive frequency. The ESR frequencies ($f_\pm$) of the NV family that is most aligned with B_0 are labelled. The strong PL response close to the ferromagnetic resonance (FMR) is a result of the process depicted in (d). The FMR is calculated as $f_{\mathrm{FMR}} = \gamma \sqrt{B_{\mathrm{IP}}\left(B_{\mathrm{IP}} + \mu_0 M_{\mathrm{s}}\right)}$, where $\gamma = 28\,\mathrm{GHz\,T^{-1}}$, $\mu_0 = 4 \times 10^{-7}\,\mathrm{H\,m^{-1}}$, $M_{\mathrm{s}} = 1.42 \times 10^5\,\mathrm{A\,m^{-1}}$ and B_{IP} is the in-plane magnetic field component (SI Note 5.7.4). (c) Spatial map of the normalized NV ESR PL showing a coherent spin wave excited unidirectionally (to the right) by applying a microwave current at f_- through the stripline. On the left of the stripline there is no detectable spin-wave signal. The film is magnetized along the stripline direction by a magnetic field B_0 (orange arrow), which is set to a low value ($B_0 \approx 0\,\mathrm{mT}$) in this measurement. At each pixel, the measured PL under microwave driving is normalized to that without microwave driving (PL$_0$). The image is low-pass filtered to reduce pixel-by-pixel noise. (d) Sketch of the spin-wave dispersion (black line) and its occupation by magnons (colour gradient). Without microwave driving (left), only thermally excited magnons are present. Microwave (MW) driving near the FMR frequency (oscillating arrow in the right panel) increases the magnon density, which can be detected via the increased stray-field noise at the NV ESR frequencies ($f_\pm$).

We reveal the directionality of the coherent spin waves launched by the stripline by spatially mapping the contrast of the f_- ESR transition (Fig. 5.1c). At $B_0 \approx 0$, this transition is resonant with spin waves of wavelength ∼500 nm, as expected from the known spin-wave dispersion (SI Note 5.7.5). On the right-hand side of the stripline, we observe a spatial standing-wave pattern in the ESR contrast that results from the interference between the direct field of the stripline and the stray fields of the spin waves launched

by the stripline[58]. In contrast, we do not observe a spin-wave signal to the left of the stripline. This directionality is characteristic of coherent spin waves travelling perpendicularly to the magnetization and results from the handedness of the stripline field and the precessional motion of the spins[80].

5.3. UNIDIRECTIONAL EXCITATION OF A MAGNON GAS
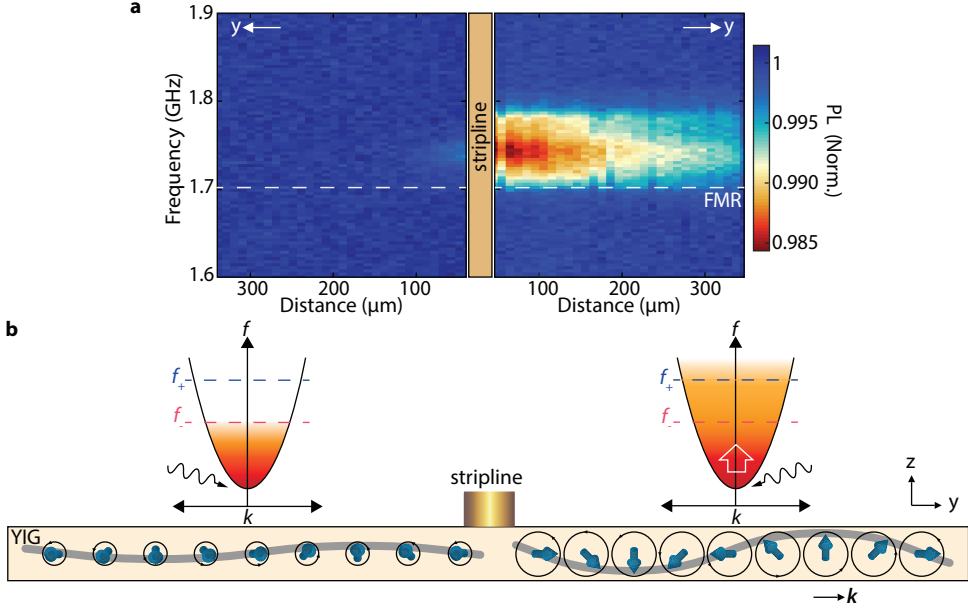
Figure 5.2: Unidirectional excitation of an out-of-equilibrium magnon gas by microwave driving near the ferromagnetic resonance. (a) One-dimensional spatial maps of the NV photoluminescence (PL) as a function of the frequency of a microwave drive current in the stripline. The microwave current excites directional coherent spin waves (travelling to the right in the image) at near-FMR frequencies. The decrease in NV photoluminescence is a result of incoherent magnons generated at the NV ESR frequencies via multi-magnon scattering (see schematics in (b)). An external magnetic field $B_0 = 20\,$mT magnetizes the film along the stripline direction. The NV ESR frequencies at this field can be seen in Fig. 5.1b. (b) Schematic of the directional excitation of a coherent spin wave by the microwave stripline and the accompanying out-of-equilibrium occupation of the spin-wave band that arises through multi-magnon scattering. The coherent spin waves are depicted as a collective, wave-like precession of the spins in the film (blue arrows). The increased excitation efficiency for right-propagating spin waves results in larger spin-wave amplitudes on the right-hand side (grey lines). The spin-wave band is schematically depicted by a parabolic dispersion. The microwave field that drives the coherent spin waves is indicated by the oscillating arrow. The out-of-equilibrium occupation of the spin-wave band is indicated by the colour gradient (as in Fig. 5.1d.) The NV detection frequencies $f_\pm$ are indicated by dashed lines.

In addition to the narrow lines of reduced photoluminescence indicating the NV ESR frequencies (Fig. 5.1b), we observe a broad band of photoluminescence reduction close to the expected ferromagnetic resonance (FMR) frequency of our YIG film that is detuned from the NV ESR transitions. A similar off-resonant NV response was observed previously [79, 84, 154, 157–160], and has been attributed to the driving of a uniform FMR

mode and subsequent multi-magnon scattering. The scattering processes lead to an increased magnon density at the NV ESR frequencies, causing NV spin relaxation[79, 154] (Fig. 5.1d). However, in contrast with the uniform nature of the FMR mode, we observe that the signal strength depends strongly on the detection location with respect to the stripline (Fig. 5.2a): on the right-hand side, we observe a much stronger response than on the left, up to distances 300 μm away from the stripline. This asymmetry shows that directional spin waves excited by the stripline, such as those in Fig. 5.1c, underlie the increased magnon densities at the NV ESR frequencies (Fig. 5.2b).
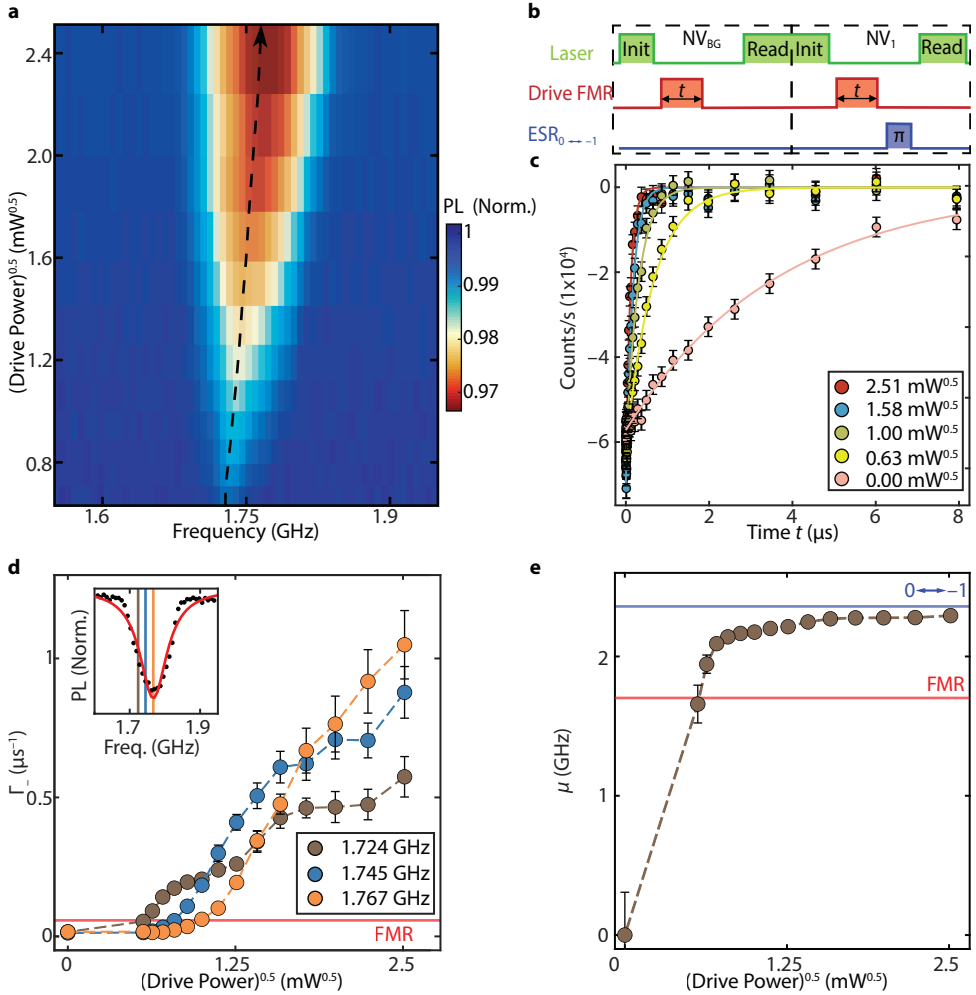
5.4. MAGNON DENSITY UNDER NEAR-FMR DRIVING

Next, we study the density of the magnon gas created via the driving of directional spin waves. Magnons can redistribute over the spin-wave band through magnon-magnon interactions and lead to an equilibrated occupation described by a Rayleigh-Jeans distribution[16] with chemical potential μ[156]: $n(f,\mu) = \frac{k_B T}{hf - \mu}$ (which is the high-temperature limit of the Bose-Einstein distribution, appropriate for our room-temperature measurements), here k_B is Boltzmann's constant, T is the temperature, h is Planck's constant and f is the probe frequency. To study whether the magnon gas (Fig. 5.2a) is described by this distribution, we monitor the magnon density at the f_- ESR frequency while driving directional spin waves. To determine which drive frequency yields the strongest NV response, we first characterize the NV photoluminescence while sweeping the frequency and power of the microwave drive field (Fig. 5.3a). Then, we apply the microwave drive at a frequency near the frequency of maximum response and characterize the increase in magnon density at the f_- ESR frequency by measuring the NV relaxation rate Γ_- between the 0 and –1 spin states (Fig. 5.3b-c) (SI Note 5.7.6). Under the near-FMR driving, f_- frequency magnons are added to the magnon gas as the scattering products of magnon-magnon interactions, resulting in an enhanced Γ_-. We measure Γ_- at several drive frequencies (Fig. 5.3d), as the location of maximum NV response changes slightly with drive power (Fig. 5.3a). For all drive frequencies, we observe a strong increase in the relaxation rate for increasing drive power, reaching up to 60 times its equilibrium value. Consistent with previous observations[154], this process is strongly non-linear, as can be seen from the threshold power required to increase the relaxation rate at the higher drive frequencies.

If the magnon density is described by the Rayleigh-Jeans distribution, then we can determine the chemical potential by measuring the NV relaxation rates using[79]:

$$\mu = hf_- \left(1 - \frac{\Gamma_-(0)}{\Gamma_-(\mu)}\right) \tag{5.1}$$

where $\Gamma_-(0)$ is the relaxation rate in the absence of microwave driving and $\Gamma_-(\mu)$ is the relaxation rate measured at a raised chemical potential caused by driving coherent spin waves. A key characteristic of the chemical potential for a bosonic system is that its maximum value is set by the bottom of the energy band[79, 155], which in our system is located about 400 MHz below the FMR (at 20 mT) as can be calculated from the spin-wave dispersion (SI Note 5.7.5). Using Eq. 5.1 to calculate the chemical potential from the measured NV relaxation rates (Fig. 5.3d), we find values far above the FMR, thereby

Figure 5.3: Characterizing the density of the magnon gas under near-FMR driving using NV relaxometry. (a) Normalized NV photoluminescence (PL) versus microwave drive frequency and the square root of the power, which is linear with the amplitude of the applied microwave field. The maximum contrast shifts with drive power (dashed black line). (b) Measurement sequence to characterize the magnon density at the f_- NV ESR frequency: a $2\,\mu s$ laser pulse (green, Init) prepares the NV spins in $|0\rangle$. A variable-duration microwave pulse (red) causes an out-of-equilibrium magnon density that induces NV spin relaxation. Two sequences are performed, with and without a microwave π-pulse. The π-pulse at the f_- ESR frequency switches the $|0\rangle$ and $|-1\rangle$ populations of the target NV spins. The final spin state is characterized by measuring the PL during the first 600 ns of a laser pulse (green, Read). The PL difference between the two sequences enables the extraction of the $|0\rangle \leftrightarrow |-1\rangle$ relaxation rate of the target NV spins assuming negligible $|0\rangle \leftrightarrow |+1\rangle$ relaxation (SI Note 5.7.6). (c) Relaxation rate measurement of the PL difference between the two sequences versus the duration of the spin-wave drive pulse (see (b)) for different drive powers at $B_0 = 20\,mT$. Filled circles: data. Solid lines: fits to $Ae^{(-2\Gamma_- t)}$, where A is an offset and Γ_- the $|0\rangle \leftrightarrow |1\rangle$ relaxation rate. The error bars represent uncertainties stemming from photon shot noise. (d) Γ_- versus the square root of the drive power for three near-FMR drive frequencies, extracted from measurements as in (b-c). The red line labelled 'FMR' indicates the maximum rate for a system described by a chemical potential that saturates at the bottom of the spin-wave band. Error bars determined from fits. Inset: Normalized NV PL versus microwave drive frequency at $2.51\,mW^{0.5}$ microwave power (see (c)). The vertical lines indicate the drive frequencies used for the measurements in the main panel. (e) Effective chemical potential as a function of the square root of the drive power. Blue line: ESR transition frequency (2.359 GHz). Red line: Calculated FMR frequency (1.702 GHz).

exceeding this maximum (Fig. 5.3e). We, therefore, conclude that the magnon gas created by near-FMR driving cannot be described by the Rayleigh-Jeans distribution with a finite chemical potential. Presumably, the magnon density is instead concentrated in a finite frequency range near the bottom of the spin-wave band that includes our detection (ESR) frequency. The strong increase in magnon density, compared to that observed in thinner YIG films[79], might be related to the lower threshold power needed for triggering non-linear spin-wave responses in thicker magnetic films[160]. Spectroscopic techniques such as Brillouin Light Scattering[16, 161] could shed further light on the spectral characteristics of the out-of-equilibrium magnon gas.

5.5. WAVENUMBER CONTENT OF INCOHERENT MAGNONS

The Rayleigh-Jeans distribution describes an equal population of the spin-waves mode at a given frequency (i.e. the Rayleigh-Jeans occupation factor does not depend on the wavevector of the mode). We now study whether the spatial frequency content of the magnon gas created by near-FMR driving can be distinguished from that corresponding to a Rayleigh-Jeans occupation via distance-dependent measurements of the NV relaxation rate. To do so, we measure the spatial decay of the spin-wave stray fields away from the film, which is determined by the spatial frequencies (wavenumbers) of the magnons that generate the fields[73]. We observe that the stray fields associated with the incoherent magnon gas decay much more rapidly with increasing NV-film distance than the stray fields generated by the coherently driven spin waves at the NV ESR frequency (Fig. 5.4a). To quantify this difference, we first characterize the decay of the stray field B_{SW} of a coherent spin wave with a single, well-defined wavenumber k_{SW} that we excite by applying a microwave drive resonant with the f_- NV ESR frequency using the stripline. The amplitude of this field decays exponentially with distance d according to[58]:

$$B_{SW} \propto e^{-k_{SW}d} \tag{5.2}$$

Because the excitation frequency is resonant with the NV ESR frequency, the field B_{SW} drives coherent NV spin rotations (Rabi oscillations) with a rotation rate (Rabi frequency, Ω_R) that is proportional to the stray-field amplitude[58]: $\Omega_R \propto B_{SW}$.

To quantify the decay length, we measure the NV Rabi frequency, Ω_R as a function of the tip-sample distance (Fig. 5.4b). By fitting the spatial decay using $\frac{\Omega_R}{\Omega_R(d=0)} = e^{(-k_{SW}d)}$, we extract wavenumber, k_{SW} of the spin waves and the corresponding decay length, l_{decay} which ranges between ~ 0.65 and $2.7\,\mu m$ depending on the external field B_0 (Fig. 5.4d, blue dots). We find a good agreement with the wavenumber calculated from the spin-wave dispersion (Fig. 5.4d, blue filled area, SI Note 5.7.5), demonstrating the power of height-dependent measurements for determining spatial frequencies.

We find that the stray fields of the out-of-equilibrium magnon gas, generated upon driving near the FMR, decay on a much shorter length scale, i.e., $\sim 280\,nm$ at $B_0 = 20\,mT$ (Fig. 5.4a). To quantify the corresponding decay length, we measure the NV relaxation rate Γ_- at different tip-sample distances d (Fig. 5.4c). By fitting the spatial decay of the relaxation rate using an exponential approximation $\frac{\Gamma_-}{\Gamma_-(d=0)} = e^{-d/l_{decay}}$, we observe that
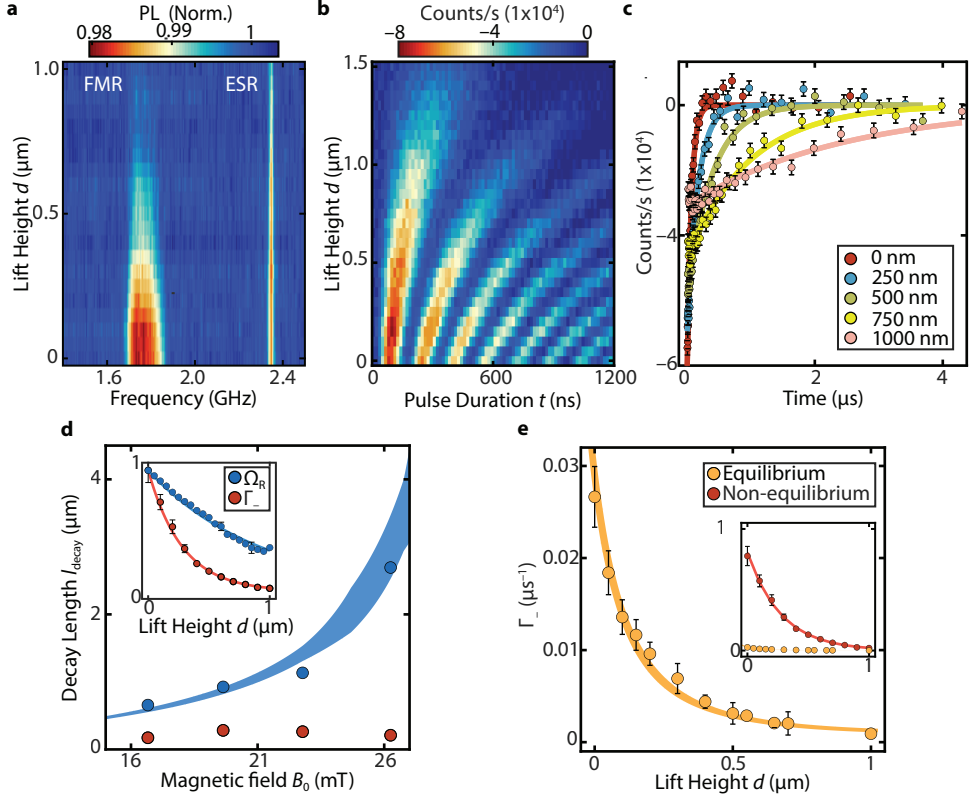
Figure 5.4: Characterizing the wavenumber content of the equilibrium and out-of-equilibrium magnon gases. (a) Normalized NV photoluminescence (PL) vs tip lift height d and microwave drive frequency, measured at ~150 μm to the right of the stripline. The decay of the signal for increasing lift height is caused by the decay of the spin-wave stray fields driving the NV spins. The tip touches the sample at 0 μm. (b) Coherent NV spin rotations (Rabi oscillations) vs lift height d. The rotations are driven by a coherent spin-wave pulse of varying duration launched by the stripline at the f_- ESR frequency at $B_0 = 20$ mT. The measurement was performed at 37 μm to the right of the stripline. (c) NV spin relaxation measurements for different tip lift heights. $B_0 = 20$ mT. Filled circles: data. Solid lines: fits to PL $= Ae^{(-2\Gamma_- t)}$. (d) Measured spatial decay length of the stray field of the driven coherent spin waves (blue circles) and of the out-of-equilibrium magnon gas (red circles) vs B_0. The blue band indicates the expected decay length for a coherent spin wave that is resonant with the NV ESR frequency, determined by calculating the spin-wavelength from the spin-wave dispersion while considering an uncertainty of ± 10 nm in film thickness[58], the $\pm 1.8°$ uncertainty in the angle between the diamond cantilever and the YIG surface, and the uncertainty in the angle of B_0 (SI Note 5.7.4). Inset: Spatial decay of the NV Rabi frequency (Ω_{Rabi}) when the Rabi oscillations are driven via coherent spin waves (blue circles) and of the NV relaxation rate (Γ_-) caused by the out-of-equilibrium magnon gas (red circles) at $B_0 = 20$ mT. Solid lines: fits to $Ae^{-d/l_{\text{decay}}}$. (e) NV relaxation rate vs lift height d without microwave drive (orange circles). Orange line: calculation for an equilibrium occupation of the spin-wave band. The width of the line considers the uncertainties discussed in (e). Inset: Comparison of the spatial decay of the NV relaxation rates without (as in the main panel, orange circles) and with microwave drive (as in inset in (d), red circles) near the FMR. $B_0 = 20$ mT. Red line: fit to $\Gamma_- = Ae^{-d/l_{\text{decay}}}$. The two lines possess a similar decay constant.

the decay length l_{decay} is below 1 μm over the entire range of B_0 (Fig. 5.4d, red dots). This short decay length contrasts with that measured for the coherent spin waves (Fig. 5.4d,

blue dots), reflecting the additional presence of large-wavenumber magnons in the incoherent magnon gas.

To examine if this is different for a magnon gas in equilibrium, we compare the NV relaxation rates measured in the absence of microwave driving to a calculation of the stray-field noise generated by a magnon gas in thermal equilibrium with zero chemical potential (Fig. 5.4e). This calculation is based on a model[73] that assumes a Rayleigh-Jeans occupation of the spin-wave band and calculates the stray-field noise at the NV ESR frequency by summing the contributions of all spin-wave modes at this frequency (SI Note 5.7.5 & Fig. 5.4e, orange line). This model was recently demonstrated to accurately describe the stray-field noise of thin magnetic films[73]. We find a quantitative match with the measured equilibrium NV relaxation rate $\Gamma_-(\mu = 0)$ if we assume a $0.28 \pm 0.3\,\mu$m distance offset of the NV centres at zero tip-lift height (Fig. 5.4e). This offset is larger than the NV implantation depth of ~ 20 nm, which could be caused by small particles picked up by the tip during scanning. We compare the measured relaxation rate under near-FMR driving to the same model scaled by a prefactor to account for the larger magnon occupation under near-FMR driving. Because the rate (Fig. 5.4e) is well described by this model, we conclude that the spatial frequency content of the incoherent magnon gas cannot be distinguished from a homogeneous k-space occupation such as that expected for a Rayleigh-Jeans distribution. Furthermore, the calculations confirm that the spatial decay length should not depend strongly on the external field B_0 (SI Note 5.7.5), consistent with the measurements shown in Fig. 5.4d.

5.6. CONCLUSIONS

We have shown that coherent spin waves enable the generation of a high-density magnon gas unidirectionally with respect to an excitation stripline. The threshold power required to trigger this process underscores the nonlinearity of the underlying magnon scattering. From the more than 10-fold increase of the stray-field noise under near-FMR driving, probed via relaxometry measurements of our sensor spin, we conclude that the resulting magnon gas cannot be described by a Rayleigh-Jeans occupation of the spin-wave band. We demonstrate that the spatial decay length of the spin-wave stray fields contains valuable information about the spatial frequencies of the spin waves generating the fields. The observed sub-micron spatial decay lengths of the stray fields generated by the out-of-equilibrium magnon gas indicate the presence of large-wavenumber magnons and highlight the need for proximal sensors such as the scanning-probe NV magnetometer. Further controlling the directionality of the excited coherent spin waves by, e.g., shaping stripline geometries and/or tuning the direction of the external magnetic field could enable delivering high-density magnon gases to target locations in a magnetic film or device. Targeted delivery of high-density magnons gases provides new opportunities for controlling spin transport and for triggering magnetic phenomena such as phase transitions[143], magnon condensation [16, 144, 145], and spin-wave-induced domain-wall motion[146–149].

Acknowledgements

5.7. Supporting Information

5.7.1. YIG Sample

We study a 235 ± 10 nm thick film of (111)-oriented ferrimagnetic insulator yttrium iron garnet (YIG) grown on a gadolinium gallium garnet substrate by liquid-phase epitaxy (Matesy GmbH). The stripline (length of 2 mm, width of 30 μm, and thickness of 200 nm) used for spin-wave excitation was fabricated directly on the YIG surface using *e*-beam lithography, using a double layer PMMA resist (A8 495K / A3 950K) and a top layer of Elektra92, followed by the deposition of 5 nm / 200 nm of Cr/Au.

5.7.2. Measurement setup

Our scanning NV-magnetometry setup is equipped with two stacks of Attocube positioners (ANPx51/RES/LT) and scanners (ANSxy50/LT and ANSz50/LT) that allow for individual positioning of the tip and sample. We first position the NV tip in the focus point of the objective (LT-APO/VISIR/0.82) and use the scanners of the sample stack to create spatial PL images (lateral and height). To record the NV PL, we use our home-built confocal setup, which is equipped with a 515 nm green light laser (Cobolt 06-MLD, pigtailed) for NV excitation. We use a fibre collimator (Schäfter+Kirchhoff 60FC-T) to couple the laser into free space. A dichroic mirror (Semrock Di03-R532-t3-25x36) is used to reflect the green laser light, which is then focused by the objective lens (LT-APO/VISIR/0.82) on the tip of a homemade all-diamond cantilever probe (SI Note 5.7.3). The shape of the tip aides the guiding of the NV PL back towards the objective, where it is collimated and transmitted by the dichroic mirror and additionally filtered by a long-pass filter (BLP01-594R-25) before it is focused on the chip of an avalanche photodiode (APD) (Excelitas SPCM-AQRH-13). The resulting signal is collected and counted by a National Instruments DAQ card. A SynthHD (v2) dual-channel microwave generator (Windfreak Technologies, LLC) is used for driving the NVs and exciting the spin waves. High-speed pulse sequences are generated by a PulseBlasterESR-PRO pulse generator (SpinCore Technologies, Inc.).

5.7.3. DIAMOND TIP FABRICATION

NV IMPLANTATION

Our scanning tip is fabricated from a (001)-oriented electronic grade type IIa diamond grown via chemical vapour deposition by Element 6. The diamond is laser cut and polished (Almax EasyLab) into 2x2x0.05 mm^3 chips and subsequently cleaned in fuming nitric acid. To remove surface damage from the polishing [111], we use inductively coupled plasma reactive ion etching (ICP-RIE) to remove the top 5 μm. The diamond is implanted with 15N ions at 6 keV with a dose of 10^{13} ions/cm^2 by INNOViON. After implantation, we clean the samples in a tri-acid solution (H_2SO_4:$HClO_4$: HNO_3 = 1:1:1) at 120 °C for 1 hour. We then anneal the diamond for 8 hours at 800 °C at approximately 10^{-6} mbar, followed by another cleaning step in a tri-acid solution.

STRUCTURING DIAMOND

To structure the diamond into a scanning tip and for mounting this tip in our AFM setup, we follow Refs. [52, 111]. We first thin down the ~45 μm thick diamond to ~5-7 μm in a 1.2x1.2 mm^2 area in the center [111, 121]. The diamond is then flipped with the NV side facing up and glued (with PMMA) to a silicon carrier wafer to enable spin coating. A 40-50 nm titanium etch mask is deposited using RF-magnetron sputtering, and a layer of about 800 nm PMMA (950K A8) is spin coated and patterned using *e*-beam lithography into 20x50 μm^2 rectangular masks. The mask is then transferred into the titanium using SF6/He plasma RIE. Subsequently, an anisotropic oxygen etch transfers the cantilevers into the diamond with a thickness of about 3 μm [111, 121]. We clean the sample using hexafluoride (40%, HF) and deposit a new layer of 5 nm of titanium to improve the adhesion of the FOx-16 resist that we spincoat subsequently and which serves as the etch mask for the 1.5 μm tall diamond pillars that are created in a final anisotropic oxygen etch. The resulting tips have a diameter of approximately 300 nm and therefore contain about 100 NVs at 20 nm below its apex. The diamond is cleaned to get rid of the titanium/FOx mask in HF and fuming nitric acid (100%) to remove possible organic contaminants. Finally, the diamond tip is glued (UV glue) to the end of a pulled optical fibre that is connected to a tuning fork for AFM operation[111].

5.7.4. MAGNETIC FIELD CALIBRATION

In our experiments, we apply the magnetic external field $\vec{B}_0$ using a permanent magnet (S-10-20-N, Supermagnete) onto a linear translation stage (MTS25-Z8, Thorlabs, controlled by a KDC101 Thorlabs servo motor). To vary the strength of the external field, we change the position of the stage to bring the magnet closer to the sample and tip. We orient the magnet in such a way that the field aligns with one of the four NV families[i] (which is 54.7 ± 1.8° with respect to the normal of the YIG surface) and to magnetize the YIG film along the length of the stripline. At each magnetic field, we calibrate its magnitude and orientation by measuring the eight ESR frequencies $f_{i=1-8}$ of the four NV families(NV$_{1-4}$) (Fig. 5.1b, main text). From these frequencies we determine $\vec{B}_0$ by

---

[i]with 'NV family', we mean the collection of NV centres with the same crystallographic orientation

performing a least square minimization[162]:

$$\min\left(\sum_{i=1}^{8}(f_i - f_i^{\text{calc}}(\vec{B}))^2\right) \tag{5.3}$$

where f_i^{calc} are the eight ESR frequencies calculated from the NV Hamiltonian at a magnetic field $\vec{B}$ [84]:

$$H = DS_Z^2 + \gamma\vec{B}\cdot\vec{S}. \tag{5.4}$$

Here, D is the zero-field splitting (2.87 GHz), $S_{i=X,Y,Z}$ are the Pauli spin-1 matrices, and γ is the electron gyromagnetic ratio (28 GHz/T). Capital XYZ denotes the NV frame. The Z-axis is taken along the NV axis and thus differs for the four NV families, pointing along the unit vectors

$$\hat{n}_{\text{NV}} = \frac{1}{\sqrt{3}}(\pm 1, \pm 1, 1) \tag{5.5}$$

expressed in the lab/diamond frame. The microwave stripline is oriented along the [110] direction in this frame.

After fitting the eight ESR frequencies, $f_{i=1-8}$, (Fig. 5.5a),we extract the magnetic field components (B_x, B_y, B_z) (Fig. 5.5b), the magnetic-field magnitude B_0 and the corresponding out-of-plane angle, θ, and in-plane angle, φ (Fig. 5.5c). Lowercase xyz refers to the lab frame.

The field is oriented in-plane up to 10 mT (see B_z, Fig S.1b), after which the out-of-plane component is increased such that the field matches the target NV axis at 30 mT (red dashed line in Fig. 5.5c). This ensures a good f_- ESR contrast over the entire field range [95].
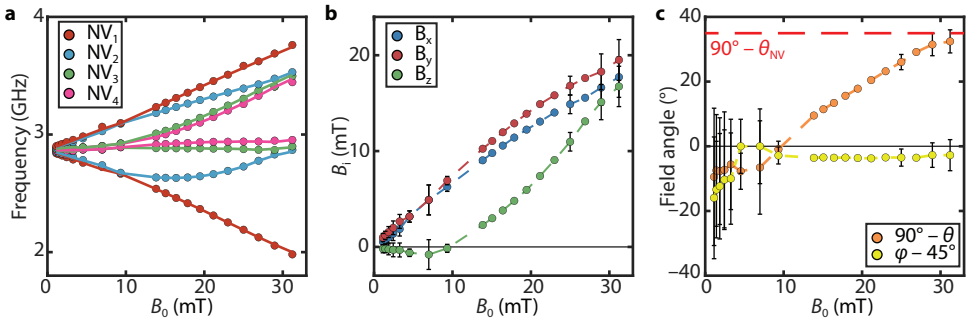
Figure 5.5: Vector magnetic field determination. (a) The eight ESR frequencies as a function of applied external magnetic field (B_0). Filled circles: data. Solid lines: fitted ESR frequencies obtained by performing a least square minimization of Eq. (5.3) at each field. (b) The magnetic field components (B_x, B_y, B_z) as a function of the field magnitude B_0. The error bars represent 95% confidence bounds. (c) The magnetic field angles as a function of B_0. The error bars represent 95% confidence bounds.

5.7.5. NV RELAXATION INDUCED BY THERMAL MAGNONS

We follow the approach of Rustagi et al.[73] to calculate the NV relaxation rates induced by the magnons in our YIG film using

$$\Gamma_\mp(\omega_\mp) = \frac{\gamma^2}{2} \int \frac{d\vec{k}}{(2\pi)^2} \sum_{i,j \in \{x,y\}} \mathscr{D}^{\text{eff}}_{\pm i}(\vec{k}) \mathscr{D}^{\text{eff}}_{\mp j}(-\vec{k}) C_{ij}(\vec{k}, \omega_\mp). \tag{5.6}$$

Here, $\Gamma_\mp$ are the relaxation rates corresponding to the $\omega_\mp$ ESR frequencies, $\vec{k}$ is the spin-wavevector, $\mathscr{C}$ is a spin-spin correlator describing the thermal magnon fluctuations, and $\mathscr{D}^{\text{eff}}$ is a dipolar tensor that calculates the magnetic stray fields that induce NV spin relaxation generated by these fluctuations. We will now summarize how these quantities are calculated for our measurement geometry. In addition, we will discuss the expected distance dependence of the relaxation rate that we compared with experiments in Fig. 5.4e of the main text.

The thermal transverse spin fluctuations in the film are described by [73]:

$$C_{ij}(\vec{k}, \omega) = 2D_{th} \sum_{\nu = \{x,y\}} S_{i\nu}(\vec{k}, \omega) S_{j\nu}(-\vec{k}, -\omega) \tag{5.7}$$

where $D_{\text{th}} = \frac{\alpha k_B T}{\gamma M_s L}$, with k_B the Boltzmann constant, T the temperature, and

$$S(\vec{k}, \omega) = \frac{\gamma}{\Lambda} \begin{bmatrix} \omega_3 - i\alpha\omega & -\omega_1 - i\omega \\ -\omega_1 + i\omega & \omega_2 - i\alpha\omega \end{bmatrix} \tag{5.8}$$

is the spin-wave susceptibility, with[73]

$$\omega_0(\vec{k}) = \omega_B \cos(\theta_0 - \theta) - \omega_M \cos^2\theta_0 + \omega_D k^2, \tag{5.9}$$

$$\omega_1(\vec{k}) = \omega_M f_k \sin\phi_k \cos\phi_k \cos\theta_0, \tag{5.10}$$

$$\omega_2(\vec{k}) = \omega_0 + \omega_M \left[f_k \cos^2\phi_k \cos^2\theta_0 + (1 - f_k) \sin^2\theta_0 \right], \tag{5.11}$$

$$\omega_3(\vec{k}) = \omega_0 + \omega_M f_k \sin^2\phi_k, \tag{5.12}$$

$$\Lambda(\omega) = (\omega_2 - i\alpha\omega)(\omega_3 - i\alpha\omega) - \omega_1^2 - \omega^2. \tag{5.13}$$

Here, $f_k \equiv 1 - (1 - e^{-kL})/(kL)$ with L the film thickness, and ϕ_k is the polar angle of a spin wave in k-space. The spin-wave dispersion is obtained by taking the real part of the solutions of $\Lambda = 0$. To calculate S we use $L = 235 \pm 10$ nm, Gilbert damping $\alpha = (1.2 \pm 0.1) \cdot 10^{-4}$, $M_s = (1.42 \pm 0.01) \cdot 10^5$ A/m [58] and $A_{\text{ex}} = (3.7 \pm 0.4) \cdot 10^{-12}$ J/m [163]. The equilibrium angle of the magnetization θ_0 is obtained by finding the minimum of the free energy at each magnetic field value (θ_0 is in-plane to within a few degrees for the field range used in our measurements).

The dipolar tensor $D^{\text{eff}}(\vec{k}, \omega)$ calculates the magnetic stray fields that induce NV spin relaxation generated by the thermal magnons in the film. Because the correlator C is expressed in the frame of the magnet (with a z-axis pointing along the equilibrium magnetization), $D^{\text{eff}}(\vec{k}, \omega)$ is obtained by first rotating the magnet frame to the lab frame,

then multiplying by the dipolar tensor $\mathscr{D}(\vec{k})$ in the lab frame, and then rotating the result to the NV frame: $D^{\text{eff}}(\vec{k},\omega) = R_{yz}(\theta_{\text{NV}},\phi_{\text{NV}})\mathscr{D}(\vec{k})R_Y(\theta_0)^T$, where

$$\mathscr{D}(\vec{k}) = -\frac{\mu_0 M_s}{2}e^{-|\vec{k}|d_{\text{NV}}}(1-e^{-|\vec{k}|L})\begin{bmatrix} \cos^2\phi_k & \sin(2\phi_k)/2 & i\cos\phi_k \\ \sin(2\phi_k)/2 & \sin^2\phi_k & i\sin\phi_k \\ i\cos\phi_k & i\sin\phi_k & -1 \end{bmatrix} \qquad (5.14)$$

where μ_0 is the vacuum permeability and d_{NV} is the distance between the NV and the sample surface. The terms in Eq.5.6 that induce spin relaxation are given by[73]: $\mathscr{D}^{\text{eff}}_{\pm v} = \mathscr{D}^{\text{eff}}_{xv} \pm i\mathscr{D}^{\text{eff}}_{yv}$.

For a magnon gas in thermal equilibrium, in the absence of microwave driving, the dependence of the NV relaxation rate on the NV-sample distance can be calculated using Eq.5.6. We find a good match between the calculated and measured rate (Fig. 5.4e, main text) if we include an offset distance of 0.28 ± 0.03 μm. This offset distance is larger than the 20 nm NV implantation depth, which could be caused by small particles picked up by the tip during scanning. We observe a similarly fast decay over a broad range of magnetic field values (Fig. 5.6).
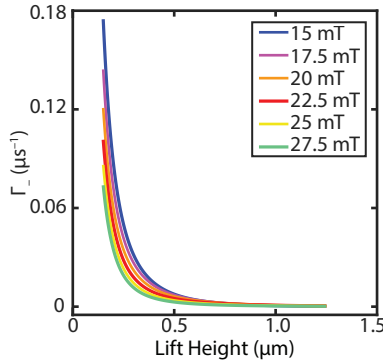
Figure 5.6: Calculated relaxation rate as a function of tip lift height for an in-equilibrium occupation of the spin-wave band for different magnetic fields. We used $\theta_{\text{NV}} = 54.7°$ and field-angle $\theta = 71.7°$ with respect to the surface normal.

5.7.6. EXTRACTING THE NV RELAXATION RATE
In this section, we describe how we obtain the relaxation rate of a target NV family, plotted in Figs. 5.3 and 5.4 of the main text[i]. To extract the Γ_- relaxation rate of the target NV family, we apply the pulse sequence shown in Fig. 5.3b of the main text. We perform two sequences: without and with a microwave π-pulse on the $|0\rangle \leftrightarrow |-1\rangle$ ESR transition of the target NV family. For the measurement without a π-pulse, we write the photoluminescence collected during readout as:

$$N(t) = p_0(t)N_0 + p_{-1}(t)N_{-1} + p_{+1}(t)N_{+1} + N_{\text{BG}} \qquad (5.15)$$

where $N_{i=-1,0,+1}$ are the number of collected photons when the target NVs are in state i and $p_{i=-1,0,+1}$ are the associated occupation probabilities. N_{BG} is the background PL,

which includes the contribution of the other NV families.

Applying a π-pulse on the $|0\rangle \leftrightarrow |-1\rangle$ transition of the target NV family switches the populations of these states. The photoluminescence collected during readout is now

$$N_\pi(t) = p_{-1}(t)N_0 + p_0(t)N_{-1} + p_{+1}(t)N_{+1} + N_{\mathrm{BG}} \tag{5.16}$$

By taking the difference of equations (5.15) and (5.16), the background contribution drops out, giving

$$N - N_\pi = (p_0(t) - p_1(t))(N_0 - N_{-1}) \tag{5.17}$$

For the field range used in our experiments $\Gamma_+ \ll \Gamma_-$ [73] because the ω_+ transition is far detuned from the FMR and moreover less affected by the fields produced by the spin waves in the YIG film. As such, the time dependence of $N - N_\pi$ is dominated by the Γ_- relaxation rate and follows an exponential decay $N - N_\pi = Ae^{-2\Gamma_- t}$ that we use to extract Γ_-.

6

FILTERING AND IMAGING OF FREQUENCY-DEGENERATE SPIN WAVES USING NANOPOSITIONING OF A SINGLE-SPIN SENSOR

Nitrogen-vacancy (NV) magnetometry is a new technique for imaging spin waves in magnetic materials. It detects spin waves by their microwave magnetic stray fields, which decay evanescently on the scale of the spin-wavelength. Here, we use nanoscale control of a single-NV sensor as a wavelength filter to characterize frequency-degenerate spin waves excited by a microstrip in a thin-film magnetic insulator. With the NV probe in contact with the magnet, we observe an incoherent mixture of thermal and microwave-driven spin waves. By retracting the tip, we progressively suppress the small-wavelength modes until a single coherent mode emerges from the mixture. In-contact scans at low drive power surprisingly show occupation of the entire isofrequency contour of the two-dimensional spin-wave dispersion despite our one-dimensional microstrip geometry. Our distance-tunable filter sheds light on the spin-wave band occupation under microwave excitation and opens opportunities for imaging magnon condensates and other coherent spin-wave modes.

S PIN waves are collective spin excitations of magnetically ordered materials, with as-
sociated quasi-particles called magnons[164]. Due to their low damping, spin waves
are promising as information carriers in information-technology devices[12, 14, 60, 63].
Techniques to image spin waves aid in studying such devices and realizing their techno-
logical potential. As such, several imaging techniques have been developed, with most
established techniques based on the spin-dependent scattering of photons[72, 165, 166].

Nitrogen-vacancy (NV) magnetometry images spin waves by their microwave magnetic
stray fields. It uses the electronic spin of the NV lattice defect in diamond as a sen-
sor, which can be read out through spin-dependent photoluminescence (PL), is atomic-
sized, and can stably exist within nanometres from the diamond surface[29, 167]. This
enables magnetic imaging with nanoscale spatial resolution and high sensitivity. The
NV spin allows probing spin-wave spectra with a ~1 MHz frequency resolution through
spin lifetime measurements and characterizing spin-wave amplitudes by measuring the
NV spin rotation rate [58]. Recently, NV magnetometry has been used to study domain-
wall-guided spin-wave modes[54], magnon scattering[74, 117, 154], spin chemical po-
tentials[79], and frequency combs[168]. To enable sensitivity to target spin-wavelengths,
accurate control of the NV-sample distance is crucial because the spin-wave stray fields
depend exponentially on the distance to the sample at a length scale set by their wave-
length.

6.1. IMAGING NANOSCALE BACKWARD-VOLUME SPIN WAVES

Here, we demonstrate that controlling the NV-sample distance using a diamond tip moun-
ted on an atomic force microscope (Fig. 6.1a) creates a tunable wavelength filter that en-
ables selective probing of frequency-degenerate spin-wave modes. Increasing the NV-
sample distance progressively filters out small-wavelength spin waves, enabling studies
of long-wavelength modes that are otherwise hidden in thermal spin-wave noise. We
demonstrate high-contrast imaging over a range of wavelengths by adjusting the NV-
sample distance on the nanoscale. When maximizing the wavenumber-cutoff of our
distance-tunable filter via in-contact scans, we find a surprising pattern of standing spin
waves instead of the expected travelling waves. Fourier transforms of the patterns re-
veal an occupation of spin-wave modes along the entire isofrequency contour of the
two-dimensional spin-wave dispersion despite our one-dimensional stripline geome-
try, which we attribute to spin-wave scattering. Within this ensemble, we clearly identify
spin waves with wavelengths of only 360±20 nm. These results show that the exponential
decay of the spin-wave stray fields provides a resource unique to magnetic-resonance
spin-wave imaging, enabling wavenumber-selective detection of frequency-degenerate
spin waves and high-resolution imaging of spin-wave scattering.

Our system consists of a thin film of yttrium iron garnet (YIG), a magnetic insulator with
ultra-low spin-wave damping[10]. We excite spin waves by applying a microwave cur-
rent to a stripline that is microfabricated onto the YIG surface (Fig. 6.1a; SI Notes 6.6.1-
6.6.3). We apply a bias field B_0 along the NV axis to tune the NV electron spin resonance
(ESR) frequencies ($f_\pm$) relative to the spin-wave band. The orientation of B_0 magnetizes
the film in-plane and perpendicularly to the stripline, enabling efficient excitation of

'backward-volume' spin waves[10] that travel parallel to the magnetization (Fig. 6.1b, SI Notes 6.6.4-6.6.5). The spin waves generate magnetic stray fields above the surface that drive our NV spin when resonant with an NV ESR frequency. We detect these NV-resonant spin waves via the NV centre's spin-dependent photoluminescence (PL)[158].

We start by providing an overview of the NV PL as a function of the frequency of the microwave current applied to the stripline and the bias field B_0 (Fig. 6.1c). We do so with the diamond tip in contact with the YIG at ~ 30 μm from the stripline. We observe several regions of reduced PL caused by NV spin transitions that provide a first insight into the spin waves excited by the stripline:
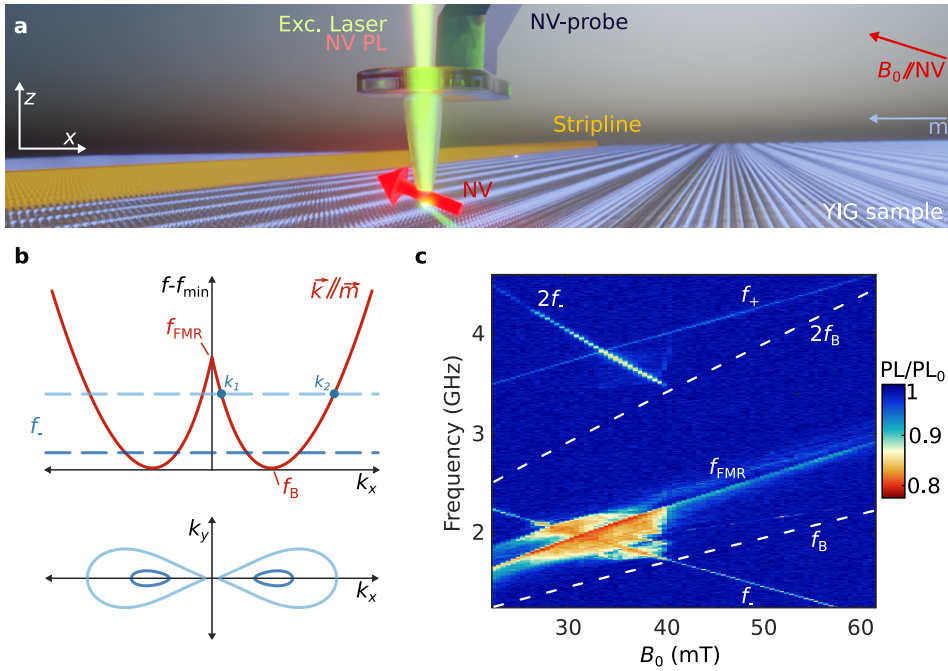
Figure 6.1: Imaging stripline-driven spin waves using scanning nitrogen-vacancy (NV) magnetometry. (a) A single NV spin embedded ~ 20 nm from the apex of a diamond tip (SI Note 6.6.2) measures the magnetic stray fields of spin waves excited by a microwave stripline in a 235 nm-thick yttrium iron garnet (YIG) film. The NV spin is initialized using a green laser and read out via its spin-dependent photoluminescence (PL). A bias magnetic field B_0 is applied along the NV axis, magnetizing the film perpendicularly to the 1 mm-long, 15 μm-wide stripline. (b) Top: Calculated dispersion of spin waves travelling parallel to the YIG magnetization ('backward-volume' spin waves). The NV spin detects spin waves at its electron spin resonance (ESR) frequency, f_-, indicated by dashed lines for two values of B_0 (darker colour corresponds to a larger B_0). In this work, we focus on spin waves resonant with f_- in the range $f_B < f_- < f_{FMR}$ for which there exist two frequency-degenerate backward-volume modes, k_1 and k_2. Bottom: iso-frequency contours of the two-dimensional spin-wave dispersion at the frequencies indicated by the dashed lines in the top panel. (c) NV photoluminescence as a function of B_0 and the microwave drive frequency. Data taken with the NV tip in contact with the YIG at ~ 30 μm from the stripline edge at 1 mW drive power. The NV photoluminescence under microwave excitation (PL) is normalized to the NV photoluminescence without microwave excitation (PL$_0$). The ESR frequencies ($f_\pm$) and calculated FMR frequency f_{FMR} are labelled. The dashed lines indicate the calculated minimum spin-wave frequency f_B and its harmonic at $2f_B$.

First, two lines of reduced PL occur when the drive frequency is resonant with the NV ESR frequencies f_- and f_+. Here, the NV spin is driven by the sum of the direct stripline field and the stray field of spin waves excited by the stripline[58, 169]. Second, a line of reduced PL reveals the YIG ferromagnetic resonance (FMR). Here, FMR-induced magnon-magnon scattering leads to spin-wave noise at the NV frequencies that causes NV spin relaxation and an associated PL reduction[79, 154]. Third, we observe a broad region of reduced PL when f_- is in the vicinity of the FMR. In this region, the stripline efficiently excites spin waves because of their micron-scale wavelengths near the FMR (SI Note 6.6.5). These spin waves in turn scatter efficiently to modes resonant with f_- because they are close in frequency and wavelength[170], causing NV spin relaxation. Correspondingly, the region of reduced PL ends abruptly when f_- drops below the bottom of the spin-wave band (labeled f_B in Fig. 6.1c) at $B_0 \approx 41\,\mathrm{mT}$. In this work, we study spin waves in the region $f_B < f_- < f_{FMR}$ and use the nanoscale control of the NV tip as a wavelength filter to separate the contributions from frequency-degenerate incoherent and coherent spin waves.
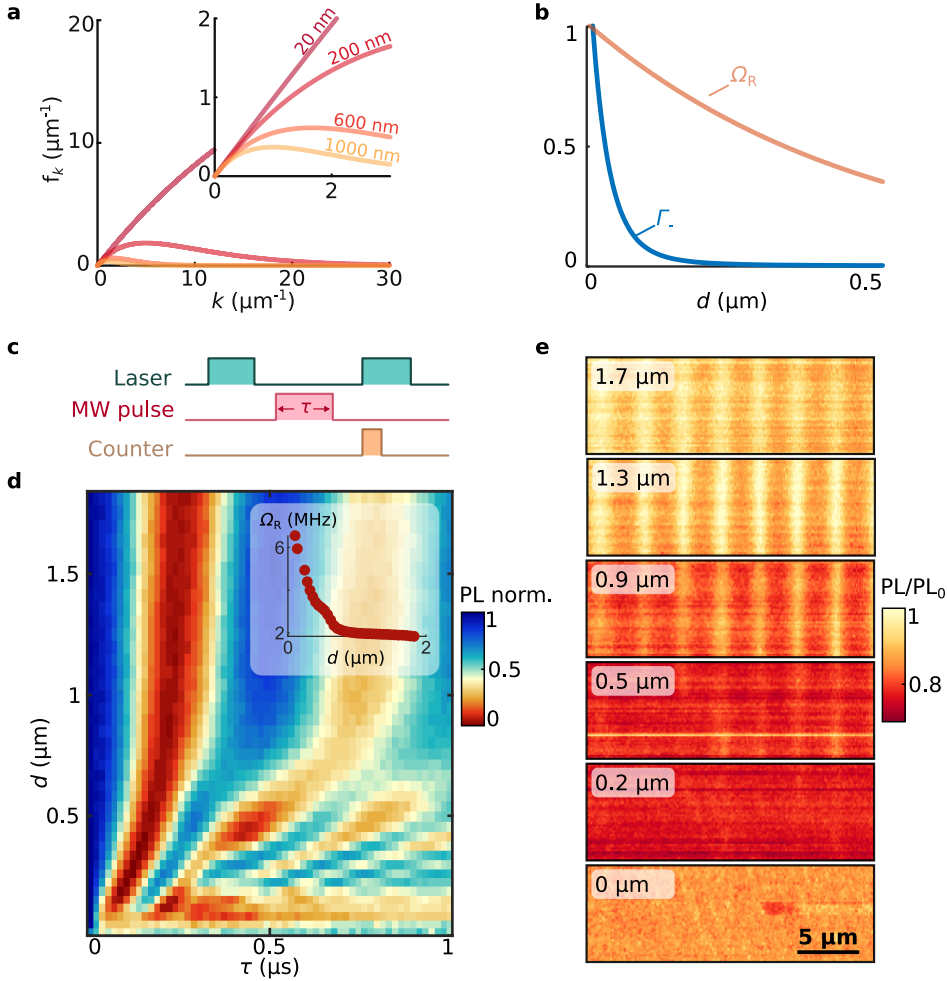
6.2. THE NV-SAMPLE DISTANCE AS A WAVELENGTH FILTER

Spin waves generate a rotating magnetic stray field with amplitude B_{SW} that decays with increasing distance d to the sample[73], with the decay length set by the spin-wavenumber k according to:

$$B_{SW} \propto f_k = k e^{-kd} \tag{6.1}$$

where f_k is the filter function (Fig. 6.2a,b). As such, increasing the NV-sample distance progressively filters out the stray fields of high-wavenumber spin waves. We demonstrate the filtering by characterizing the stray fields of spin waves excited by the microwave stripline as a function of the NV-sample distance. We do so by measuring the NV spin rotation rate (Rabi frequency), which depends linearly on the amplitude of the NV-resonant microwave field. We measure the Rabi frequency by tuning the NV frequency f_- to the iso-frequency contour of Fig. 6.1b and applying variable-duration microwave pulses. These pulses excite f_--resonant spin waves that drive NV spin rotations via their magnetic stray field[109].

With the tip in contact with the YIG (Fig. 6.2d, $d = 0\,\mathrm{nm}$), we observe fast NV spin decoherence, indicating a strong presence of incoherent spin-wave noise. As further shown below, the noise is caused by a combination of thermal and microwave-excited spin wave modes. By lifting the NV a few hundreds of nanometres, we suppress the noise sufficiently and start observing NV Rabi oscillations, indicating a coherent microwave field at the NV frequency. The non-exponential decrease of the Rabi frequency with a further increasing d (Fig. 6.2d and its inset) shows that the Rabi oscillations are driven by an ensemble of coherent spin waves of which the high wavenumbers are progressively suppressed by the distance-dependent cutoff of the filter. The microwave magnetic field generated by the stripline, which is approximately constant over the $\sim 2\,\mu\mathrm{m}$ lift-height range given the $\sim 30\,\mu\mathrm{m}$ distance to the stripline edge, sets the Rabi frequency at large d.

Figure 6.2: Tuning the NV-sample distance as a filter to selectively image a long-wavelength spin-wave mode. (a) The spin-wave stray field is proportional to a prefactor f_k (filter function) that depends on the NV-sample distance d (Eq. 6.1). The filter function peaks at $k = 1/d$, where k is the spin-wavenumber. The filter function is plotted for several values of d. (b) Calculation comparing the NV relaxation rate Γ_- caused by thermal spin waves to the NV Rabi oscillation rate caused by a coherently driven spin wave. Both rates are normalized to their value at $d = 0$ to highlight the different scaling with distance. The calculation of Γ_- assumes an equal population of all spin-wave modes at frequency f_- as expected for a Rayleigh-Jeans distribution[73]. The calculation of Ω_R assumes only a single spin-wave mode with wavenumber $k = 2\,\mu m^{-1}$ (as imaged in e) is excited. (c) Pulse sequence used for the measurement in (d): A 2.5 μs green laser pulse initializes the NV spin. A variable-duration microwave (MW)-pulse excites spin waves. The final NV spin state is read out by measuring the NV photoluminescence during the first 600 ns of a second green laser pulse. (d) Spin-wave-driven NV spin dynamics vs tip-sample distance d. The dynamics are governed by the stray-field spectrum of the spin waves at the NV frequency. For $d \gtrsim 100$ nm, the stray field of a coherent spin wave yields high-visibility Rabi oscillations with a long decay time. Below ~ 100 nm, the Rabi decay time starts to vanish, attributed to the more rapidly increasing stray field generated by thermal spin waves (see b). Measurement taken at 31 μm from the stripline edge at $B_0 = 32$ mT, $f_- = 1.98$ GHz and $P_{MW} = 6.3$ mW. Inset: Fitted Rabi frequency vs d down to 100 nm. (e) Spatial maps of the ESR contrast while driving spin waves at $f_- = 1.89$ GHz and $B_0 = 35$ mT ($k_1 = 1.7\,\mu m^{-1}$ and $k_2 = 22\,\mu m^{-1}$) at $P_{MW} = 1$ mW for varying d. The ESR contrast is obtained by normalizing the NV photoluminescence under microwave excitation (PL) to that without microwave excitation (PL$_0$).

Using spatial maps of the ESR contrast (Fig. 6.2e), we demonstrate that the distance-tunable filter enables spatial imaging of a single low-k spin wave within an ensemble of frequency-degenerate spin-wave modes. We define the contrast C by the ratio of the NV PL with and without microwave drive ($C = 1 - \mathrm{PL}/\mathrm{PL}_0$). The spatial contrast arises due to the interference between the field of the excited spin waves (which are propagating) and the uniform reference field that is supplied by our stripline[58, 169]. The in-contact scan (bottom panel Fig. 6.2e) shows two important features: first, the maximum contrast, $C_{\max}(d = 0) = 0.15$, is reduced with respect to the maximum contrast at increased distances $C_{\max}(d > 200\,\mathrm{nm}) = 0.25$. Second, the contrast equals its maximum value throughout the scan (i.e., it is saturated). The reduced ESR contrast of the in-contact scan is consistent with the strong increase of the stray field generated by thermally excited spin waves (Fig. 6.2b) that enhance the NV-spin relaxation rate[73, 79, 85, 128, 171] (SI Note 6.6.6) and lead to PL reduction[33, 104]. The spatially homogeneous saturation indicates a large amplitude of the microwave-driven spin waves, as we will show in more detail below.

Retracting the tip to $d = 0.2\,\mu\mathrm{m}$, we find that the contrast approximately doubles with respect to $d = 0\,\mu\mathrm{m}$. This is expected from the rapid suppression of the thermal spin-wave stray fields by our filter. However, we still find that the contrast is saturated over the entire spatial map (Fig. 6.2e) due to the large stray fields of spin waves excited by the microwave drive. For distances $d > 1\,\mu\mathrm{m}$, the microwave-driven spin waves are filtered to an extent that yields a clear spatial image of a single low-k spin-wave mode (Fig. 6.2e). These results show how lifting the tip from the surface filters out high-k spin waves, enabling high-contrast imaging of a single low-k spin wave within an ensemble of thermal and coherent spin-wave modes.

6.3. HIGH-CONTRAST SPIN-WAVE IMAGING

Fast NV-imaging of spin waves requires a strong ESR contrast. Because the spin-wave stray field falls off exponentially (Eq. 6.1), maintaining a strong contrast requires adapting the NV-sample distance to the expected spin-wavelength (Fig. 6.3a). We change the wavelength of the mode, indicated by k_1 in figure 6.1b, by increasing B_0 while reducing the drive frequency according to $f_- = D - \gamma B_0$ to maintain resonance with the NV, where $D = 2.87\,\mathrm{GHz}$ is the NV zero-field splitting and $\gamma = 28\,\mathrm{GHz\,T^{-1}}$ is the electron gyromagnetic ratio. Starting from the distance used in figure 6.2c for $B_0 = 35\,\mathrm{mT}$, we find that keeping $kd = constant$ yields high-contrast images over a range of wavelengths (Fig. 6.3b). The spatial images of figure 6.3b show how the wavelength decreases with increasing B_0 until the f_- detection frequency drops below the bottom of the spin-wave band at $B_0 \approx 41\,\mathrm{mT}$ (inset Fig. 6.3c). At this field ($B_0 = 41\,\mathrm{mT}$), both modes (labeled k_1 and k_2 in Fig.6.1) are expected to contribute to the interference pattern. However, due to the low signal-to-noise, we cannot conclusively identify both modes (SI Note 6.6.7). The large ESR contrast at the other fields enables a straightforward extraction of the wavelengths (SI Note 6.6.7), which correspond well with the calculated spin-wave dispersion (Fig. 6.3c).
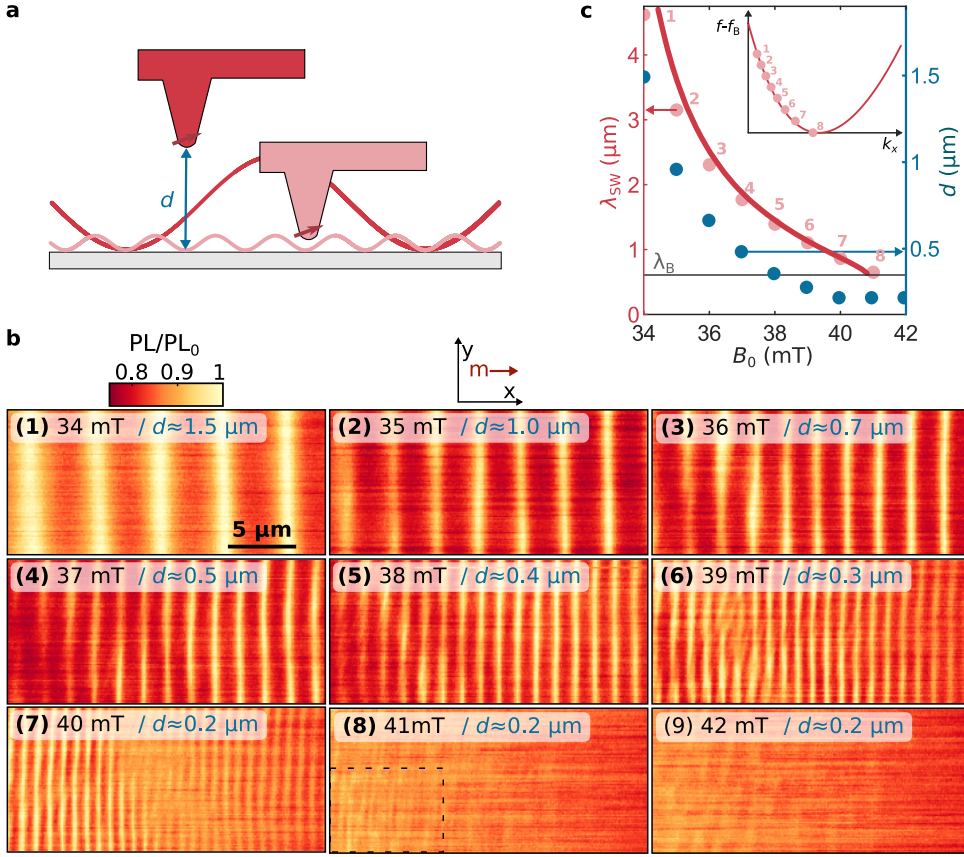
Figure 6.3: Adapting the sensor-to-sample distance to realize high-contrast imaging of different spin-wavelengths. (a) Spin waves generate a magnetic stray field that decays exponentially at the scale of the spin-wavelength. We tune the tip-sample distance d to optimize the detection of different wavelengths. (b) Spatial maps of the NV ESR contrast showing backward-volume spin waves excited by the stripline at different magnetic fields B_0. Increasing B_0 (panels 1-8) decreases the wavelength of the spin waves that are resonant with the NV ESR frequency. In each scan, we tune the distance d to maintain a constant ESR contrast, as plotted in c. In panel 8, we extract the wavelength by analyzing the dashed box. Drive power $P_{MW} = 4\,\text{mW}$. (c) The wavelengths extracted by fitting (SI Note 6.6.7) the wave patterns in b (pink dots) compared to the wavelengths calculated from the backward-volume dispersion (plotted in red, SI Note 6.6.4), as a function of B_0. The wavelength at the minimum of the spin-wave band is indicated by λ_B. Blue dots(right y-axis): The tip-sample distance d used in each of the scans shown in b. Inset, red line: calculated dispersion of the backward-volume spin waves relative to the minimum spin-wave frequency. Pink dots: modes imaged in b.

## 6.4. NANOSCALE IMAGING OF FREQUENCY-DEGENERATE SPIN WAVES

Bringing the NV-tip into contact with the sample maximizes the wavenumber cutoff of our filter and increases the relative contribution of high-wavenumber modes to the stray field (Fig. 6.2a). We use in-contact scans to study the ensemble of spin-wave modes excited in the magnetic film. To avoid the spatially homogeneous saturation of the NV

ESR contrast observed for the in-contact scan of figure 6.2e, we reduce the microwave drive power by a factor 500. This reduction yields smaller amplitudes of the microwave-excited spin waves, which prevents saturation of the NV ESR contrast and thereby re-establishes the ability of the ESR contrast to be modulated by spatial changes in the spin-wave stray fields. The resulting spatial modulations of the ESR contrast reveal a rich pattern of spin waves in different directions (Fig. 6.4a).

To interpret the wavenumber content of the spin-wave patterns observed in figure 6.4a, we perform a Fourier transform. The Fourier maps reveal the excitation of spin-wave modes along the entire f_--isofrequency contour of the two-dimensional spin-wave dispersion (Fig. 6.4b). We observe spectral content at wavenumbers up to $k \approx 25 \mu m^{-1}$. The peaks at $k \approx 17 \mu m^{-1}$ (right panel, Fig. 6.4b) correspond to spin-wavelengths of $\approx 360 nm$ that are also clearly visible in the real-space images (right panel, Fig. 6.4). Although these modes are not directly excited by our microstrip, such a homogeneous occupation of the spin-wave dispersion may be expected when taking into account scattering of the primarily excited backward-volume spin waves[172] enhanced by the presence of defects, such as small scratches and small pits that are homogeneously present in our liquid-phase-epitaxy-grown YIG film (SI Note 6.6.8). Previous works[173–178] demonstrated that such defects act as spin-wave scatterers and lead to the occupation of high-k modes.

6
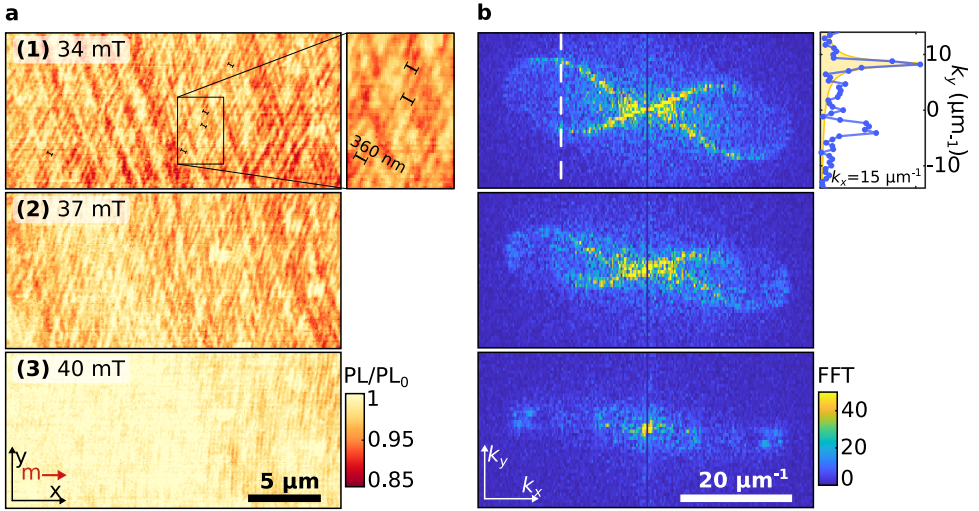
Figure 6.4: Emergence of frequency-degenerate standing spin-wave modes in spatial maps of the ESR contrast. (a) Measured ESR contrast when the tip is in contact with the sample at low drive power (6.3 μW) for different magnetic bias fields B_0. Right panel: zoom-in of 1 with 360 nm spin waves. (b) Absolute value of the Fourier transformations (FFT) of the maps in (a), revealing the wavevectors present in the spatial spin-wave patterns. The full isofrequency contour of the spin-wave dispersion is visible at $B_0 = 34 mT$. Right panel: line-trace at $k_x = 15 \mu m^{-1}$ (white dashed line). The fitted peak (yellow) corresponds to $k_y = 8.3 \mu m^{-1}$, yielding $k = 17 \mu m^{-1}$ and $\phi_k = 29°$. The corresponding wavelength of $360 \pm 20 nm$ (uncertainty derived from the fitted peak width) is clearly visible in the zoomed-in real-space image presented in 1 (black bars).

The absence of ESR contrast for $B_0 > 40\,\text{mT}$ (at which the NV frequency sits below f_B; SI Note 6.6.9) shows that the amplitude of the direct stripline field is too small to generate ESR contrast. We, therefore, conclude that the stray-field patterns observed at $B_0 < 40\,\text{mT}$ do not result from interference between the spin-wave and stripline fields but are instead generated by standing spin waves that result from scattering. These results highlight the coherent nature of the scattering process and the efficiency by which it leads to the occupation of high-momentum modes that are otherwise inaccessible to a one-dimensional excitation stripline.

6.5. CONCLUSIONS

Nanoscale control of the NV-sample distance serves as a tunable filter that enables balancing the magnetic fields generated by an ensemble of incoherent and coherently driven spin waves of different wavelengths. This control enables selective imaging of a coherent spin-wave mode within a mixture of frequency-degenerate spin waves and retaining a high-visibility response when imaging different wavelengths. In-contact scans at reduced drive power show a surprising pattern of standing spin-wave modes. The Fourier transforms of these patterns reveal spin-wave occupation along the entire isofrequency contour of the two-dimensional spin-wave dispersion. We attribute the occupation of these high-momentum modes to defect-enhanced spin-wave scattering. The phase relation between the scattered modes is maintained, emphasizing the coherent nature of the scattering process. Nanoscale control of the NV-sample distance and wave-number-selective imaging of magnetic oscillations at microwave frequencies paves the way for imaging magnon condensates[16] or other coherent spin-wave modes[54] and could also be used to probe microwave electric current distributions in devices.

6.6. SUPPORTING INFORMATION

6.6.1. YIG SAMPLE

The ~ 235(10) nm thick yttrium iron garnet (YIG) was grown on a gadolinium gallium garnet (GGG) substrate by liquid-phase epitaxy (Matesy GmbH). The YIG chip was first

sonicated in acetone to remove contaminants. A 1 mm-long and 15 μm-wide stripline (5 nm titanium / 200 nm gold) for spin-wave excitation was then deposited on top of the YIG surface using *e*-beam evaporation preceded by *e*-beam lithography, using a double PMMA resist (A8 495K / A3 950K) and a top layer of Elektra92.

6.6.2. MEASUREMENT SETUP

Our scanning NV-magnetometry setup consists of two stacks of Attocube positioners (ANPx51/RES/LT) and scanners (ANSxy50/LT and ANSz50/LT) that enable individual positioning of the tip and sample, in addition to a confocal microscope setup, which are all placed in an acoustic enclosure. The confocal setup uses a 515 nm green laser (Cobolt 06-MLD, pigtailed) for NV excitation, which is focused by the objective lens (LT-APO/VISIR/0.82) onto a single-NV tip ((001)-oriented, QZabre Ltd). The NV was created via nitrogen implantation with an implantation energy of 7 keV. This energy leads to an expected implantation depth of about (10 ± 10) nm (see, e.g. Ref. [179]). Taking into account a possible selection of relatively deep NVs because of photoluminescence properties, we conservatively estimate an NV-depth of 20 nm below the tip surface. The NV photoluminescence (PL) is collected by the same objective and separated from the excitation laser by a dichroic mirror (Semrock Di03-R532-t3-25x36) and a long-pass filter (Semrock BLP01-594R-25), spatially filtered by a pinhole (50 μm), and finally collected by an avalanche photodiode (APD) (Excelitas SPCM-AQRH-13). A SynthHD (v2) microwave generator (Windfreak Technologies, LLC) was used to apply microwave signals. A programmable pulse generator (SpinCore Technologies, Inc. PulseBlasterESR-PRO 500) controls the timing of the laser excitation, detection window and microwaves. A National Instruments card (PCIe 6323) was used for the data acquisition.

6.6.3. SPIN-WAVE MEASUREMENT METHODS

All measurements were performed close to the middle of the 1 mm-long stripline to prevent edge effects from stripline corners, within 30 μm from the edge of the 15 μm-wide stripline. The direct stripline field interferes with the spin-wave field to form the standing-wave stray-field patterns of figures 2 and 3 (main text) [58, 169]. The static field B_0 is applied by moving a small permanent magnet mounted on translation stages. For all measurements, the magnet is aligned along the NV axis within $\sim 5°$ such that the expected angle between the NV and the sample is $\theta \approx 54°$ with respect to the sample-plane normal. Because of some uncertainty introduced when mounting the NV-probe, we leave this angle as a free parameter when fitting the measured wavelength to the spin-wave dispersion, yielding $\theta = 49°$ (Fig. 3d). For the scans at non-zero tip-sample distances in figures 2 and 3 (main text), we first touch down onto the sample with the tip to acquire a well-defined distance reference. Then, we turn off the AFM feedback and set the lift height using our piezo scanner (SI Note 6.6.10). We repeat this for each line trace. As there is no feedback, the lift height can change over a line trace due to drift or sample tilt.

6.6.4. SPIN-WAVE DISPERSION

Here, we calculate the spin-wave dispersion of our 235 nm film of yttrium iron garnet (YIG). We assume a 2D geometry, where the magnetization does not change across the

film thickness (Fig. 6.5). We first consider the relevant energy contributions for our magnetic system to evaluate the Landau-Liftshitz-Gilbert (LLG) equation that describes the dynamics of the magnetization. Following the approach described by Rustagi *et. al*[73], we then obtain the magnetic susceptibility and the spin-wave dispersion (section 6.6.4).

a

b
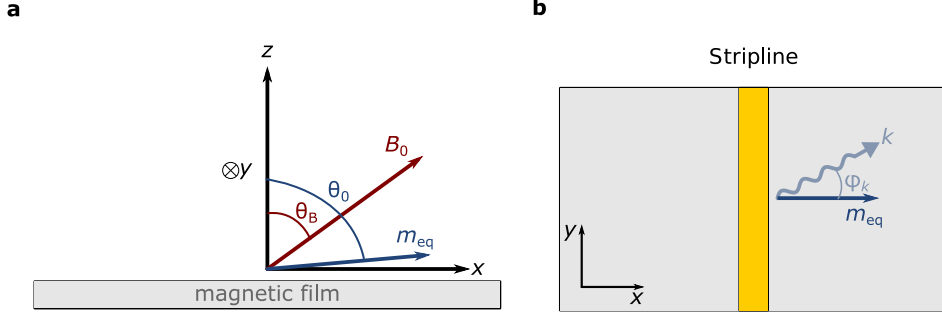
Figure 6.5: Schematic of the measurement geometry. (a) Side view of our measurement geometry. The magnetic field is applied at an angle θ_B with respect to the sample normal. As a result, the equilibrium magnetization $\vec{m}_{eq}$ tilts slightly out-of-plane with an angle θ_0. (b) Top view of the measurement geometry. We drive the transverse magnetization via an oscillating magnetic field supplied by a microwave current that is sent through a microstrip with width 15 μm and length 1 mm. In this work, the stripline field excites spin waves that travel parallel to the equilibrium magnetization, also called backward-volume spin waves. The parameters used for calculating the spin-wave dispersion for the film studied in this work are $M_s = 1.42 \cdot 10^5$ A/m, $A_{ex} = 3.8 \cdot 10^{-12}$ J/m, $\alpha = 1 \cdot 10^{-4}$ and $L = 235$ nm [58]. The angle between the magnetic field and the film, θ_B is $\theta_B \approx \theta_{NV} \approx 54°$.

MAGNETIC SUSCEPTIBILITY

Given that the Zeeman interaction, the demagnetizing field and the exchange interaction are the relevant energy contributions, we calculate the response of the transverse magnetization $\delta\vec{m}'_\perp$ to a drive field $\vec{h}_\perp(\vec{k})$ via $\delta\vec{m}'_\perp = S\vec{h}_\perp$. Here, $\delta\vec{m}'$ is defined in the magnet frame, where the equilibrium magnetization ($\vec{m}_{eq}$) points in the z-direction. And S is the transverse magnetic susceptibility, which is given by [73]:

$$S(\vec{k},\omega) = \frac{\gamma}{\Lambda} \begin{bmatrix} \omega_3 - i\alpha\omega & -\omega_1 - i\omega \\ -\omega_1 + i\omega & \omega_2 - i\alpha\omega \end{bmatrix} \tag{6.2}$$

where

$$\omega_0(\vec{k}) = \omega_B \cos(\theta_B - \theta_0) - \omega_M \cos^2\theta_0 + \omega_D k^2 \tag{6.3}$$

$$\omega_1(\vec{k}) = \omega_M f_L \sin\phi_k \cos\phi_k \cos\theta_0, \tag{6.4}$$

$$\omega_2(\vec{k}) = \omega_0 + \omega_M \left[f_L \cos^2\phi_k \cos^2\theta_0 + (1 - f_L)\sin^2\theta_0 \right] \tag{6.5}$$

$$\omega_3(\vec{k}) = \omega_0 + \omega_M f_L \sin^2\phi_k \tag{6.6}$$

$$\Lambda(\omega) = (\omega_2 - i\alpha\omega)(\omega_3 - i\alpha\omega) - \omega_1^2 - \omega^2 \tag{6.7}$$

Here, $\omega_B = \gamma B_0$, is the frequency associated with the Zeeman energy, where γ is the gyromagnetic ratio and B_0 the externally applied magnetic field. We apply B_0 at an angle

θ_B, which is the direction of the magnetic field with respect to the sample normal, such that it aligns with the NV centre. As a result, the equilibrium magnetization θ_0 tilts out-of-plane by an angle θ_0. Next, the frequency associated with the demagnetizing field is given by: $\omega_M = \gamma \mu_0 M_s$, where μ_0 and M_s are the vacuum permeability and the saturation magnetization, respectively. Finally, $\omega_D = \frac{\gamma D}{M_s}$ is associated with the exchange interaction, where D is the spin stiffness[i]. A wave vector, $\vec{k}$ is described by its wavenumber k (i.e. the modulus of the wave vector) and by its direction, which is described by ϕ_k. Finally, the prefactor f_L is given by $f_L \equiv 1 - (1 - e^{-kL})/(kL)$ in which L is the film thickness.

EQUILIBRIUM MAGNETIZATION

The equilibrium angle of the magnetization, θ_0, follows from minimizing the free energy and solving for each value of the magnetic field:

$$-2B_0 \sin(\theta_B - \theta_0) = \mu_0 M_s \sin(2\theta_0) \tag{6.8}$$

We calculate that θ_0 is in-plane to within a few degrees for the magnetic fields used in our measurements.

SPIN-WAVE DISPERSION

The spin-wave dispersion is given by the frequencies for which the susceptibility is singular, i.e. when: $\Lambda = 0$ (Fig. 6.6). By tuning the external magnetic field, we vary f_- with respect to the minimum spin-wave frequency. As such, the contour (dashed line in Fig. 6.6) changes shape such that f_- becomes resonant with spin waves of different wavevectors.
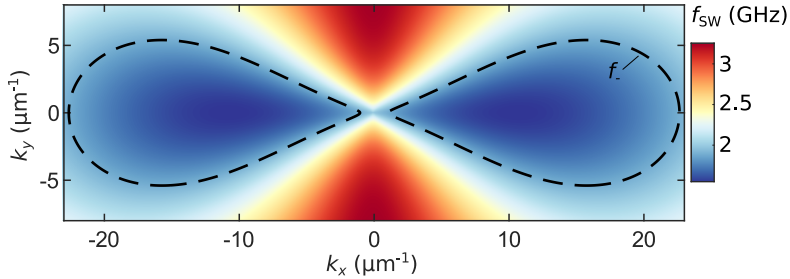
Figure 6.6: Spin-wave dispersion. Calculated spin-wave dispersion for $B_0 = 35$ mT, i.e. when $f_B < f_- < f_{FMR}$. The field is aligned along the NV-axis such that $f_- = 1.89$ GHz, which is represented by the iso-frequency contour (dashed line).

6.6.5. STRIPLINE FIELD

We use a stripline oriented along y, with width w, length L and thickness h for spin-wave excitation, centred at $x = 0$ and $z = -h/2$. A microwave current density $J(\omega)$ applied to

---

[i]The spin stiffness is often expressed in terms of the exchange constant A with more conventional units (J/m): $D = 2\gamma A_{ex}/M_s$ (with units (rad/s/m^2))

the stripline generates a magnetic field with components [58]:

$$h_x = 2J(\omega)e^{kz}\frac{e^{-kh}-1}{kk_x}\sin\left(k_x\frac{w}{2}\right)\frac{\sin\left(k_y\frac{L}{2}\right)}{k_{y(x)}} \qquad (6.9)$$

$$h_z = -2iJ(\omega)e^{kz}\frac{e^{-kh}-1}{k^2}\sin\left(k_x\frac{w}{2}\right)\frac{\sin\left(k_y\frac{L}{2}\right)}{k_y} \qquad (6.10)$$

$$(6.11)$$

in k-space. Because the film is magnetized along x, the x-component of the field does not contribute to spin-wave excitation. As such, we only consider the $z-$component. The field exciting the spin waves is obtained by averaging over the film thickness:

$$\tilde{h}_z = -2iJ(\omega)\frac{e^{-kL}-1}{kL}\frac{e^{-kh}-1}{k^2}\sin\left(k_x\frac{w}{2}\right)\frac{\sin\left(k_y\frac{L}{2}\right)}{k_y} \qquad (6.12)$$

Because the length of the stripline far exceeds its width and the distance between the stripline center and our measurement location, it is essentially a one-dimensional stripline that does not excite spin waves in the k_y direction (Fig. 6.7).
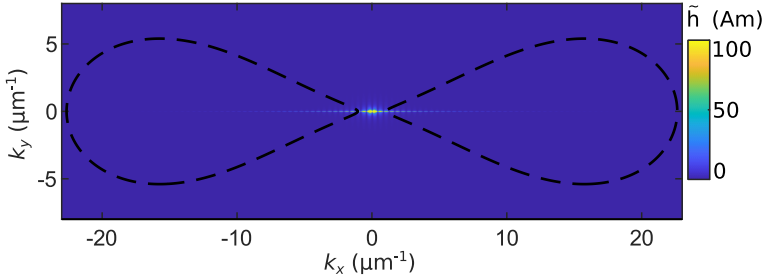
Figure 6.7: The effective field strength for a stripline that is aligned perpendicular to the magnetization (backward-volume geometry). Using a 15 μm-wide and 1 mm-long stripline. The stripline field is most efficient in driving low-wavenumber modes (close to the FMR). Due to its one-dimensional character, spin waves with a component in the k_y direction are not excited. Dashed line indicates the f_--isofrequency contour (Fig. 6.6) of NV resonant modes at 35 mT.

6.6.6. NV RELAXATION INDUCED BY THERMAL MAGNONS
We follow the approach of Rustagi *et al.*[73] to calculate the NV relaxation rates induced by the magnons in our YIG film (Fig. 2d, main text) using:

$$\Gamma_\mp(\omega_\mp) = \frac{\gamma^2}{2}\int\frac{d\vec{k}}{(2\pi)^2}\sum_{i,j\in\{x,y\}}\mathscr{D}_{\pm i}^{\text{eff}}(\vec{k})\mathscr{D}_{\mp j}^{\text{eff}}(-\vec{k})C_{ij}(\vec{k},\omega_\mp) \qquad (6.13)$$

Here, $\Gamma_\mp$ are the relaxation rates corresponding to the $\omega_\mp$ ESR frequencies, $\vec{k}$ is the spin-wavevector, $\mathscr{C}$ is a spin-spin correlator describing the thermal magnon fluctuations, and $\mathscr{D}^{\text{eff}}$ is a dipolar tensor that calculates the magnetic stray fields that induce NV spin relaxation generated by these fluctuations. Note, this equation is defined in the magnet frame, for which the equilibrium magnetization is along the z-direction.

The thermal transverse spin fluctuations in the film are described by [73]:

$$C_{ij}(\vec{k},\omega) = 2D_{th} \sum_{\nu=\{x,y\}} S_{i\nu}(\vec{k},\omega) S_{j\nu}(-\vec{k},-\omega) \tag{6.14}$$

where $D_{th} = \frac{\alpha k_B T}{\gamma M_s L}$, with k_B the Boltzmann constant, T the temperature, S the magnetic susceptibility (Eq. 6.2).

The dipolar tensor $D^{eff}(\vec{k},\omega)$ is obtained by first rotating the magnet frame to the lab frame, then multiplying by the dipolar tensor $\mathscr{D}(\vec{k})$ in the lab frame, and then rotating the result to the NV frame: $D^{eff}(\vec{k},\omega) = R_{yz}(\theta_{NV},\phi_{NV})\mathscr{D}(\vec{k})R_Y(\theta_0)^T$, where

$$\mathscr{D}(\vec{k}) = -\frac{\mu_0 M_s}{2} e^{-|\vec{k}|d_{NV}}(1 - e^{-|\vec{k}|L}) \begin{bmatrix} \cos^2\phi_k & \sin(2\phi_k)/2 & i\cos\phi_k \\ \sin(2\phi_k)/2 & \sin^2\phi_k & i\sin\phi_k \\ i\cos\phi_k & i\sin\phi_k & -1 \end{bmatrix} \tag{6.15}$$

where μ_0 is the vacuum permeability and d_{NV} is the distance between the NV and the sample surface. The terms in Eq. (6.13) that induce spin relaxation are given by[73]: $\mathscr{D}^{eff}_{\pm\nu} = \mathscr{D}^{eff}_{x\nu} \pm i\mathscr{D}^{eff}_{y\nu}$.

For a magnon gas in thermal equilibrium, in the absence of microwave driving, the dependence of the NV relaxation rate on the NV-sample distance can be calculated using Eq. (6.13). The fast increase in rate (Fig. 2d, main text) results in a reduction of the ESR contrast as the NV sensor approaches the film to within nanometre proximity.

6.6.7. Spatial ESR contrast generated by a single spin wave

Here, we determine the spatial profile of the ESR contrast generated by a propagating spin-wave mode, with wavenumber k that interferes with a uniform reference field of varying amplitude (Fig. 6.8)[58, 169]. We show that the ESR contrast spatially varies depending on the wavenumber, given that the reference field has a finite amplitude.
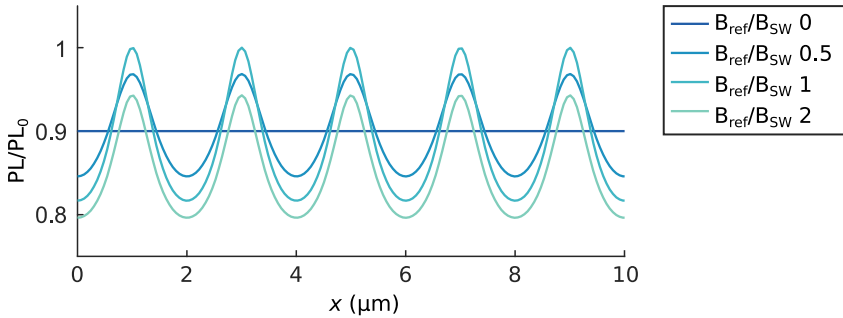
Figure 6.8: Spatial profile of a single spin wave mode interfering with a reference field. The expected PL/PL_0 for a single spin-wave mode for various strengths of the reference field.

Spin waves produce a field of which the component (B_{SW}) that is rotating with the correct handedness in a plane that is perpendicular to the NV-axis drives Rabi oscillations[58]. This component varies spatially according to:

$$B_{SW} = B_{SW}^0 e^{ik(x-x_0)} \tag{6.16}$$

This field induces NV Rabi oscillations, of which the rate is given by:

$$\Omega_R = \frac{\gamma}{\sqrt{2}}|B_{SW} + B_{ref}| \tag{6.17}$$

where B_{ref} is the component of the reference field that is rotating with the correct handedness in a plane perpendicular to the NV-axis. The ESR contrast is given by:

$$PL/PL_0 = 1 - C_{ESR} \tag{6.18}$$

$$PL/PL_0 = 1 - \beta\frac{\Omega_R^2}{\Omega_R^2 + \delta^2} \tag{6.19}$$

where β is a constant that describes the maximum ESR contrast and δ is a parameter that depends on the optical pumping rate[33], which we assume to be constant as all measurements were taken at the same laser power.

EXTRACTING THE SPIN WAVELENGTH OF THE LOW WAVENUMBER MODE

Here we analyze the spatial maps shown in figure 6.3b (main text) and extract the wavelength of the imaged modes.
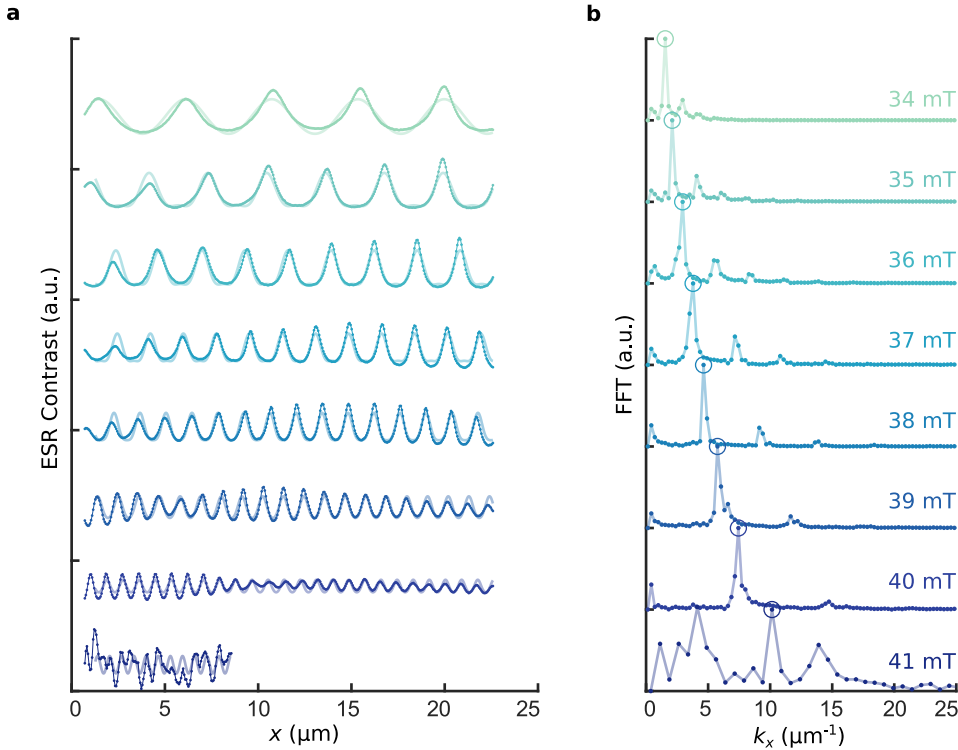
Figure 6.9: Wavelength analysis of spin-wave maps (a) We average the 2D maps of figure 3b (main text), to obtain a 1D linetrace of the ESR contrast as a function of x-position. We fit the data using equation 6.19, to obtain the wavenumber and its uncertainty. (b) Fourier transform of the 1D data shown in (a). Circles represent peak positions used as an initial guess for the fitting.

To do so, we first plot the signal as a function of x (Fig. 6.9a) after subtracting a linear term to account for the non-uniformity of the stripline-field. Using equation 6.19, we then fit the averaged data (Fig. 6.9a). The fit allows us to extract the wavenumber k, which we plot as a function of B_0 (Fig. 3c, main text). In figure 6.9b, we show the corresponding Fourier transform of the averaged data traces. Finally, we fit the extracted wavenumbers to the backward-volume spin-wave dispersion, and we find that an angle of $\theta_B = 49°$, which is the angle between the magnetic field and the YIG surface normal, fits our data best due to uncertainty in the mounting of the NV-probe with respect to the sample surface.

6.6.8. COMBINED ATOMIC FORCE MICROSCOPY AND PHOTOLUMINESCENCE SCANS OF THE YIG SURFACE

In contact mode, our scanning NV magnetometry setup collects both the topography, via the AFM feedback signal and the NV photoluminescence (Fig. 6.10). The topography image not only shows dirt particles laying on top of the surface (large white dot in the centre of the scan), but also scratches and tiny pits in the YIG surface that can lead to magnon scattering [174, 177, 178].
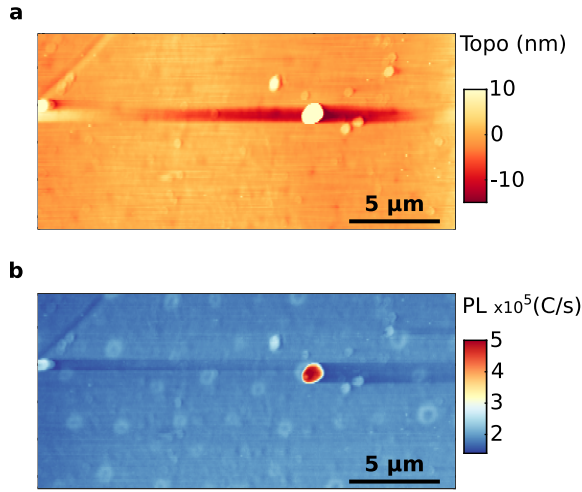
Figure 6.10: YIG surface. (a) Surface topography (Topo) where the arrows indicate several small defects and (b) photoluminescence (PL) of our 235 nm-thick YIG film surface. Data correspond to the ESR map in figure 6.11b, scan 1 taken with the tip in contact with the YIG surface.

6.6.9. OVERVIEW SPIN-WAVE IMAGES

a) Lift-mode scan

PL/PL$_0$ 0.75 1   FFT 0 100

b) Low-power contact-mode scans

PL/PL$_0$ 0.9 1   FFT 0 20 40
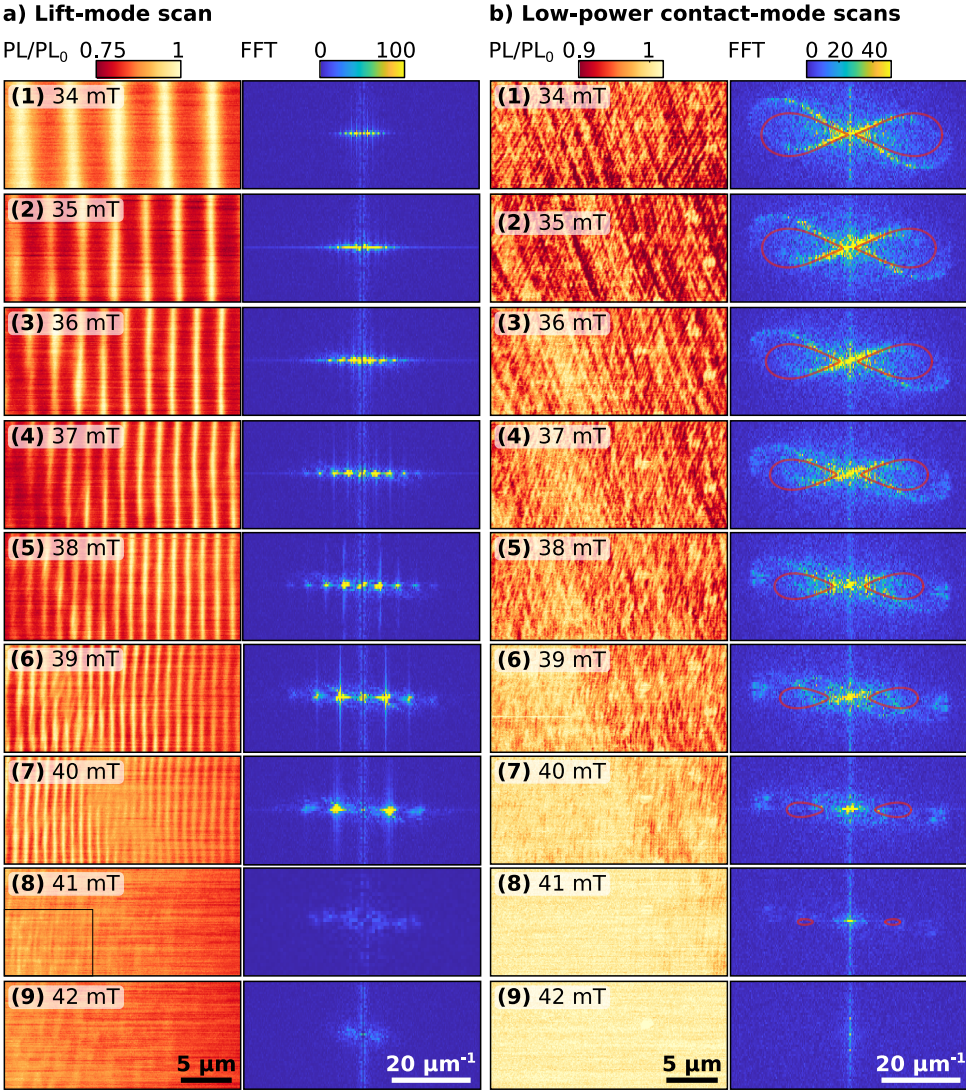
Figure 6.11: Overview spin-wave images (a) Scans corresponding to Fig. 3b of the main text using $P_{MW} = 4\,\text{mW}$ and we change the NV-to-sample depending on the spin-wavelength. (b) Scans corresponding to Fig. 4a of the main text using $P_{MW} = 6.3\,\mu\text{W}$ while keeping the NV-tip in contact with the magnetic surface. Red line: the calculated isofrequency contour of the 2D spin-wave dispersion.

6.6.10. Calibration of the piezoelectric scanners

Lateral displacement

Our piezoelectric scanner (ANSxy50/LT) exhibits a nonlinear motion as a function of applied voltage. We calibrate this non-linear motion using a silicon nitride sample with $2\,\mu$m chess pitch structures. Specifically, we scan over the same region of interest and piezo scanner voltages/offsets while recording the photoluminescence (Figure 6.12a). Our calibration procedure to convert the non-linear displacement as a function of the applied voltage to the position is as follows:

1. We first remove the first 25 lines from our scan data which show large non-linear and non-reproducible displacements depending on scan speed and time spent on the first pixel.

2. We assign the applied voltage to known positions of subsequent chess pitches (Fig. 6.12). For simplicity, we do this for a single row or column (Fig. 6.12b).

3. We fit a second-order polynomial to the known X or Y displacement.

We repeat this process for the two scan speeds used in this work: $0.1\,\mathrm{Vs}^{-1}$ and $0.05\,\mathrm{Vs}^{-1}$ used for the lift-mode and contact mode scans. We can now interpolate our 2D spatial scans, which were taken at linearly spaced voltage intervals and obtain a 2D image with linearly spaced position intervals. Note that all scan data shown in the manuscript are taken in the forward scan direction, and we, therefore, do not take piezoelectric hysteresis into account.
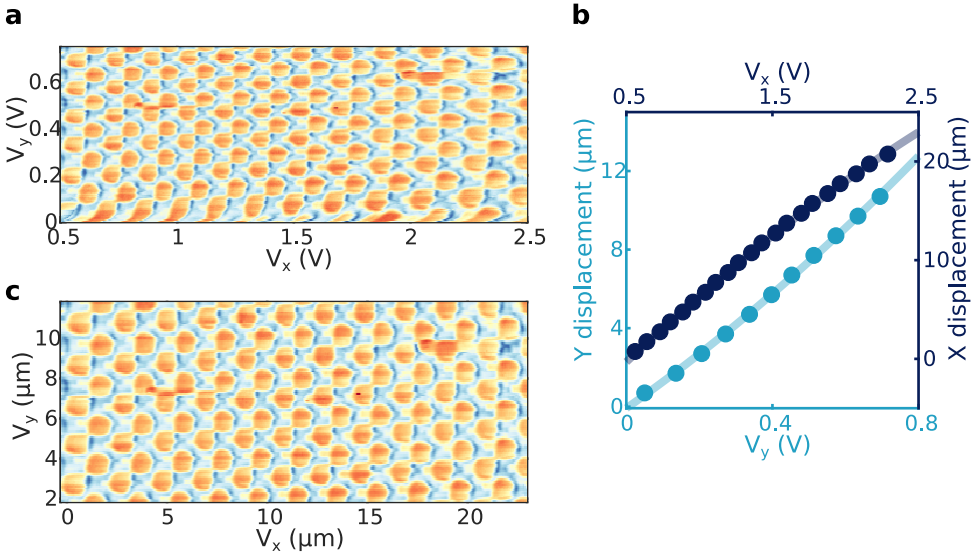
Figure 6.12: Calibration of lateral piezoelectric scanners. (a) 2D spatial scan of calibration sample with a $2\,\mu$m pitch using linearly spaced voltage intervals at a scan speed of $0.1\,\mathrm{Vs}^{-1}$. (b) We fit the known X and Y displacement of the chess pits (using a single row or column) as a function of applied X and Y voltage. (c) Interpolated data shown in (a), now using linearly spaced position intervals obtained by the fitting functions in (b) and with the first 25 scan lines removed

CALIBRATION OF THE NV-TO-SAMPLE DISTANCE

When retracting the NV-tip from the YIG surface, we observe oscillations in the NV PL (Fig. 6.13a). We assume that the oscillations are caused by interference between the YIG-surface-reflected laser light and the laser light internally reflected in the diamond tip (akin to the effect leading to Newton rings). The interference leads to PL oscillations with a spatial period equal to half the laser wavelength (i.e. 515 nm/2). We use these oscillations to estimate the tip-sample distance d for each setpoint distance obtained from the linear voltage-to-distance conversion provided by the supplier of the scanners (Fig. 6.13b) .
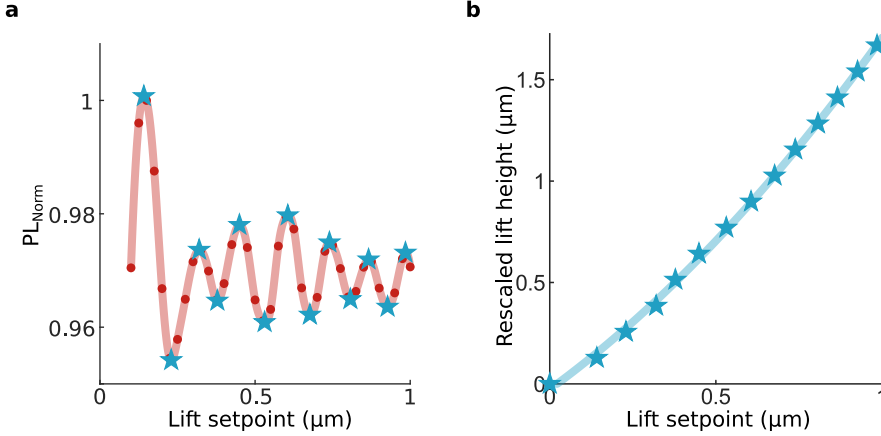
Figure 6.13: Calibration of lift height. (a) Oscillating PL signal when the tip is retracted from the YIG surface. The stars are the found extrema. Data correspond to the Rabi measurement shown in Fig. 2b of the main text. (b) We allocate a distance of $\lambda/4$ between each extremum (stars), of which the first maximum corresponds to an absolute distance of $\lambda/4$ from the surface. Our contact position is fixed at zero lift height. We use a second-order polynomial to fit the displacement (solid line).

7

CONCLUSIONS & OUTLOOK

M AGNETOMETERS have been essential for developing our understanding of the world around us: From magnetic compasses, the first magnetometers used for navigation[2, 3], to modern-day magnetic resonance imaging (MRI), which images the microscopic magnetic environment around nuclear spins[180].

In this thesis, we used a magnetometer based on the electron spin associated with diamond's nitrogen-vacancy (NV) centre. NV magnetometry is a versatile and sensitive magnetic imaging technique that we use to study the nanoscale magnetization oscillations in magnets caused by spin waves. Spin waves are the elementary excitations of magnetic materials, which are interesting because of their rich physics and potential role in low-dissipation information technology. In particular, we studied spin waves in a thin magnetic insulator called yttrium iron garnet (YIG), which is known for its low dissipation and represents a model magnet for studying spin waves[10].

NV magnetometry detects spin waves by their microwave magnetic stray fields [58]. These fields decay evanescently on the scale of the spin wavelength. As such, we used NV centres embedded in an atomic force microscope probe enabling nanometre NV-sample proximity and sensitivity to nanoscale spin waves.

This chapter concludes our work by highlighting our main results. Based on these results, we describe several new research directions in the outlook.

7.1. THESIS HIGHLIGHTS

In chapter 4, we described the nanofabrication of diamond for NV magnetometry and, particularly, for the in-house fabrication of all-diamond scanning NV probes. Our first generation of NV probes, consisting of a platform carrying a cylindrical pillar with a top diameter of $300 - 400\,\text{nm}$, was realized by implementing the methods developed by Refs.[52, 111]. Just below the pillar apex, we implanted an ensemble of NV centres. Such

probes provide NV-sample proximity, thereby ensuring sensitivity to fields that rapidly decay from the sample surface while also providing high photoluminescence (PL) rates and sensitivity to different field projections. In **chapter 5**, we benchmark the sensitivity of our probes by measuring the NV-sample distance-dependent sub-micron scale decay of the magnetic field noise produced by thermal spin waves in YIG. In addition, we could image the transport of coherent spin waves with wavelengths down to ~500 nm, which is near the imaging resolution of NV ensembles. Furthermore, while driving low-wavenumber coherent spin waves, we found a surprising unidirectional excitation of an out-of-equilibrium magnon gas that extended hundreds of micrometres from the excitation stripline. Such targeted delivery of high-density magnon gases can be used for controlling spin transport in specific directions.

The magnetic noise from incoherent spin waves makes NV-imaging of coherent spin waves at close NV-sample proximity challenging. In **chapter 6**, we demonstrate that lifting the NV from the magnetic surface by > 200 nm prevents the observed NV saturation and decoherence. Specifically, we achieved high and constant contrast imaging of different spin wavelengths by tuning the NV-sample distance according to the expected wavelength. We then showed that we could recover the in-contact NV response and achieve high-wavenumber sensitivity by reducing the spin-wave drive power by more than two orders of magnitude.

Note that although the ensemble-NV probes used in chapter 5 were optimal for studying the evanescent fields of thermal spin waves, they do not provide nanometre imaging resolution parallel to the sample plane. As such, we used here a commercially available NV probe with a single NV, enabling an imaging resolution of ~20 nm, which revealed a rich pattern of nanoscale spin waves with wavelengths down to ~360 nm. The broad range of two-dimensional wavevectors is particularly unexpected because of our one-dimensional excitation geometry, which we attributed to defect-enhanced scattering of the primarily excited low-wavenumber mode to higher momentum modes. Our spin wave images showed that the NV-sample distance provides a wavelength filter necessary to detect and distinguish the stray fields of nanoscale spin waves from those of frequency-degenerate lower wavenumber modes that are more efficiently excited, paving the way for high-resolution imaging of magnon condensates[16] or current distributions in microwave electronics.

Finally, throughout this work, we continuously optimized our diamond fabrication routines. The second part of **chapter 4** describes the realization of our latest generation of scanning NV probes with an optimal shape for NV PL collection and high magnetic field sensitivity. In particular, we realized semi-conical-shaped NV probes with a 14° tapering angle for which simulations predict a PL collection that is twice as efficient compared to standard cylindrical probes. Furthermore, we reduced fabrication complexity by excluding the use of HSQ resist and using standard oxygen-based diamond etch recipes. Although creating single shallow NV centres with long coherence times is still a work in progress and limits our fabrication yield, a first optical inspection shows PL rates of more than 3 MHz, an indication of the high PL collection efficiency of our

newly shaped probes. In future experiments, such high collection efficiency probes will speed up our measurements or enable revealing the weak magnetic signals associated with exotic spin-wave phenomena, such as magnons in two-dimensional materials.

To conclude, we successfully realized a platform for magnetic imaging of nanoscale spin waves based on the electron spin of the NV centre in diamond. Our spin-wave imaging experiments showing targeted delivery of high-density magnon gasses and the presence of nanoscale spin-waves within a sea of more efficiently excited low-wavenumber modes are illustrative of the rich physics that can be exposed by scanning NV magnetometry. At the same time, we optimized our diamond fabrication recipes and realized a second generation of NV probes that provide a higher PL collection efficiency for higher magnetic field sensitivity. The exciting quality advancement of NV probes, not only reported here but also by other groups [101–103] and by industry[181], pushes the performance of scanning NV magnetometry forward with many research opportunities lying ahead that we will now briefly touch upon.

7.2. OUTLOOK

Having benchmarked our technique for studying spin waves in the model magnet YIG, we are now in the exciting position to utilize it and explore spin-wave physics in more exotic systems. In particular, the discovery of magnetism in two dimensions, e.g., in van der Waals materials (CrI_3[182], $C_2G_2T_6$[183]), or complex oxides ($SrRuO_3$[184]), has opened many avenues for exciting physics research. Magnetism in 2D materials is interesting because the reduced dimensions lead to stronger interactions and more prominent spin fluctuations [25, 185–187]. This may give rise to exotic properties that are elusive in their 3D counterparts. In addition, due to the relatively low number of charge carriers in 2D materials, they offer a unique degree of tunability via strain[188, 189], or electric gating [184, 190–192], useful in devices or when studying magnetic phase transitions.

Despite extensive research in recent years, some questions, such as: How large are the competing magnetic contributions enabling the 2D magnetic state? How large is the spin-wave damping? What is the spin-wave dispersion? How do the magnetic state and the spin-wave density evolve as a function of increased dimensions, going from the 2D limit to the bulk?, remain (largely) unexplored. Our scanning NV magnetometer may shed light on these questions by imaging the material's magnetic texture[41] and spin-wave excitations.

Other exciting research directions our scanning NV magnetometer could be used for are studying non-linear spin-wave interactions, quantum interactions of magnons, or interactions between spin waves and other sources of magnetic fields, such as currents, magnetic domain walls, or vortices in superconductors. Unique to our NV imaging technique is that it can detect these interactions via the stray fields they generate, which is possible even when the magnet is buried underneath optically opaque materials that are typically part of such hybrid devices[77].

NV magnetometry for a broader research community

Secondly, due to diamond's chemical inertness, NV magnetometry opens opportunities to probe nanoscale magnetism in chemically-sensitive samples. For example, several recent works pioneer the use of NV magnetometry for studying paleomagnetic minerals to uncover the history of the earth's magnetic field [48, 49], or the structure of the early solar system [193]. Additionally, in nanobiology, NV magnetometry could be used for the localization of iron proteins in the brain of Alzheimer's patients[194, 195], or sensing of the action potential in nerves [196]. Finally, because NV magnetometry does not require large external magnetic fields to improve its spatial resolution, it is also a cost-effective alternative to other biomedical imaging techniques like MRI.

Towards the third generation of NV probes

NV probes with improved sensitivity or versatility will expand the applications of NV magnetometry. As such, we now list several ongoing and future efforts to bring the performance of our NV probe to the next level:

- **Diamond surface improvement for highly coherent shallow NV centers**
  The strong decoherence of NV centres that are within ~50 nm from the diamond surface severely limits the sensitivity of NV magnetometry to evanescent fields[112, 197]. To enhance the quality of shallow NV centres and our fabrication yield of single-NV probes, the effect of new polishing techniques (§4.2.1) and triacid cleaning at temperatures above 150 °C (SI Note 4.6.1) is being explored.

- **Fabricate NV probes around prelocated NV centers**
  Compared to using NV centres implanted at an average density for each probe to host a single NV centre, fabricating NV probes around prelocalized NV centres has several benefits: 1) The use of a (~2 orders of magnitude) lower implantation dose leads to fewer lattice defects and lower charge noise[112]. 2) We select only those NV centres that have good optical-spin properties. 3) The NV PL collection efficiency is higher than that of a probe with a randomly located NV[135]. 4) A 100% fabrication yield. This fabrication strategy requires automatically identifying NV centres and localizing them with respect to a predefined coordinate system at a challenging accuracy of only several tens of nanometres.

- **Millikelvin sensing with other diamond color centers and fibre-based optics**
  The optical power required for excitation and readout of the NV centre using free space optics limits our current technique to temperatures above several Kelvins. One way to reduce laser heating in a cryostat is by switching to fibre-based optics and embedding the NV in a diamond nanobeam coupled to one of the fibre ends[198, 199]. Recent work from our group shows the first proof-of-concept spin-wave imaging experiment using a scanning-diamond nanobeam with fibre-based optics[118], paving the way to probe spin-wave physics at millikelvin temperatures. Ultimately, integrating other colour centres in diamond, such as the silicon [200] and the tin vacancy[201] that provide better spin-optical properties at such low temperatures enables a further reduction of the laser power. In addition, these defects suffer less from spin decoherence when confined to nanostructures, making them more suitable for integration in diamond nanobeams[202–204].

REFERENCES

(1) O'Grady, P. F. Thales of Miletus: The Beginnings of Western Science and Philosophy. *Western Philosophy Series, Routledge* **2002**.

(2) Hua, J.; Feng, L. Thirty Great Inventions of China: From Millet Agriculture to Artemisinin. **2020**, 663–683.

(3) Jiang, X. The Origins of Sciences in China: History of Science and Technology in China. *Springer Singapore* **2021**, 850.

(4) Duyn, J. H. The future of ultra-high field MRI and fMRI for study of the human brain. *NeuroImage* **2012**, *62*, 1241–8.

(5) Perin, R. The superconducting magnet system for the LHC. *IEEE Transactions on Magnetics* **1991**, *27*, 1735–1742.

(6) Rossi, L. Superconducting magnets for the LHC main lattice. *IEEE Transactions on Applied Superconductivity* **2004**, *14*, 153–158.

(7) McFadyen, I. R.; Fullerton, E. E.; Carey, M. J. State-of-the-art magnetic hard disk drives. *Mrs Bulletin* **2006**, *31*, 379–383.

(8) Moser, A.; Supper, N. F.; Berger, A.; Margulies, D. T.; Fullerton, E. E. Noise subtraction in antiferromagnetically coupled magnetic recording media. *Applied Physics Letters* **2005**, *86*, 262501.

(9) Bloch, F. Zur Theorie des Ferromagnetismus. *Zeitschrift für Physik* **1930**, *61*, 206–219.

(10) Serga, A. A.; Chumak, A. V.; Hillebrands, B. YIG magnonics. *Journal of Physics D: Applied Physics* **2010**, *43*, 264002.

(11) Schneider, T.; Serga, A. A.; Leven, B.; Hillebrands, B.; Stamps, R. L.; Kostylev, M. P. Realization of spin-wave logic gates. *Applied Physics Letters* **2008**, *92*, 022505.

(12) Chumak, A. V. et al. Roadmap on Spin-Wave Computing. *IEEE Transactions on Magnetics* **2022**, *58*, 0800172.

(13) Csaba, G.; Papp, A.; Porod, W. Spin-wave based realization of optical computing primitives. *Journal of Applied Physics* **2014**, *115*, 17C741.

(14) Chumak, A. V.; Serga, A. A.; Hillebrands, B. Magnon transistor for all-magnon data processing. *Nature Communications* **2014**, *5*, 4700.

(15) Wang, Q.; Hamadeh, A.; Verba, R.; Lomakin, V.; Mohseni, M.; Hillebrands, B.; Chumak, A. V.; Pirro, P. A nonlinear magnonic nano-ring resonator. *npj Computational Materials* **2020**, *6*, 192.

(16) Demokritov, S. O.; Demidov, V. E.; Dzyapko, O.; Melkov, G. A.; Serga, A. A.; Hillebrands, B.; Slavin, A. N. Bose–Einstein condensation of quasi-equilibrium magnons at room temperature under pumping. *Nature* **2006**, *443*, 430–433.

(17) Bunkov, Y. M.; Volovik, G. E. Magnon Bose–Einstein condensation and spin su-
      perfluidity. *Journal of Physics: Condensed Matter* **2010**, *22*, 164210.

(18) Sonin, E. B. Spin superfluidity and spin waves in YIG films. *Phys. Rev. B* **2017**, *95*,
      144432.

(19) Berk, C.; Jaris, M.; Yang, W.; Dhuey, S.; Cabrini, S.; Schmidt, H. Strongly cou-
      pled magnon-phonon dynamics in a single nanomagnet. *Nature Communica-
      tions* **2019**, *10*, 2652.

(20) Zhang, X.; Bauer, G. E. W.; Yu, T. Unidirectional Pumping of Phonons by Magne-
      tization Dynamics. *Phys. Rev. Lett.* **2020**, *125*, 077203.

(21) Li, Y.; Zhao, C.; Zhang, W.; Hoffmann, A.; Novosad, V. Advances in coherent cou-
      pling between magnons and acoustic phonons. *APL Materials* **2021**, *9*, 060902.

(22) Awschalom, D. D. et al. Quantum Engineering With Hybrid Magnonic Systems
      and Materials (Invited Paper). *IEEE Transactions on Quantum Engineering* **2021**,
      2, 1–36.

(23) Kounalakis, M.; Bauer, G. E. W.; Blanter, Y. M. Analog Quantum Control of Magnonic
      Cat States on a Chip by a Superconducting Qubit. *Phys. Rev. Lett.* **2022**, *129*, 037205.

(24) Park, J.-G. Opportunities and challenges of 2D magnetic van der Waals materials:
      magnetic graphene? *Journal of Physics: Condensed Matter* **2016**, *28*, 301001.

(25) Burch, K. S.; Mandrus, D.; Park, J.-G. Magnetism in two-dimensional van der
      Waals materials. *Nature* **2018**, *563*, 47–52.

(26) Xing, W.; Qiu, L.; Wang, X.; Yao, Y.; Ma, Y.; Cai, R.; Jia, S.; Xie, X. C.; Han, W. Magnon
      Transport in Quasi-Two-Dimensional van der Waals Antiferromagnets. *Phys. Rev.
      X* **2019**, *9*, 011026.

(27) Bae, Y. J. et al. Exciton-coupled coherent magnons in a 2D semiconductor. *Nature*
      2022, *609*, 282–286.

(28) Doherty, M. W.; Manson, N. B.; Delaney, P.; Jelezko, F.; Wrachtrup, J.; Hollenberg,
      L. C. L. The nitrogen-vacancy colour centre in diamond. *Physics Reports* **2013**,
      528, 1–45.

(29) Rondin, L.; Tetienne, J. P.; Hingant, T.; Roch, J. F.; Maletinsky, P.; Jacques, V. Magne-
      tometry with nitrogen-vacancy defects in diamond. *Reports on Progress in Physics*
      2014, *77*, 056503.

(30) Schirhagl, R.; Chang, K.; Loretz, M.; Degen, C. L. Nitrogen-Vacancy Centers in
      Diamond: Nanoscale Sensors for Physics and Biology. *Annual Review of Physical
      Chemistry* **2014**, *65*, PMID: 24274702, 83–105.

(31) Jelezko, F.; Gaebel, T.; Popa, I.; Domhan, M.; Gruber, A.; Wrachtrup, J. Observation
      of Coherent Oscillation of a Single Nuclear Spin and Realization of a Two-Qubit
      Conditional Quantum Gate. *Physical Review Letters* **2004**, *93*, 130501.

(32) Balasubramanian, G.; Neumann, P.; Twitchen, D.; Markham, M.; Kolesov, R.; Mizuochi,
      N.; Isoya, J.; Achard, J.; Beck, J.; Tissler, J.; Jacques, V.; Hemmer, P. R.; Jelezko, F.;
      Wrachtrup, J. Ultralong spin coherence time in isotopically engineered diamond.
      Nature Materials **2009**, *8*, 383–387.

7

(33) Dréau, A.; Lesik, M.; Rondin, L.; Spinicelli, P.; Arcizet, O.; Roch, J. F.; Jacques, V. Avoiding power broadening in optically detected magnetic resonance of single NV defects for enhanced dc magnetic field sensitivity. *Physical Review B* **2011**, *84*, 195204.

(34) Barrett, S. D.; Kok, P. Efficient high-fidelity quantum computation using matter qubits and linear optics. *Physical Review A* **2005**, *71*, 060310.

(35) Waldherr, G.; Wang, Y.; Zaiser, S.; Jamali, M.; Schulte-Herbrüggen, T.; Abe, H.; Ohshima, T.; Isoya, J.; Du, J. F.; Neumann, P.; Wrachtrup, J. Quantum error correction in a solid-state hybrid spin register. *Nature* **2014**, *506*, 204–207.

(36) Pfaff, W.; Hensen, B. J.; Bernien, H.; van Dam, S. B.; Blok, M. S.; Taminiau, T. H.; Tiggelman, M. J.; Schouten, R. N.; Markham, M.; Twitchen, D. J.; Hanson, R. Unconditional quantum teleportation between distant solid-state quantum bits. *Science* **2014**, *345*, 532–535.

(37) Hensen, B. et al. Loophole-free Bell inequality violation using electron spins separated by 1.3 kilometres. *Nature* **2015**, *526*, 682–686.

(38) Taminiau, T. H.; Wagenaar, J. J. T.; van der Sar, T.; Jelezko, F.; Dobrovitski, V. V.; Hanson, R. Detection and Control of Individual Nuclear Spins Using a Weakly Coupled Electron Spin. *Physical Review Letters* **2012**, *109*, 137602.

(39) Kolkowitz, S.; Unterreithmeier, Q. P.; Bennett, S. D.; Lukin, M. D. Sensing Distant Nuclear Spins with a Single Electron Spin. *Physical Review Letters* **2012**, *109*, 137601.

(40) Zhao, N.; Honert, J.; Schmid, B.; Klas, M.; Isoya, J.; Markham, M.; Twitchen, D.; Jelezko, F.; Liu, R.-B.; Fedder, H.; Wrachtrup, J. Sensing single remote nuclear spins. *Nature Nanotechnology* **2012**, *7*, 657–662.

(41) Thiel, L.; Wang, Z.; Tschudin, M. A.; Rohner, D.; Gutiérrez-Lezama, I.; Ubrig, N.; Gibertini, M.; Giannini, E.; Morpurgo, A. F.; Maletinsky, P. Probing magnetism in 2D materials at the nanoscale with single-spin microscopy. *Science* **2019**, *364*, 973–976.

(42) Scheidegger, P. J.; Diesch, S.; Palm, M. L.; Degen, C. L. Scanning nitrogen-vacancy magnetometry down to 350 mK. *Applied Physics Letters* **2022**, *120*, 224001.

(43) Hsieh, S. et al. Imaging stress and magnetism at high pressures using a nanoscale quantum sensor. *Science* **2019**, *366*, 1349–1354.

(44) Taylor, J. M.; Cappellaro, P.; Childress, L.; Jiang, L.; Budker, D.; Hemmer, P. R.; Yacoby, A.; Walsworth, R.; Lukin, M. D. High-sensitivity diamond magnetometer with nanoscale resolution. *Nature Physics* **2008**, *4*, 810–816.

(45) De Lange, G.; Ristè, D.; Dobrovitski, V. V.; Hanson, R. Single-Spin Magnetometry with Multipulse Sensing Sequences. *Phys. Rev. Lett.* **2011**, *106*, 080802.

(46) Puentes, G.; Waldherr, G.; Neumann, P.; Balasubramanian, G.; Wrachtrup, J. Efficient route to high-bandwidth nanoscale magnetometry using single spins in diamond. *Scientific Reports* **2014**, *4*, 4677.

7

(47)   Hall, L. T.; Simpson, D. A.; Hollenberg, L. C. L. Nanoscale sensing and imaging in biology using the nitrogen-vacancy center in diamond. *MRS Bulletin* **2013**, *38*, 162–167.

(48)   Glenn, D. R.; Fu, R. R.; Kehayias, P.; Le Sage, D.; Lima, E. A.; Weiss, B. P.; Walsworth, R. L. Micrometer-scale magnetic imaging of geological samples using a quantum diamond microscope. *Geochemistry, Geophysics, Geosystems* **2017**, *18*, 3254–3267.

(49)   De Groot, L. V.; Fabian, K.; Béguin, A.; Kosters, M. E.; Cortés-Ortuño, D.; Fu, R. R.; Jansen, C. M. L.; Harrison, R. J.; van Leeuwen, T.; Barnhoorn, A. Micromagnetic Tomography for Paleomagnetism and Rock-Magnetism. *Journal of Geophysical Research: Solid Earth* **2021**, *126*, e2021JB022364.

(50)   Chatzidrosos, G.; Wickenbrock, A.; Bougas, L.; Leefer, N.; Wu, T.; Jensen, K.; Dumeige, Y.; Budker, D. Miniature Cavity-Enhanced Diamond Magnetometer. *Phys. Rev. Appl.* **2017**, *8*, 044019.

(51)   Kuwahata, A.; Kitaizumi, T.; Saichi, K.; Sato, T.; Igarashi, R.; Ohshima, T.; Masuyama, Y.; Iwasaki, T.; Hatano, M.; Jelezko, F.; Kusakabe, M.; Yatsui, T.; Sekino, M. Magnetometer with nitrogen-vacancy center in a bulk diamond for detecting magnetic nanoparticles in biomedical applications. *Scientific Reports* **2020**, *10*, 2483.

(52)   Maletinsky, P.; Hong, S.; Grinolds, M. S.; Hausmann, B.; Lukin, M. D.; Walsworth, R. L.; Loncar, M.; Yacoby, A. A robust scanning diamond sensor for nanoscale imaging with single nitrogen-vacancy centres. *Nature Nanotechnology* **2012**, *7*, 320–324.

(53)   Sun, Q.-C.; Song, T.; Anderson, E.; Brunner, A.; Förster, J.; Shalomayeva, T.; Taniguchi, T.; Watanabe, K.; Gräfe, J.; Stöhr, R.; Xu, X.; Wrachtrup, J. Magnetic domains and domain wall pinning in atomically thin CrBr3 revealed by nanoscale imaging. *Nature Communications* **2021**, *12*, 1989.

(54)   Finco, A.; Haykal, A.; Tanos, R.; Fabre, F.; Chouaieb, S.; Akhtar, W.; Robert-Philip, I.; Legrand, W.; Ajejas, F.; Bouzehouane, K. Imaging non-collinear antiferromagnetic textures via single spin relaxometry. *Nature communications* **2021**, *12*, 767.

(55)   Makushko, P. et al. Flexomagnetism and vertically graded Néel temperature of antiferromagnetic Cr2O3 thin films. *Nature Communications* **2022**, *13*, 6745.

(56)   Ku, M. J. H. et al. Imaging viscous flow of the Dirac fluid in graphene. *Nature* **2020**, *583*, 537–541.

(57)   Palm, M.; Huxter, W.; Welter, P.; Ernst, S.; Scheidegger, P.; Diesch, S.; Chang, K.; Rickhaus, P.; Taniguchi, T.; Watanabe, K.; Ensslin, K.; Degen, C. Imaging of Sub-microampere Currents in Bilayer Graphene Using a Scanning Diamond Magnetometer. *Phys. Rev. Appl.* **2022**, *17*, 054008.

(58)   Bertelli, I.; Carmiggelt, J. J.; Yu, T.; Simon, B. G.; Pothoven, C. C.; Bauer, G. E. W.; Blanter, Y. M.; Aarts, J.; Van Der Sar, T. Magnetic resonance imaging of spin-wave transport and interference in a magnetic insulator. *Science Advances* **2020**, *6*, eabd3556.

7

(59)   Giamarchi, T.; Rüegg, C.; Tchernyshyov, O. Bose–Einstein condensation in magnetic insulators. *Nature Physics* **2008**, *4*, 198–204.

(60)   Wang, Q.; Pirro, P.; Verba, R.; Slavin, A.; Hillebrands, B.; Chumak, A. V. Reconfigurable nanoscale spin-wave directional coupler. *Science Advances* **2018**, *4*, e1701517.

(61)   Chumak, A. V.; Vasyuchka, V.; Serga, A.; Hillebrands, B. Magnon spintronics. *Nature Physics* **2015**, *11*, 453–461.

(62)   Chumak, A. V.; Serga, A. A.; Jungfleisch, M. B.; Neb, R.; Bozhko, D. A.; Tiberkevich, V. S.; Hillebrands, B. Direct detection of magnon spin transport by the inverse spin Hall effect. *Applied Physics Letters* **2012**, *100*, 082405.

(63)   Cornelissen, L. J.; Liu, J.; Duine, R. A.; Youssef, J. B.; Van Wees, B. J. Long-distance transport of magnon spin information in a magnetic insulator at room temperature. *Nature Physics* **2015**, *11*, 1022–1026.

(64)   Vlaminck, V.; Bailleul, M. Current-Induced Spin-Wave Doppler Shift. *Science* **2008**, *322*, 410–413.

(65)   Chen, J.; Yu, T.; Liu, C.; Liu, T.; Madami, M.; Shen, K.; Zhang, J.; Tu, S.; Alam, M. S.; Xia, K.; Wu, M.; Gubbiotti, G.; Blanter, Y. M.; Bauer, G. E. W.; Yu, H. Excitation of unidirectional exchange spin waves by a nanoscale magnetic grating. *Physical Review B* **2019**, *100*, 104427.

(66)   Carmiggelt, J. J.; Dreijer, O. C.; Dubs, C.; Surzhenko, O.; Sar, T. v. d. Electrical spectroscopy of the spin-wave dispersion and bistability in gallium-doped yttrium iron garnet. *Applied Physics Letters* **2021**, *119*, 202403.

(67)   Demidov, V. E.; Kostylev, M. P.; Rott, K.; Krzysteczko, P.; Reiss, G.; Demokritov, S. O. Excitation of microwaveguide modes by a stripe antenna. *Applied Physics Letters* **2009**, *95*, 112509.

(68)   Pirro, P.; Brächer, T.; Chumak, A. V.; Lägel, B.; Dubs, C.; Surzhenko, O.; Görnert, P.; Leven, B.; Hillebrands, B. Spin-wave excitation and propagation in microstructured waveguides of yttrium iron garnet/Pt bilayers. *Applied Physics Letters* **2014**, *104*, 012402.

(69)   Dieterle, G. et al. Coherent Excitation of Heterosymmetric Spin Waves with Ultrashort Wavelengths. *Physical Review Letters* **2019**, *122*, 117202.

(70)   Albisetti, E.; Tacchi, S.; Silvani, R.; Scaramuzzi, G.; Finizio, S.; Wintz, S.; Rinaldi, C.; Cantoni, M.; Raabe, J.; Carlotti, G.; Bertacco, R.; Riedo, E.; Petti, D. Optically Inspired Nanomagnonics with Nonreciprocal Spin Waves in Synthetic Antiferromagnets. *Advanced Materials* **2020**, *32*, 1906439.

(71)   Park, J. P.; Eames, P.; Engebretson, D. M.; Berezovsky, J.; Crowell, P. A. Spatially Resolved Dynamics of Localized Spin-Wave Modes in Ferromagnetic Wires. *Physical Review Letters* **2002**, *89*, 277201.

(72)   Acremann, Y.; Back, C. H.; Buess, M.; Portmann, O.; Vaterlaus, A.; Pescia, D.; Melchior, H. Imaging Precessional Motion of the Magnetization Vector. *Science* **2000**, *290*, 492–495.

7

(73)   Rustagi, A.; Bertelli, I.; Van Der Sar, T.; Upadhyaya, P. Sensing chiral magnetic noise via quantum impurity relaxometry. *Physical Review B* **2020**, *102*, 220403(R).

(74)   Bertelli, I. Magnetic imaging of spin waves and magnetic phase transitions with nitrogen-vacancy centers in diamond, Thesis, 2021.

(75)   Borst, M.; Vree, P. H.; Lowther, A.; Teepe, A.; Kurdi, S.; Bertelli, I.; Simon, B. G.; Blanter, Y. M.; van der Sar, T. Temperature-, field-, and laser-control of spin-wave dispersion and scattering using a superconducting gate. *(In preparation)* **2023**.

(76)   Gilbert, T. L. A phenomenological theory of damping in ferromagnetic materials. *IEEE Transactions on Magnetics* **2004**, *40*, 3443–3449.

(77)   Bertelli, I.; Simon, B. G.; Yu, T.; Aarts, J.; Bauer, G. E. W.; Blanter, Y. M.; van der Sar, T. Imaging Spin-Wave Damping Underneath Metals Using Electron Spins in Diamond. *Advanced Quantum Technologies* **2021**, *4*, 2100094.

(78)   Kittel, C.; McEuen, P.; McEuen, P., *Introduction to solid state physics*; Wiley New York: 1996; Vol. 8.

(79)   Du, C.; Van der Sar, T.; Zhou, T. X.; Upadhyaya, P.; Casola, F.; Zhang, H.; Onbasli, M. C.; Ross, C. A.; Walsworth, R. L.; Tserkovnyak, Y. Control and local measurement of the spin chemical potential in a magnetic insulator. *Science* **2017**, *357*, 195–198.

(80)   Yu, T.; Blanter, Y. M.; Bauer, G. E. W. Chiral pumping of spin waves. *Physical Review Letters* **2019**, *123*, 247202.

(81)   Liu, C. et al. Long-distance propagation of short-wavelength spin waves. *Nature Communications* **2018**, *9*, 738.

(82)   Che, P.; Baumgaertl, K.; Kukolova, A.; Dubs, C.; Grundler, D. Efficient wavelength conversion of exchange magnons below 100 nm by magnetic coplanar waveguides. *Nature Communications* **2020**, *11*, 1445.

(83)   Schwabl, F., *Advanced Quantum Mechanics*; Springer-Verlag: Berlin, 2000.

(84)   Van der Sar, T.; Casola, F.; Walsworth, R.; Yacoby, A. Nanometre-scale probing of spin waves using single electron spins. *Nature Communications* **2015**, *6*, 7886.

(85)   Flebus, B.; Tserkovnyak, Y. Quantum-Impurity Relaxometry of Magnetization Dynamics. *Physical Review Letters* **2018**, *121*, 187204.

(86)   Chatterjee, S.; Rodriguez-Nieva, J. F.; Demler, E. Diagnosing phases of magnetic insulators via noise magnetometry with spin qubits. *Physical Review B* **2019**, *99*, 104425.

(87)   Manson, N. B.; Harrison, J. P.; Sellars, M. J. Nitrogen-vacancy center in diamond: Model of the electronic structure and associated dynamics. *Physical Review B* **2006**, *74*, 104303.

(88)   Loubser, J. H. N.; Wyk, J. A. v. Electron spin resonance in the study of diamond. *Reports on Progress in Physics* **1978**, *41*, 1201.

(89)   Ashcroft, N. W.; Mermin, N. D., *Solid State Physics*; Brooks/Cole, Cengage Learning: 1976.

7

(90) Gruber, A.; Dräbenstedt, A.; Tietz, C.; Fleury, L.; Wrachtrup, J.; Borczyskowski, C. v. Scanning Confocal Optical Microscopy and Magnetic Resonance on Single Defect Centers. *Science* **1997**, *276*, 2012–2014.

(91) Awschalom, D. D.; Hanson, R.; Wrachtrup, J.; Zhou, B. B. Quantum technologies with optically interfaced solid-state spins. *Nature Photonics* **2018**, *12*, 516–527.

(92) Van der Sar, T.; Taminiau, T. H.; Hanson, R. Diamond-based quantum technologies. *Photoniques* **2021**, *107*, 44–48.

(93) Rondin, L.; Dantelle, G.; Slablab, A.; Grosshans, F.; Treussart, F.; Bergonzo, P.; Perruchas, S.; Gacoin, T.; Chaigneau, M.; Chang, H.-C.; Jacques, V.; Roch, J.-F. Surface-induced charge state conversion of nitrogen-vacancy defects in nanodiamonds. *Phys. Rev. B* **2010**, *82*, 115449.

(94) Robledo, L.; Bernien, H.; Sar, T. v. d.; Hanson, R. Spin dynamics in the optical cycle of single nitrogen-vacancy centres in diamond. *New Journal of Physics* **2011**, *13*, 025013.

(95) Tetienne, J. P.; Rondin, L.; Spinicelli, P.; Chipaux, M.; Debuisschert, T.; Roch, J. F.; Jacques, V. Magnetic-field-dependent photodynamics of single NV defects in diamond: an application to qualitative all-optical magnetic imaging. *New Journal of Physics* **2012**, *14*, 103033.

(96) Epstein, R. J.; Mendoza, F. M.; Kato, Y. K.; Awschalom, D. D. Anisotropic interactions of a single spin and dark-spin spectroscopy in diamond. *Nature Physics* **2005**, *1*, 94–98.

(97) Goldman, M. L.; Sipahigil, A.; Doherty, M. W.; Yao, N. Y.; Bennett, S. D.; Markham, M.; Twitchen, D. J.; Manson, N. B.; Kubanek, A.; Lukin, M. D. Phonon-induced population dynamics and intersystem crossing in nitrogen-vacancy centers. *Physical review letters* **2015**, *114*, 145502.

(98) Maze, J. R.; Stanwix, P. L.; Hodges, J. S.; Hong, S.; Taylor, J. M.; Cappellaro, P.; Jiang, L.; Dutt, M. V. G.; Togan, E.; Zibrov, A. S.; Yacoby, A.; Walsworth, R. L.; Lukin, M. D. Nanoscale magnetic sensing with an individual electronic spin in diamond. *Nature* **2008**, *455*, 644–647.

(99) Balasubramanian, G.; Chan, I. Y.; Kolesov, R.; Al-Hmoud, M.; Tisler, J.; Shin, C.; Kim, C.; Wojcik, A.; Hemmer, P. R.; Krueger, A.; Hanke, T.; Leitenstorfer, A.; Bratschitsch, R.; Jelezko, F.; Wrachtrup, J. Nanoscale imaging magnetometry with diamond spins under ambient conditions. *Nature* **2008**, *455*, 648–651.

(100) Vitanov, N. V.; Shore, B. W.; Yatsenko, L.; Böhmer, K.; Halfmann, T.; Rickes, T.; Bergmann, K. Power broadening revisited: theory and experiment. *Optics Communications* **2001**, *199*, 117–126.

(101) Fuchs, P.; Challier, M.; Neu, E. Optimized single-crystal diamond scanning probes for high sensitivity magnetometry. *New Journal of Physics* **2018**, *20*, 125001.

(102) Wan, N. H.; Shields, B. J.; Kim, D.; Mouradian, S.; Lienhard, B.; Walsh, M.; Bakhru, H.; Schröder, T.; Englund, D. Efficient extraction of light from a nitrogen-vacancy center in a diamond parabolic reflector. *Nano letters* **2018**, *18*, 2787–2793.

7

(103) Hedrich, N.; Rohner, D.; Batzer, M.; Maletinsky, P.; Shields, B. J. Parabolic Diamond Scanning Probes for Single-Spin Magnetic Field Imaging. *Physical Review Applied* **2020**, *14*, 064007.

(104) Rollo, M.; Finco, A.; Tanos, R.; Fabre, F.; Devolder, T.; Robert-Philip, I.; Jacques, V. Quantitative study of the response of a single NV defect in diamond to magnetic noise. *Physical Review B* **2021**, *103*, 235418.

(105) Degen, C. L. Scanning magnetic field microscope with a diamond single-spin sensor. *Applied Physics Letters* **2008**, *92*, 243111.

(106) Casola, F.; Van Der Sar, T.; Yacoby, A. Probing condensed matter physics with magnetometry based on nitrogen-vacancy centres in diamond. *Nature Reviews Materials* **2018**, *3*, 17088.

(107) Rondin, L.; Tetienne, J. P.; Rohart, S.; Thiaville, A.; Hingant, T.; Spinicelli, P.; Roch, J. F.; Jacques, V. Stray-field imaging of magnetic vortices with a single diamond spin. *Nature Communications* **2013**, *4*, 2279.

(108) Tetienne, J. P.; Hingant, T.; Martínez, L. J.; Rohart, S.; Thiaville, A.; Diez, L. H.; Garcia, K.; Adam, J. P.; Kim, J. V.; Roch, J. F. The nature of domain walls in ultrathin ferromagnets revealed by scanning nanomagnetometry. *Nature communications* **2015**, *6*, 1–6.

(109) Andrich, P.; de las Casas, C. F.; Liu, X.; Bretscher, H. L.; Berman, J. R.; Heremans, F. J.; Nealey, P. F.; Awschalom, D. D. Long-range spin wave mediated control of defect qubits in nanodiamonds. *npj Quantum Information* **2017**, *3*, 28.

(110) Horsley, A.; Appel, P.; Wolters, J.; Achard, J.; Tallaire, A.; Maletinsky, P.; Treutlein, P. Microwave Device Characterization Using a Widefield Diamond Microscope. *Physical Review Applied* **2018**, *10*, 044039.

(111) Appel, P.; Neu, E.; Ganzhorn, M.; Barfuss, A.; Batzer, M.; Gratz, M.; Tschöpe, A.; Maletinsky, P. Fabrication of all diamond scanning probes for nanoscale magnetometry. *Review of Scientific Instruments* **2016**, *87*, 063703–063703.

(112) Sangtawesin, S. et al. Origins of Diamond Surface Noise Probed by Correlating Single-Spin Measurements with Surface Spectroscopy. *Physical Review X* **2019**, *9*, 031052.

(113) Rodgers, L. V. H.; Hughes, L. B.; Xie, M.; Maurer, P. C.; Kolkowitz, S.; Bleszynski Jayich, A. C.; de Leon, N. P. Materials challenges for quantum technologies based on color centers in diamond. *MRS Bulletin* **2021**, *46*, 623–633.

(114) Hadden, J. P.; Harrison, J. P.; Stanley-Clarke, A. C.; Marseglia, L.; Ho, Y.-L. D.; Patton, B. R.; O'Brien, J. L.; Rarity, J. G. Strongly enhanced photon collection from diamond defect centers under microfabricated integrated solid immersion lenses. *Applied Physics Letters* **2010**, *97*, 241901.

(115) Jamali, M.; Gerhardt, I.; Rezai, M.; Frenner, K.; Fedder, H.; Wrachtrup, J. Microscopic diamond solid-immersion-lenses fabricated around single defect centers by focused ion beam milling. *Review of Scientific Instruments* **2014**, *85*, 123703.

7

(116) Pompili, M.; Hermans, S. L. N.; Baier, S.; Beukers, H. K. C.; Humphreys, P. C.; Schouten, R. N.; Vermeulen, R. F. L.; Tiggelman, M. J.; dos Santos Martins, L.; Dirkse, B.; Wehner, S.; Hanson, R. Realization of a multinode quantum network of remote solid-state qubits. *Science* **2021**, *372*, 259–264.

(117) Zhou, T. X.; Stöhr, R. J.; Yacoby, A. Scanning diamond NV center probes compatible with conventional AFM technology. *Applied Physics Letters* **2017**, *111*, 163106.

(118) Li, Y.; Gerritsma, F. A.; Kurdi, S.; Codreanu, N.; Gröblacher, S.; Hanson, R.; Norte, R.; van der Sar, T. A Fiber-Coupled Scanning Magnetometer with Nitrogen-Vacancy Spins in a Diamond Nanobeam. *ACS Photonics* **2023 ASAP**.

(119) Chu, Y. et al. Coherent Optical Transitions in Implanted Nitrogen Vacancy Centers. *Nano Letters* **2014**, *14*, 1982–1986.

(120) Tao, Y.; Boss, J. M.; Moores, B. A.; Degen, C. L. Single-crystal diamond nanomechanical resonators with quality factors exceeding one million. *Nature Communications* **2014**, *5*, 3638.

(121) Ruf, M.; Ijspeert, M.; van Dam, S.; de Jong, N.; van den Berg, H.; Evers, G.; Hanson, R. Optically Coherent Nitrogen-Vacancy Centers in Micrometer-Thin Etched Diamond Membranes. *Nano Letters* **2019**, *19*, 3987–3992.

(122) Hicks, M.-L.; Pakpour-Tabrizi, A. C.; Jackman, R. B. Diamond Etching Beyond 10 μm with Near-Zero Micromasking. *Scientific Reports* **2019**, *9*, 15619.

(123) Challier, M.; Sonusen, S.; Barfuss, A.; Rohner, D.; Riedel, D.; Koelbl, J.; Ganzhorn, M.; Appel, P.; Maletinsky, P.; Neu, E. Advanced Fabrication of Single-Crystal Diamond Membranes for Quantum Technologies. *Micromachines* **2018**, *9*, 148.

(124) Pezzagna, S.; Naydenov, B.; Jelezko, F.; Wrachtrup, J.; Meijer, J. Creation efficiency of nitrogen-vacancy centres in diamond. *New Journal of Physics* **2010**, *12*, 065017.

(125) Brown, K. J.; Chartier, E.; Sweet, E. M.; Hopper, D. A.; Bassett, L. C. Cleaning diamond surfaces using boiling acid treatment in a standard laboratory chemical hood. *Journal of Chemical Health & Safety* **2019**, *26*, 40–44.

(126) Van Dam, S. B.; Walsh, M.; Degen, M. J.; Bersin, E.; Mouradian, S. L.; Galiullin, A.; Ruf, M.; IJspeert, M.; Taminiau, T. H.; Hanson, R.; Englund, D. R. Optical coherence of diamond nitrogen-vacancy centers formed by ion implantation and annealing. *Phys. Rev. B* **2019**, *99*, 161203.

(127) Allers, L.; Collins, A. T.; Hiscock, J. The annealing of interstitial-related optical centres in type II natural and CVD diamond. *Diamond and Related Materials* **1998**, *7*, 228–232.

(128) Simon, B. G.; Kurdi, S.; La, H.; Bertelli, I.; Carmiggelt, J. J.; Ruf, M.; De Jong, N.; Van Den Berg, H.; Katan, A. J.; Van Der Sar, T. Directional excitation of a high-density magnon gas using coherently driven spin waves. *Nano letters* **2021**, *21*, 8213–8219.

(129) Choy, J. T.; Bulu, I.; Hausmann, B. J. M.; Janitz, E.; Huang, I.-C.; Lončar, M. Spontaneous emission and collection efficiency enhancement of single emitters in diamond via plasmonic cavities and gratings. *Applied Physics Letters* **2013**, *103*, 161101.

7

(130) Radtke, M.; Nelz, R.; Slablab, A.; Neu, E. Reliable Nanofabrication of Single-Crystal Diamond Photonic Nanostructures for Nanoscale Sensing. *Micromachines* **2019**, *10*.

(131) Novotny, L.; Hecht, B., *Principles of Nano-Optics*; Cambridge University Press, New York: 2006, p 559.

(132) Benevides, R.; Ménard, M.; Wiederhecker, G. S.; Mayer Alegre, T. P. Ar/Cl2 etching of GaAs optomechanical microdisks fabricated with positive electroresist. *Optical Materials Express* **2020**, *10*, 57–67.

(133) Kirchner, R.; Guzenko, V. A.; Vartiainen, I.; Chidambaram, N.; Schift, H. ZEP520A — A resist for electron-beam grayscale lithography and thermal reflow. *Microelectronic Engineering* **2016**, *153*, 71–76.

(134) Kirchner, R.; Schift, H. Thermal reflow of polymers for innovative and smart 3D structures: A review. *Materials Science in Semiconductor Processing* **2019**, *92*, 58–72.

(135) Amghar, S. Fabrication and design of diamond nanopillars for single Nitrogen-Vacancy scanning probes. *MSc Physics Thesis, Delft University of Technology* **2020**.

(136) Norte, R. 0.; Moura, J. 0.; Gröblacher, S. Mechanical Resonators for Quantum Optomechanics Experiments at Room Temperature. *Physical Review Letters* **2016**, *116*, 147202.

(137) Bernard, S.; Reinhardt, C.; Dumont, V.; Peter, Y.-A.; Sankey, J. C. Precision resonance tuning and design of SiN photonic crystal reflectors. *Optics Letters* **2016**, *41*, 5624–5627.

(138) Fink, J. M.; Kalaee, M.; Norte, R.; Pitanti, A.; Painter, O. Efficient microwave frequency conversion mediated by a photonics compatible silicon nitride nanobeam oscillator. *Quantum Science and Technology* **2020**, *5*, 034011.

(139) Antonio, G. N.; Bertelli, I.; Simon, B. G.; Medapalli, R.; Afanasiev, D.; Sar, T. v. d. Magnetic imaging and statistical analysis of the metamagnetic phase transition of FeRh with electron spins in diamond. *Journal of Applied Physics* **2021**, *129*, 223904.

(140) Kurtsiefer, C.; Mayer, S.; Zarda, P.; Weinfurter, H. Stable Solid-State Source of Single Photons. *Phys. Rev. Lett.* **2000**, *85*, 290–293.

(141) Cornelissen, L. J.; Liu, J.; Van Wees, B. J.; Duine, R. A. Spin-current-controlled modulation of the magnon spin conductance in a three-terminal magnon transistor. *Physical Review Letters* **2018**, *120*, 097702.

(142) Wimmer, T.; Althammer, M.; Liensberger, L.; Vlietstra, N.; Geprägs, S.; Weiler, M.; Gross, R.; Huebl, H. Spin transport in a magnetic insulator with zero effective damping. *Physical Review Letters* **2019**, *123*, 257201.

(143) Nan, T.; Lee, Y.; Zhuang, S.; Hu, Z.; Clarkson, J. D.; Wang, X.; Ko, C.; Choe, H.; Chen, Z.; Budil, D. Electric-field control of spin dynamics during magnetic phase transitions. *Science Advances* **2020**, *6*, eabd2613.

(144) Schneider, M.; Brächer, T.; Breitbach, D.; Lauer, V.; Pirro, P.; Bozhko, D. A.; Musiienko-Shmarova, H. Y.; Heinz, B.; Wang, Q.; Meyer, T. Bose–Einstein condensation of quasiparticles by rapid cooling. *Nature Nanotechnology* **2020**, *15*, 457–461.

(145) Demokritov, S. O.; Demidov, V. E.; Dzyapko, O.; Melkov, G. A.; Slavin, A. N. Quantum coherence due to Bose–Einstein condensation of parametrically driven magnons. *New Journal of Physics* **2008**, *10*, 045029.

(146) Kim, S. K.; Tserkovnyak, Y.; Tchernyshyov, O. Propulsion of a domain wall in an antiferromagnet by magnons. *Physical Review B* **2014**, *90*, 104406.

(147) Shen, P.; Tserkovnyak, Y.; Kim, S. K. Driving a magnetized domain wall in an antiferromagnet by magnons. *Journal of Applied Physics* **2020**, *127*, 223905.

(148) Chang, L.-J.; Liu, Y.-F.; Kao, M.-Y.; Tsai, L.-Z.; Liang, J.-Z.; Lee, S.-F. Ferromagnetic domain walls as spin wave filters and the interplay between domain walls and spin waves. *Scientific Reports* **2018**, *8*, 3910.

(149) Wang, W.; Albert, M.; Beg, M.; Bisotti, M.-A.; Chernyshenko, D.; Cortés-Ortuño, D.; Hawke, I.; Fangohr, H. Magnon-driven domain-wall motion with the Dzyaloshinskii-Moriya interaction. *Physical Review Letters* **2015**, *114*, 087203.

(150) Kajiwara, Y.; Harii, K.; Takahashi, S.; Ohe, J.-i.; Uchida, K.; Mizuguchi, M.; Umezawa, H.; Kawai, H.; Ando, K.; Takanashi, K. Transmission of electrical signals by spin-wave interconversion in a magnetic insulator. *Nature* **2010**, *464*, 262–266.

(151) Schneider, M. et al. Control of the Bose-Einstein Condensation of Magnons by the Spin Hall Effect. *Physical Review Letters* **2021**, *127*, 237203–237203.

(152) Wettling, W.; Wilber, W. D.; Kabos, P.; Patton, C. E. Light scattering from parallel-pump instabilities in yttrium iron garnet. *Physical Review Letters* **1983**, *51*, 1680.

(153) Bauer, H. G.; Majchrak, P.; Kachel, T.; Back, C. H.; Woltersdorf, G. Nonlinear spin-wave excitations at low magnetic bias fields. *Nature Communications* **2015**, *6*, 8274.

(154) McCullian, B. A.; Thabt, A. M.; Gray, B. A.; Melendez, A. L.; Wolf, M. S.; Safonov, V. L.; Pelekhov, D. V.; Bhallamudi, V. P.; Page, M. R.; Hammel, P. C. Broadband multi-magnon relaxometry using a quantum spin sensor for high frequency ferromagnetic dynamics sensing. *Nature Communications* **2020**, *11*, 5229.

(155) Pitaevskii, L.; Stringari, S., *Bose-Einstein condensation and superfluidity*; Oxford University Press: 2016.

(156) Demidov, V. E.; Dzyapko, O.; Demokritov, S. O.; Melkov, G. A.; Slavin, A. N. Thermalization of a parametrically driven magnon gas leading to Bose-Einstein condensation. *Physical Review Letters* **2007**, *99*, 037205.

(157) Wang, X.; Xiao, Y.; Liu, C.; Lee-Wong, E.; McLaughlin, N. J.; Wang, H.; Wu, M.; Wang, H.; Fullerton, E. E.; Du, C. R. Electrical control of coherent spin rotation of a single-spin qubit. *npj Quantum Information* **2020**, *6*, 78.

(158) Wolfe, C. S.; Bhallamudi, V. P.; Wang, H. L.; Du, C. H.; Manuilov, S.; Teeling-Smith, R. M.; Berger, A. J.; Adur, R.; Yang, F. Y.; Hammel, P. C. Off-resonant manipulation of spins in diamond via precessing magnetization of a proximal ferromagnet. *Physical Review B* **2014**, *89*, 180406(R).

7

(159)   Wolfe, C. S.; Manuilov, S. A.; Purser, C. M.; Teeling-Smith, R.; Dubs, C.; Hammel, P. C.; Bhallamudi, V. P. Spatially resolved detection of complex ferromagnetic dynamics using optically detected nitrogen-vacancy spins. *Applied Physics Letters* **2016**, *108*, 232409.

(160)   Lee-Wong, E.; Xue, R.; Ye, F.; Kreisel, A.; van Der Sar, T.; Yacoby, A.; Du, C. R. Nanoscale detection of magnon excitations with variable wavevectors through a quantum spin sensor. *Nano Letters* **2020**, *20*, 3284–3290.

(161)   Kabos, P.; Wiese, G.; Patton, C. E. Measurement of spin wave instability magnon distributions for subsidiary absorption in yttrium iron garnet films by Brillouin light scattering. *Physical Review Letters* **1994**, *72*, 2093–2096.

(162)   Lillie, S. E.; Broadway, D. A.; Dontschuk, N.; Scholten, S. C.; Johnson, B. C.; Wolf, S.; Rachel, S.; Hollenberg, L. C. L.; Tetienne, J.-P. Laser Modulation of Superconductivity in a Cryogenic Wide-field Nitrogen-Vacancy Microscope. *Nano Letters* **2020**, *20*, 1855–1861.

(163)   Klingler, S.; Chumak, A. V.; Mewes, T.; Khodadadi, B.; Mewes, C.; Dubs, C.; Surzhenko, O.; Hillebrands, B.; Conca, A. Measurements of the exchange stiffness of YIG films using broadband ferromagnetic resonance techniques. *Journal of Physics D: Applied Physics* **2014**, *48*, 015001.

(164)   Rezende, S. M., *Fundamentals of magnonics*; Springer: 2020; Vol. 969.

(165)   Sebastian, T.; Schultheiss, K.; Obry, B.; Hillebrands, B.; Schultheiss, H. Microfocused Brillouin light scattering: imaging spin waves at the nanoscale. *Frontiers in Physics* **2015**, *3*, 35.

(166)   Sluka, V. et al. Emission and propagation of 1D and 2D spin waves with nanoscale wavelengths in anisotropic spin textures. *Nature Nanotechnology* **2019**, *14*, 328–333.

(167)   Degen, C. L.; Reinhard, F.; Cappellaro, P. Quantum sensing. *Reviews of Modern Physics* **2017**, *89*, 035002.

(168)   Koerner, C.; Dreyer, R.; Wagener, M.; Liebing, N.; Bauer, H. G.; Woltersdorf, G. Frequency multiplication by collective nanoscale spin-wave dynamics. *Science* **2022**, *375*, 1165–1169.

(169)   Zhou, T. X.; Carmiggelt, J. J.; Gächter, L. M.; Esterlis, I.; Sels, D.; Stöhr, R. J.; Du, C.; Fernandez, D.; Rodriguez-Nieva, J. F.; Büttner, F.; Demler, E.; Yacoby, A. A magnon scattering platform. *Proceedings of the National Academy of Sciences* **2021**, *118*, e2019473118.

(170)   Hula, T.; Schultheiss, K.; Buzdakov, A.; Körber, L.; Bejarano, M.; Flacke, L.; Liensberger, L.; Weiler, M.; Shaw, J. M.; Nembach, H. T.; Fassbender, J.; Schultheiss, H. Nonlinear losses in magnon transport due to four-magnon scattering. *Applied Physics Letters* **2020**, *117*, 042404.

(171)   Purser, C. M.; Bhallamudi, V. P.; Guo, F.; Page, M. R.; Guo, Q.; Fuchs, G. D.; Hammel, P. C. Spinwave detection by nitrogen-vacancy centers in diamond as a function of probe–sample separation. *Applied Physics Letters* **2020**, *116*, 202401.

(172)   Mohseni, M.; Verba, R.; Brächer, T.; Wang, Q.; Bozhko, D. A.; Hillebrands, B.; Pirro, P. Backscattering Immunity of Dipole-Exchange Magnetostatic Surface Spin Waves. *Physical Review Letters* **2019**, *122*, 197201.

(173)   Yu, C.; Pechan, M. J.; Burgei, W. A.; Mankey, G. J. Lateral standing spin waves in permalloy antidot arrays. *Journal of Applied Physics* **2004**, *95*, 6648–6650.

(174)   Gieniusz, R.; Ulrichs, H.; Bessonov, V. D.; Guzowska, U.; Stognii, A. I.; Maziewski, A. Single antidot as a passive way to create caustic spin-wave beams in yttrium iron garnet films. *Applied Physics Letters* **2013**, *102*, 102409.

(175)   Gieniusz, R.; Bessonov, V. D.; Guzowska, U.; Stognii, A. I.; Maziewski, A. An antidot array as an edge for total non-reflection of spin waves in yttrium iron garnet films. *Applied Physics Letters* **2014**, *104*, 082412.

(176)   Davies, C. S.; Sadovnikov, A. V.; Grishin, S. V.; Sharaevskii, Y. P.; Nikitov, S. A.; Kruglyak, V. V. Generation of propagating spin waves from regions of increased dynamic demagnetising field near magnetic antidots. *Appl. Phys. Lett.* **2015**, *107*, 162401.

(177)   Groß, F.; Zelent, M.; Träger, N.; Förster, J.; Sanli, U. T.; Sauter, R.; Decker, M.; Back, C. H.; Weigand, M.; Keskinbora, K.; Schütz, G.; Krawczyk, M.; Gräfe, J. Building Blocks for Magnon Optics: Emission and Conversion of Short Spin Waves. *ACS Nano* **2020**, *14*, 17184–17193.

(178)   Gräfe, J.; Gruszecki, P.; Zelent, M.; Decker, M.; Keskinbora, K.; Noske, M.; Gawronski, P.; Stoll, H.; Weigand, M.; Krawczyk, M.; Back, C. H.; Goering, E. J.; Schütz, G. Direct observation of spin-wave focusing by a Fresnel lens. *Physical Review B* **2020**, *102*, 024420.

(179)   Greentree, A. D.; Olivero, P.; Draganski, M.; Trajkov, E.; Rabeau, J. R.; Reichart, P.; Gibson, B. C.; Rubanov, S.; Huntington, S. T.; Jamieson, D. N.; Prawer, S. Critical components for diamond-based quantum coherent devices. *Journal of Physics: Condensed Matter* **2006**, *18*, S825–S842.

(180)   Vlaardingerbroek, M. T.; Boer, J. A., *Magnetic resonance imaging: theory and practice*; Springer Science & Business Media: 2013.

(181)   Welter, P.; Rhensius, J.; Morales, A.; Wörnle, M. S.; Lambert, C.-H.; Puebla-Hellmann, G.; Gambardella, P.; Degen, C. L. Scanning nitrogen-vacancy center magnetometry in large in-plane magnetic fields. *Applied Physics Letters* **2022**, *120*, 074003.

(182)   Huang, B.; Clark, G.; Navarro-Moratalla, E.; Klein, D. R.; Cheng, R.; Seyler, K. L.; Zhong, D.; Schmidgall, E.; McGuire, M. A.; Cobden, D. H. Layer-dependent ferromagnetism in a van der Waals crystal down to the monolayer limit. *Nature* **2017**, *546*, 270–273.

(183)   Gong, C.; Li, L.; Li, Z.; Ji, H.; Stern, A.; Xia, Y.; Cao, T.; Bao, W.; Wang, C.; Wang, Y.; Qiu, Z. Q.; Cava, R. J.; Louie, S. G.; Xia, J.; Zhang, X. Discovery of intrinsic ferromagnetism in two-dimensional van der Waals crystals. *Nature* **2017**, *546*, 265–269.

7

(184) Boschker, H.; Harada, T.; Asaba, T.; Ashoori, R.; Boris, A. V.; Hilgenkamp, H.; Hughes, C. R.; Holtz, M. E.; Li, L.; Muller, D. A. Ferromagnetism and conductivity in atomically thin SrRuO3. *Physical review X* **2019**, *9*, 011027.

(185) Ortmanns, L. C.; Bauer, G. E. W.; Blanter, Y. M. Magnon dispersion in bilayers of two-dimensional ferromagnets. *Phys. Rev. B* **2021**, *103*, 155430.

(186) Gibertini, M.; Koperski, M.; Morpurgo, A. F.; Novoselov, K. S. Magnetic 2D materials and heterostructures. *Nature nanotechnology* **2019**, *14*, 408–419.

(187) Jenkins, S.; Rózsa, L.; Atxitia, U.; Evans, R. F. L.; Novoselov, K. S.; Santos, E. J. G. Breaking through the Mermin-Wagner limit in 2D van der Waals magnets. *Nature Communications* **2022**, *13*, 6917.

(188) Ma, Y.; Dai, Y.; Guo, M.; Niu, C.; Zhu, Y.; Huang, B. Evidence of the Existence of Magnetism in Pristine VX2 Monolayers (X = S, Se) and Their Strain-Induced Tunable Magnetic Properties. *ACS Nano* **2012**, *6*, 1695–1701.

(189) Šiškins, M.; Kurdi, S.; Lee, M.; Slotboom, B. J. M.; Xing, W.; Mañas-Valero, S.; Coronado, E.; Jia, S.; Han, W.; van der Sar, T.; van der Zant, H. S. J.; Steeneken, P. G. Nanomechanical probing and strain tuning of the Curie temperature in suspended Cr2Ge2Te6-based heterostructures. *npj 2D Materials and Applications* **2022**, *6*, 41.

(190) Deng, Y.; Yu, Y.; Song, Y.; Zhang, J.; Wang, N. Z.; Sun, Z.; Yi, Y.; Wu, Y. Z.; Wu, S.; Zhu, J.; Wang, J.; Chen, X. H.; Zhang, Y. Gate-tunable room-temperature ferromagnetism in two-dimensional Fe3GeTe2. *Nature* **2018**, *563*, 94–99.

(191) Huang, B.; Clark, G.; Klein, D. R.; MacNeill, D.; Navarro-Moratalla, E.; Seyler, K. L.; Wilson, N.; McGuire, M. A.; Cobden, D. H.; Xiao, D.; Yao, W.; Jarillo-Herrero, P.; Xu, X. Electrical control of 2D magnetism in bilayer CrI3. *Nature Nanotechnology* **2018**, *13*, 544–548.

(192) Wang, Z.; Zhang, T.; Ding, M.; Dong, B.; Li, Y.; Chen, M.; Li, X.; Huang, J.; Wang, H.; Zhao, X. Electric-field control of magnetism in a few-layered van der Waals ferromagnetic semiconductor. *Nature nanotechnology* **2018**, *13*, 554–559.

(193) Borlina, C. S.; Weiss, B. P.; Bryson, J. F. J.; Bai, X.-N.; Lima, E. A.; Chatterjee, N.; Mansbach, E. N. Paleomagnetic evidence for a disk substructure in the early solar system. *Science Advances* **2021**, *7*, eabj6928.

(194) Bossoni, L.; Grand Moursel, L.; Bulk, M.; Simon, B. G.; Webb, A.; van der Weerd, L.; Huber, M.; Carretta, P.; Lascialfari, A.; Oosterkamp, T. H. Human-brain ferritin studied by muon spin rotation: a pilot study. *Journal of Physics: Condensed Matter* **2017**, *29*, 415801.

(195) Wang, P.; Chen, S.; Guo, M.; Peng, S.; Wang, M.; Chen, M.; Ma, W.; Zhang, R.; Su, J.; Rong, X.; Shi, F.; Xu, T.; Du, J. Nanoscale magnetic imaging of ferritins in a single cell. *Science Advances* **2019**, *5*, eaau8038.

(196) Webb, J. L.; Troise, L.; Hansen, N. W.; Achard, J.; Brinza, O.; Staacke, R.; Kieschnick, M.; Meijer, J.; Perrier, J.-F.; Berg-Sørensen, K. Optimization of a diamond nitrogen vacancy centre magnetometer for sensing of biological signals. *Frontiers in Physics* **2020**, *8*, 522536.

7

(197) Bluvstein, D.; Zhang, Z.; Jayich, A. C. B. Identifying and Mitigating Charge Instabilities in Shallow Diamond Nitrogen-Vacancy Centers. *PRL* **2019**, *122*, 076101.

(198) Burek, M. J.; Chu, Y.; Liddy, M. S. Z.; Patel, P.; Rochman, J.; Meesala, S.; Hong, W.; Quan, Q.; Lukin, M. D.; Lončar, M. High quality-factor optical nanocavities in bulk single-crystal diamond. *Nature Communications* **2014**, *5*, 5718.

(199) Mouradian, S.; Wan, N. H.; Schröder, T.; Englund, D. Rectangular photonic crystal nanobeam cavities in bulk diamond. *Appl. Phys. Lett.* **2017**, *111*, 021103.

(200) Sipahigil, A.; Jahnke, K. D.; Rogers, L. J.; Teraji, T.; Isoya, J.; Zibrov, A. S.; Jelezko, F.; Lukin, M. D. Indistinguishable Photons from Separated Silicon-Vacancy Centers in Diamond. *PRL* **2014**, *113*, 113602.

(201) Iwasaki, T.; Miyamoto, Y.; Taniguchi, T.; Siyushev, P.; Metsch, M. H.; Jelezko, F.; Hatano, M. Tin-Vacancy Quantum Emitters in Diamond. *Phys. Rev. Lett.* **2017**, *119*, 253601.

(202) Trusheim, M. E. et al. Transform-Limited Photons From a Coherent Tin-Vacancy Spin in Diamond. *Phys. Rev. Lett.* **2020**, *124*, 023602.

(203) Rugar, A. E.; Dory, C.; Aghaeimeibodi, S.; Lu, H.; Sun, S.; Mishra, S. D.; Shen, Z.-X.; Melosh, N. A.; Vučković, J. Narrow-Linewidth Tin-Vacancy Centers in a Diamond Waveguide. *ACS Photonics* **2020**, *7*, 2356–2361.

(204) Arjona Martínez, J.; Parker, R. A.; Chen, K. C.; Purser, C. M.; Li, L.; Michaels, C. P.; Stramma, A. M.; Debroux, R.; Harris, I. B.; Hayhurst Appel, M.; Nichols, E. C.; Trusheim, M. E.; Gangloff, D. A.; Englund, D.; Atatüre, M. Photonic Indistinguishability of the Tin-Vacancy Center in Nanostructured Diamond. *PRL* **2022**, *129*, 173603.

CURRICULUM VITÆ

Brecht G. SIMON

12-12-1994   Born in Enschede, The Netherlands.

EDUCATION

2007–2013   **Secondary school**
Lyceum de Grundel, Hengelo, The Netherlands

2013–2016   **B.Sc. Physics**
Universiteit Leiden, Leiden, The Netherlands

2013–2016   **B.Sc. Astronomy**
Universiteit Leiden, Leiden, The Netherlands

2016–2018   **M.Sc. Physics**
Universiteit Leiden, Leiden, The Netherlands
Thesis: Current-induced domain-wall motion in permalloy nanowires
Supervisor: Prof. Dr. J. Aarts

International research project
Universität Regensburg, Regensburg, Germany
Thesis: Design and fabrication of hybrid carbon nanotube-$NbSe_2$ devices for Majorana Fermion detection
Supervisor: Prof. Dr. C. Strunk

2018–2023   **Ph.D. Physics**
Delft University of Technology, Delft, The Netherlands
Thesis: Building a platform for magnetic imaging of spin waves
Promotors: Dr. T. van der Sar
Prof. Dr. L. Kuipers

LIST OF PUBLICATIONS

9. T.S. Ghiasi, M. Borst, S. Kurdi, **B.G. Simon**, I. Bertelli, S. Mañas, E. Coronado, H.S.J. van der Zant, T. van der Sar, *Nitrogen vacancy magnetometry of CrSBr by diamond membrane transfer* (submitted)

8. J. J. Carmiggelt, I. Bertelli, R.W. Mulder, A. Teepe, M. Elyasi, **B.G. Simon**, G.E.W. Bauer, Y.M. Blanter, T. van der Sar, *Broadband microwave detection using electron spins in a hybrid diamond-magnet sensor chip* Nature Communications **14**, 490 (2023)

7. **B. G. Simon***, S. Kurdi*, J. J. Carmiggelt, M. Borst, A. J. Katan, T. van der Sar, *Filtering and imaging of frequency-degenerate spin waves using nanopositioning of a single-spin sensor* Nano Letters **22**, 9198–9204 (2022)

6. **B. G. Simon***, S. Kurdi*, H. La, I. Bertelli, J. J. Carmiggelt, M. T. Ruf, N. de Jong, H. van den Berg, A. J. Katan, T. van der Sar, *Directional Excitation of a High-Density Magnon Gas Using Coherently Driven Spin Waves*, Nano Letters **21**, 8213–8219 (2021).

5. I. Bertelli, **B. G. Simon**, T. Yu, J. Aarts, G. E. W. Bauer, Y. M. Blanter, T. van der Sar, *Imaging spin-wave damping underneath metals using electron spins in diamond*, Advanced Quantum Technologies 2100094 (2021)

4. G. Nava Antonio*, I. Bertelli*, **B. G. Simon**, R. Medapalli, D. Afanasiev, T. van der Sar, *Magnetic imaging and statistical analysis of the metamagnetic phase transition of FeRh with electron spins in diamond*, Journal of Applied Physics **129**, 223904 (2021).

3. J. J. Carmiggelt, **B. G. Simon**, I. Bertelli, T. van der Sar, *Spinsensoren in diamant onthullen golvende spinzee*, Nederlands Tijdschrift voor Natuurkunde, June (2021)

2. I. Bertelli, J. J. Carmiggelt, T. Yu, **B. G. Simon**, C. C. Pothoven, G. E. W. Bauer, Y. M. Blanter, J. Aarts, T. van der Sar, *Magnetic resonance imaging of spin-wave transport and interference in a magnetic insulator*, Science Advances **6**, eabd3556 (2020)

1. L. Bossoni, L. G. Moursel, M. Bulk, **B. G. Simon**, A. Webb, L. van der Weerd, M. Huber, P. Carretta, A. Lascialfari, T. H. Oosterkamp, *Human-brain ferritin studied by muon spin rotation: a pilot study*, Journal of Physics: Condensed Matter **29**, 41 (2017).

---

*Equally contributing authors

ACKNOWLEDGEMENTS

Pursuing a PhD was very exciting because I not only got to learn new physics and play around with fancy equipment, but I could also do all that while collaborating with some fantastic people. Without them, this dissertation would not have been the same, and I want to thank them here:

First, I want to thank my supervisor and promotor, **Toeno**, who gave me the opportunity and the means to work on this very cool project. I am grateful for all the skills you taught me and our various discussions ranging from spin-wave physics to setup design and diamond nanofabrication to article writing. During these discussions, I was always amazed by all your ideas, your physics knowledge, as well as lab expertise, and, not to forget, your time-management skills. But, most of all, I thank you for providing such a great and fun atmosphere to do experimental physics research with the occasional parties and for bringing together such an amazing group of people: the van der Sar lab!

Kobus, thank you for being my promotor, for your advice during our meetings, and for leading the department so well.

Allard, you joined the scanning team one year after me, and I am very thankful you did. I can not think of a more skilled scanning probe expert, and it's an honour that you are now also a part of my PhD committee. I hope you will stay with the QN department for a long time to come, saving many PhD projects along the way, as you did for mine.

Tjerk, my first encounter with physics research was with you and **Lucia** during my bachelor project. The various experiments in your lab and at the MRI and synchrotron facilities opened my eyes to how challenging and multifaceted physics experiments could be. Because of this valuable and fun experience, I decided to pursue a PhD in experimental physics, something I had never considered before. Thank you!

I also want to thank the other committee members, **Yaroslav Blanter**, **Sander Otte**, and **Elke Neu-Ruffing** for taking part in my PhD defence ceremony and for reading and assessing my thesis and your feedback. Thank you **Simon Gröblacher** for being a reserve member and sharing your expertise in the diamond fabrication meetings.

My PhD would not have been the same and especially not as fun without the other wonderful members of the van der Sar lab:

Joris, we've shared a decade of studies, during which we've become close friends. I've learned you are one of the smartest people and best teachers I know, and I want to thank

you for all your help in patiently teaching me the details of spin-wave physics. Your enthusiastic and colourful comments during our talks in the office or while cycling back to the Hague were always uplifting and a good guide! Your crazy moments at conferences when you sometimes experienced a bit too much of *onderdompelen*, straying once again from your aspired moderate Stoic life path, made sure our PhD was never boring; I hope to see you back every once in a while to revive some of these old habits. Finally, thank you for being my paranymph, and I wish you and Laar a bright future and an amazing time in Munich.

Samer, you joined the lab during the most intense part of the pandemic. We worked together, trying to keep a 1.5m distance by more or less throwing the keyboard and mouse at each other. This only worked well because of your patient and kind character and unwavering positive attitude. In the end, getting our measurements to work would have been a tedious and impossible exercise without you. As such, I couldn't have wished for a better collaborator, and I thank you for all your help, but most of all, for becoming such a good friend. Finally, thank you for being my paranymph, and I am looking forward to seeing you leading your own amazing lab next and calling you Prof Sam K.

Before I joined the lab, **Iacopo** had not only already realized an amazing setup for spin-wave NV magnetometry, laying the foundation for my PhD and that of the entire lab, but he also defined a solid social code of conduct involving drinks every Friday (and Tuesday?!) afternoon. Thank you for your help living up to those high standards and teaching me everything about designing and aligning optical setups, working with thousands of lines of measurement code, imaging spin waves, and much more. I think you are an extremely talented physicist that I am grateful to have worked with, but most of all, I want to thank you for being such a kind and thoughtful friend.

Michael, I am impressed by your persistence that pays out both in your work and partying endeavours. Especially your carefully designed and characterized setups, including the lab's first low-temperature NV measurements and samples (exotic phenomena in hybrid magnet-superconductor-TMD-diamond-(did I miss something?!)), will be used for a long time to come and are a fantastic achievement for the lab! I want to thank you for your help aligning optics and for all the fun times!

Yufan, I missed your zoom-interview because I was stuck in the cleanroom, a situation you're now very familiar with. Seeing how much you accomplished there and with the upstairs setup is exciting! I am curious to see your upcoming results and feel that your calm and persistent attitude is really the only path toward millikelvin sensing; I am sure you will come far! Finally, thank you for becoming an amazing and reliable colleague and friend, and sorry for abandoning you in Barcelona; it was quite a bike ride!

Finally, the New Kids: **Annick**, **Roland** and **Pim**. You all are a talented and energetic addition to the team. Thank you for organizing the legendary *groepsuitje*! Good luck also to our new members **Fabian** and **Gesa**. I am excited that such a great group is taking our lab's experiments to the next level.

During my time at TNW, I got to know many more amazing people: **Sonia**, thank you for your sincere interest in my work and well-being and all the funny jokes in the corridor. The first to invite me to Friday Beers were **Iacopo**, **Thierry**, **Holger**, and **Nikos**, thanks guys, for the good times and for showing me around the labs! Thierry and **Edouard**, I am sad we never got to combine our research, but Sam managed to cool down the setup, so maybe it's time for your comeback. **Rasa**, you were the best conference roomie. I will miss your laughs, pranks, and kind and uplifting words! **Lucas**, good luck in writing the next Science paper (number 10, I recall??!). **Laetitia**, I wish you all the luck with finding your place within the academic world, but of course, preferably in Germany! **Martin**, stories will be told about your stamping skills and kindness long after you leave, but I somehow feel you will return as a Prof soon. Thank you for passing on your knowledge, and best of luck in Munich. **Makars**, thank you for keeping me in the loop on your project; it says a lot about how much you value collaborations. Good luck with your academic career! **Sonakshi**, you were so helpful when I needed someone to tell me it was okay to ask for more time. Your energetic and kind character lifts the QN spirit to higher levels! **Nicoo!!**, thank you for all your cheerful greetings in the corridor; I will miss them. **Mattias**, **Anta**, I was delighted when you guys joined our legendary soccer team, and I wish we could have played a bit more. Finally, also many thanks to **David**, **Coosje**, **Guillermo**, **Sabrya**, **Irina**, **Marc**, **Thijs**, **Patrick**, **Robbie**, **Alexandre**, **Hester**, **Sarwan**, **Talieh**, and others for making my time in Delft great!

Next, I want to use this opportunity to thank the **Blender Guru** for his amazing, fun, and free tutorials as well as the other Blender enthusiasts willing to share their skills online, pushing scientific illustrating to a whole new level.

My end as a PhD student in Delft also sadly means an end to my Monday-night football career. I want to thank **Schmomus V**, we concurred many, especially in the third half. I will never forget beating the Kavli Warriors (at least once!) and reaching the top of our league! And thank you **Christian**, and of course, all your other team members, for playing with us and organizing the fun summer matches!

I also want to thank my friends outside TU Delft for all the good times and support. **Jessika**, thank you for being such a thoughtful friend, good luck with the final bits of your PhD! Bedankt lieve **Mallerds (Eef, Flo, Ier, Jan, San, Taar, Willie)**, jullie zijn een geweldige groep mensen. Ik hoop dat we elkaar vaak blijven zien bij *ploco's,* op kampeertrips en dat we onze dansskills blijven door ontwikkelen. **Charlotte**, ik weet zeker dat jouw attente en creatieve karakter je ver zullen brengen als arts en als wetenschapper. Bedankt voor je vriendschap en ik hoop je snel weer te zien in Stockholm! **Margôt**, al sinds groep drie ben jij mijn allerallerallerbeste vriend. Wij maakten samen (prijswinnende) stop-motion filmpjes, kampeerden in weilanden en gingen op reis en ik hoop dat we dat soort avonturen nog lang blijven opzoeken! Bedankt voor alle fijne gesprekken en steun als ik er doorheen zat. **Mijn Twentse vrienden**, bedankt voor jullie gezelligheid en ik hoop dat we elkaar blijven overhalen om elkaar te zien al is het in Amsterdam of de jaarlijkse Kerstmiddag in Hengelo.

Als laatste wil ik mijn familie, de **Simonnen**, de **Zwetsloten** en de **Jenneboers** bedanken voor alle steun en interesse. **Oom Wim** en **tante Marleen** bedankt voor alle hulp tijdens mijn studie. **Goitze**, bedankt voor het zijn van mijn grote broer en voorbeeld. Toen ook ik naar Delft verhuisde zorgde jij ervoor dat ik mij meteen thuis voelde en op de hoogte was van het Delftse studentenleven, met als hoogtepunten DJ PJ op lichtjesavond en de maandagavond voetbalcompetitie. Het is geweldig dat je zo'n leuke plek hebt gevonden in Kopenhagen en ik wens je heel veel geluk en een hoop gezelligheid toe en hopelijk zie ik je daar snel! **Mam**, ik vind jouw werk prachtig en hoop dat je geïnspireerd blijft om nog een lange tijd mooie dingen te maken. Bedankt voor het goede voorbeeld, door altijd te kiezen voor een interessante carrière, maar bovenal, wil ik je bedanken voor een prachtige jeugd en mijn allerliefste herinnering: onze lange zomers aan de zandstranden van Bretagne toen ook **Lambert** er nog was. Als laatste, bedankt lieve **Bas** voor al jouw steun afgelopen jaren en dat je altijd zorgt voor een fijne plek om thuis te komen, met niet te vergeten onze gekke kat Jack. Ik hou van jou!

- Oegstgeest, May 1, 2023